



Pilkington Library

Author/Filing Title LEE

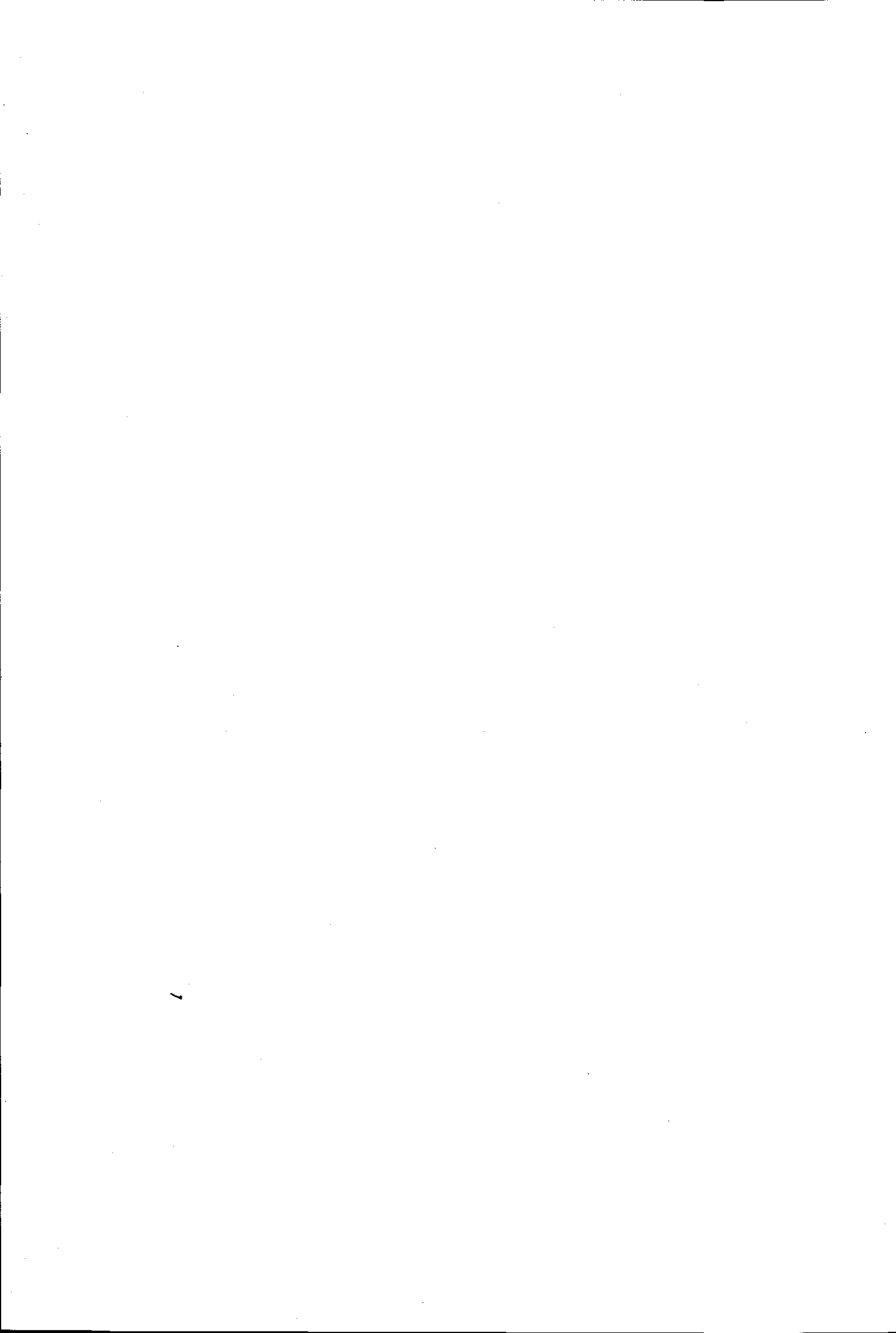
Vol. No. Class Mark T

**Please note that fines are charged on ALL
overdue items.**

	LOAN COPY	
--	-----------	--

0402155440





**Design and Modelling of Photonic Band-gap
Response from Doubly Periodic Arrays**

by

Richard Lee Yee Loong, BEng


Master of Philosophy Thesis

Submitted in Partial fulfillment of the requirements for the award of degree
of Master of Philosophy by Loughborough University

January 2000

Department of Electronic and Electrical Engineering
Loughborough University
United Kingdom

© Richard Y L Lee, 1999

 Loughborough University Pittenger Library
Date <i>July 00</i>
Class
Acc No. <i>040215540</i>

M000 1623 LB

To my Mother and my Wife

Abstract

Currently, much research is aimed at using light as an information carrier in systems. Photonic crystals are materials with varying dielectric properties designed to interact with photons. If these crystals are arranged in a periodic structure they can control the propagation of electromagnetic waves through the structure. Photonic Bandgap (PBG) crystal is a periodic structure that prohibits propagation of all electromagnetic waves within a particular frequency band. Original PBG research was done in the optical region, but PBG properties are scaleable and applicable to a wide range of frequencies. In recent years, there has been increasing interest in microwave and millimeter-wave applications of PBG structures. Currently, research has also extended to Metallodielectric Photonic crystal (MDPC) which is replacing the photonic crystal with periodic metal elements in low dielectric region.

Frequency Selective Surfaces (FSSs) which have been extensively researched are planar versions of a two dimensional metallodielectric PBG crystal. The emergence of the band gap was first investigated by an earlier study on propagation behavior of periodic arrays as FSS in rectangular waveguides and leaky wave antennas.

The research effort in this thesis concentrates on the modelling and practical demonstration of such doubly periodic metallic arrays on dielectric sheets that prohibit any propagation of electromagnetic fields in all planar directions within the bandgap frequencies. In general, the resonant properties of an FSS across the reflection band make them prime candidates for yielding a controlled photonic band-gap. Extending from the techniques used in the analysis of FSS by the investigating the propagation constant along the substrate's surface, the properties of the PBG can be examined for a specific array geometry from the dispersion curves. By varying the array parameters such as the type of element, physical dimension, lattice parameters and dielectric constants of the substrates, the control of the band gap is investigated. Prototypes have been fabricated and tested to verify the simulation prediction of the location of the absolute bandgap for various types of array elements, dimensions and lattice arrangement. Applications of such structures in microstrip and patch antenna designs are also investigated.

Keywords- Photonic Bandgap (PBG), Frequency Selective Surface (FSS), Periodic Structures, Surface waves, Method of Moment (MoM), 2-D Planar arrays.

ACKNOWLEDGEMENTS

I would foremost like to thank my supervisor, Professor Yiannis Vardaxoglou, for his supervision and encouragement throughout this research. I am most grateful for the constant guidance and all the sessions of fruitful discussion.

I would like to acknowledge the receipt of the Overseas Research Scholarship (ORS) Award and the Loughborough University Departmental Studentship Award.

I extend my thanks to all the technical and administrative staff for their support in this research especially Neville Carpenter, Mark Snape, Dave Brown and Susan Dart.

I would also like to thank all my colleagues in the Antennas group at Loughborough, Mohan, James, Alex and Gavin. I would specially like to thank Alford for his help and the designing of patch antennas for our investigation and Patrick from Centre for Mobile Communications Research for his supportive advice.

I am especially grateful to Dr Dave Lockyer for all the advice, explanation and help that he has given me.

I am very grateful to my mother and brother for all of their love and support and prayers. I am especially grateful to my wife, Lydia, for her moral support and unswerving love and being there for me always.

Finally, I would like to thank God most of all for providing the opportunity and His grace for me to do this M.Phil. He has guided me through all the highs and lows especially in time of need.

PUBLICATIONS FROM THE RESEARCH

- [1] VARDAXOGLU J.C., LOCKYER D.S., KEARNEY M.J., LEE Y.L.R.: 'Photonic Induced Antenna Arrays and Their Bandgap Properties', International Conference on Electromagnetics in Advanced Applications 1999, pp 485-488.
- [2] LEE R., VARDAXOGLU J.C., BUDIMUR D.: 'Microwave Band-gap and Band-pass Structures using Planar Metallodielectric Periodic Arrays', 30th ARMMS Conference Digest, Hindhead, United Kingdom, Nov. 1999.
- [3] VARDAXOGLU J.C., LEE R.: 'Photonic Band-gap and Band-pass Characteristics from Dipole and Tripole FSS Structures', Abstract accepted for publication in AP2000 Millennium Conference on Antenna and Propagation, Davos, Switzerland, April 2000.
- [4] LEE R., CHAURAYA A., VARDAXOGLU J.C.: 'Metallodielectric Photonic Band Gap Structures for Microwave Filter and Antenna Applications' Submitted for PREP2000 Conference, Nottingham, United Kingdom, April 2000.
- [5] LEE R., VARDAXOGLU J.C., BUDIMUR D.: 'High Q resonator using a Microwave Bandgap Structure from Periodic Array of conducting Dipoles', Submitted for publication in Electronics Letters.
- [6] VARDAXOGLU J.C., LEE R.: 'Dispersion curves of Dipole and Cross Dipole 2-D Planar Array for Microwave Bandgap application', Submitted for publication in Electronics Letters.
- [7] VARDAXOGLU J.C., LEE R.: 'Analysis of 2-D planar Microwave Bandgap for Antenna Applications', Submitted for publication in IEE Proceedings.
- [8] VARDAXOGLU J.C., LEE R.: 'Performance of a Vivaldi antenna on a two dimensional tripole array FSS', Submitted for publication Microwave and Optical Technology Letters.

Symbols and Greek letters used in Thesis

A	unit cell area
A'	Conducting area of unit cell
c_n	coefficient of the basis function
$\underline{D}_u, \underline{D}_v$	lattice vectors
\underline{E}	transverse electric vector field
\underline{H}	transverse magnetic vector field
h_n	entire domain basis functions
\underline{I}	current of the array element
\tilde{J}	spectrum of electric current
k^i	incident wave vector
\underline{k}_{mpq}	modal wave vector
$R_{coeff}^{cpo}, T_{coeff}^{cpo}$	reflection and transmission coefficients (copolar)
\underline{r}	tangential position vector
s	substrate thickness
$\alpha, \alpha_1, \alpha_2$	lattice related angles
β_{pq}	modal propagation constant
ϵ_r	relative permittivity (dielectric constant)
η_{mpq}	modal admittance
θ^i, ϕ^i	incident polar angles
Ξ_{pq}, Ψ_{pq}	modal field solutions
\underline{K}_{mpq}	modal unit vector $m = 1$ TM modes, $m = 2$ TE modes

TABLE OF CONTENTS

	Page
Abstract	i
Acknowledgements	ii
CHAPTER 1	
INTRODUCTION TO PHOTONIC BANDGAP CRYSTAL	
1.0 Introduction.....	1
1.1 Two Dimension planar Metallodielectric Photonic Crystal.....	4
1.2 Organisation of this Thesis	5
<i>References.....</i>	<i>7</i>
CHAPTER 2	
THEORY OF ANALYSIS	
2.0 Introduction	10
2.1 Modal Analysis of Planar Frequency Selective Surface.....	12
2.1.1 Modal Field Representation.....	14
2.2 Formulation of Scattering for a Single FSS Structure	18
2.2.1 Fields at different interfaces	18
2.2.2 Electric Field Integral equation (EFIE)	23
2.3 Method of Moments	25
2.4 Reflection and Transmission Coefficients.....	27
2.4 Propagation along the surface (X-Y plane).....	30

2.5	Direct and Reciprocal Lattices in Two Dimensions.....	32
2.6.1	Irreducible Brillouin zone and the array element.....	37
2.7	Conclusions.....	40
	<i>References.....</i>	41

CHAPTER 3

SURFACE WAVES ON A DIELECTRIC SLAB

3.0	Introduction	43
3.1	Propagation Modes of a Dielectric Slab on a Ground Plane.....	44
3.1.1	TM modes.....	44
3.1.2	TE modes.....	46
3.2	Program simulation and results.....	47
3.3	Conclusions.....	51
	<i>References.....</i>	52

CHAPTER 4

PLANAR 2-D ARRAY USING DIPOLE AND CROSS DIPOLE CONDUCTORS

4.0	Introduction.....	53
4.1	Experimental setup.....	54
4.2	Planar 2-D array using Dipole and Cross Dipole conductor.....	59
4.3	Dipole Array Results and Discussion.....	62
4.3.1	Dipole Dimension ($D=10\text{mm}$, $L=7.5\text{mm}$).....	63
4.3.2	Dipole Dimension ($D=8\text{mm}$, $L=6\text{mm}$).....	66

4.4	Cross Dipole array Results and Discussion.....	69
4.5	Testing for Convergence.....	72
4.6	Conclusions.....	74
	<i>References.....</i>	75

CHAPTER 5

PLANAR 2-D ARRAY USING TRIPOLE CONDUCTORS AND APPLICATIONS

5.0	Introduction.....	76
5.1	Planar 2-D array using Tripole conductor.....	77
5.2	Tripole Array Simulation Results and Discussion.....	79
5.3	Radiation Pattern of a Tripole Periodic Array on a Vivaldi Antenna.....	83
5.4	Designing the Bandgap Frequency.....	92
5.5	Some Applications investigated.....	96
	5.5.1 Application for Tripole Array	96
	5.5.2 Application for Dipole Array	101
5.5	Conclusions.....	106
	<i>References.....</i>	108

CHAPTER 6

	CONCLUSIONS.....	110
	<i>References.....</i>	113

Chapter 1

Introduction to Photonic Bandgap Crystals

1.0 Introduction

Since the suggestion in 1987 [1], that creating a periodicity in dielectric materials could prevent the propagation of electromagnetic waves at certain frequencies, there has been much work, both theoretical and experimental, in the field of Photonic Crystals to create a so called 'photonic bandgap' (PBG) material.

A photonic crystal is a structure with a periodic arrangement of high dielectric constant cavities embedded within a low dielectric region, these will introduce 'gaps' into the energy band structure for the photon states at Bragg planes and provoke a range of forbidden energies for the photons [2,3]. This range of forbidden frequencies is called the photonic bandgap in which propagation is forbidden in certain directions. For cases at certain frequencies, the photonic crystal will prohibit propagation of an electromagnetic wave at any incident angle, direction and polarization; this is termed as the absolute photonic bandgap.

Photonic crystals of two and three dimensions are being intensively investigated [4]. For the three dimensional photonic crystal, it will have its lattice periodicity in three dimensions and at frequencies in its absolute photonic bandgap region, thereby prohibiting propagation in any direction. Figure 1.1 shows an example of a 3-D square lattice photonic crystal surrounded by air or a low dielectric material (not shown). Fabrication of such a photonic crystal lattice is still a challenge at present.

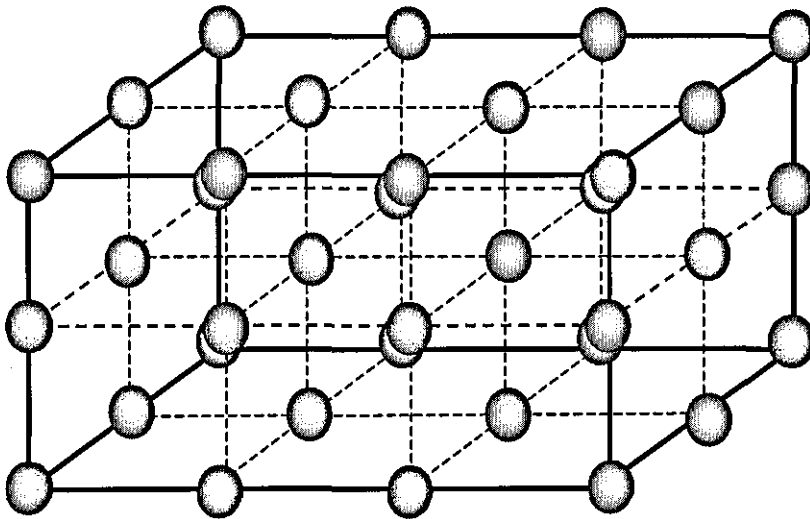


Figure 1.1 : Part of a 3-D square lattice photonic crystal

Whereas a 2-D photonic crystal is easier to fabricate, it possesses periodicity only in the x - y plane and is finite in the z direction. Figure 1.2 shows an example of a 2-D square lattice photonic crystal surrounded by air or a low dielectric material (not shown). Frequencies in its absolute photonic bandgap region will be prohibited for any in-plane propagation (perpendicular to the x - y plane) for any polarization and any direction along the x - y plane. Propagation in the z direction will not see any bandgap since there is no dielectric variation in the z direction [5–10].

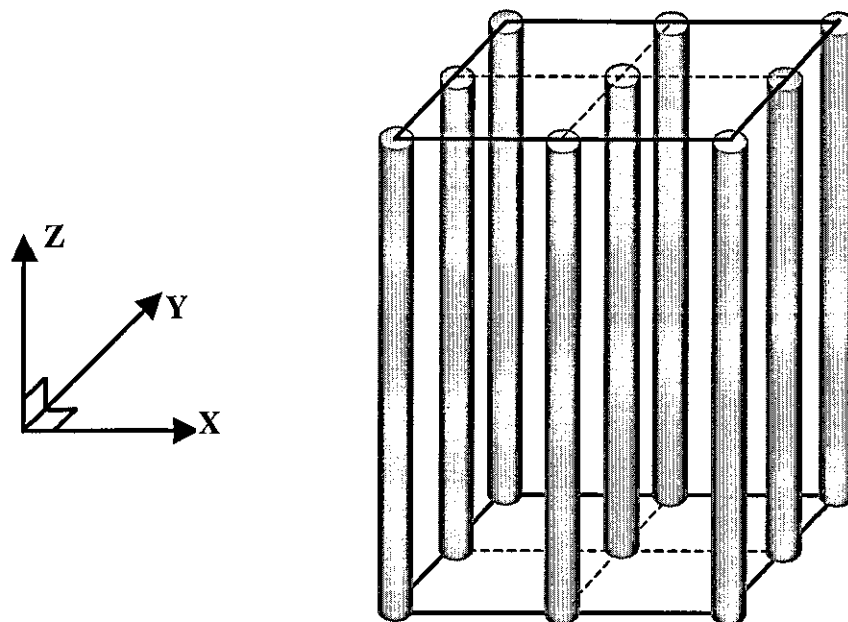


Figure 1.2 : Part of a 2-D square lattice photonic crystal surround by air

Recent years have also seen potential applications for photonic crystals, which have been investigated primarily in the microwave frequency region. One of the applications looked into is an optimised dipole antenna on a photonic bandgap crystal. By fabricating the antenna on the PBG material with the driving frequency in the stopband, no power should be transmitted into the PBG material thus all the power should be radiated in the desired direction [11-13].

Another application utilises the PBG to act as a band reject filter within a waveguide [14].

PBG materials have also been investigated for microstrip circuit applications and have exhibited very high suppression in the stopband [15,16]. It has also been shown that PBG structures can suppress surface waves from microstrip antennas and also improve their directivity [17,18].

1.1 Two Dimension Planar Metallodielectric Photonic Crystal

Original PBG research was done in the optical region [1], but PBG properties are scaleable and applicable to a wide range of frequencies. In recent years, there has been an increasing interest in microwave and millimeter-wave applications of PBG structures.

However, contributors in this field regarding PBG structures in the microwave and millimeter-wave regions still retain the 'photonic band gap' terminology. This terminology has caused some controversy in the microwave community. A recent paper by Oliner [19] has tried to clarify that the terminology is inappropriate and it should be classified under 'microwave periodic structure'. However, the 'photonic bandgap' terminology is adapted at the start of this thesis and subsequently used throughout.

Currently, research has also extended to Metallodielectric Photonic crystal (MDPC) which is replacing the periodic high dielectric constant cavities of the photonic crystal with periodic metallic elements. In microwave and millimeter-wave regions, such structures exhibit a much larger electromagnetic stopband than the photonic crystal [20-21]. The 2-D planar version of metallodielectric Photonic crystal is in effect a type of Frequency Selective Surface (FSS).

Frequency Selective Surfaces are two dimensional periodic arrays of metallic elements or apertures which exhibit stopband and passband characteristics when excited by an electromagnetic wave at an arbitrary angle to the plane of the array (Figure 1.3). For example, a periodic array of conductors will reflect polarised incident waves at some frequencies (stopband) and remain transparent to these waves at other frequencies.

If the incident angle θ is increased to 90° from the normal, the incidence will be along the plane of the FSS array. When exploring the propagation mode along the plane of the FSS array, this structure can be regarded as a planar version of a 2-D metallodielectric PBG crystal and it will exhibit band gap properties in the plane of the array. If the band gap extends throughout the irreducible Brillouin zone (Section 2.6); an absolute photonic band gap is achieved.

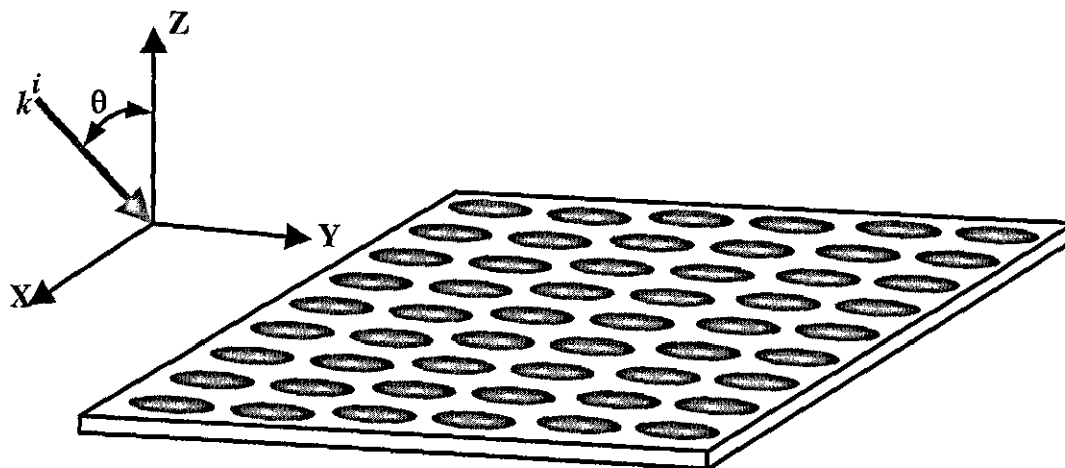


Figure 1.3 : Part of a FSS array as a 2-D planar metalodielectric PBG crystal

The research effort in this study concentrates on the modeling of such doubly periodic metallic arrays on dielectric sheets to obtain an absolute band gap from such a structure. The control of the band gap is investigated by varying the array parameters such as the type of element, physical dimension, lattice parameters and dielectric constants of the substrates.

Prototypes have been fabricated and tested to verify the simulation prediction of the location of the absolute bandgap for various types of array elements, dimensions and lattice geometry. Applications of such structures in microstrip and patch antenna designs are also investigated.

1.2 Organisation of this Thesis

This thesis is organised into six chapters in the following manner.

Chapter 2 lays out the theory that the research techniques used in analysis of FSS which this work draws upon. The analysis of propagation along the surface is achieved by evaluating the propagation constant within the irreducible Brillouin zone to predict the propagation modes.

Finally, this chapter also explores the properties and effects of the reciprocal lattice and its irreducible Brillouin zone from its respective direct lattice and array element.

Chapter 3 looks into surface waves that exist on the dielectric slab with and without a ground plane. Using the propagation constant derived in Chapter 2, the TM/TE surface wave modes are predicted and compared to the analytical values to verify the method of modelling and prediction accuracy.

Chapter 4 covers the array elements of the dipole and cross dipole, with the aim of achieving an absolute bandgap. The experimental set-up for this research work is also described here. Finally, the test of convergence is also investigated to ensure adequate Floquet modes and basis functions are used for the predictions.

Chapter 5 investigates array with tripole elements to achieve an absolute bandgap. Printing a transmitting Vivaldi antenna and a tripole array on a dielectric slab, the radiation pattern measurements are presented in the bandgap and bandpass regions. This chapter also looks into designing the bandgap frequency by varying the element dimensions and the effects on the location of bandgap with different substrate thickness and dielectric constant. Finally, some novel applications of this technology are presented.

Chapter 6 draws conclusions of the work presented in this thesis and suggestions are made for future research work.

REFERENCES

- [1] YABLONOVITCH, E.: 'Inhibited spontaneous emission in solid-state physics and electronics', *Physical Review Letters*, Vol. 58, No 20, May 1987, pp. 2059-2062.
- [2] RUSSELL, P.S.J.: 'Photonic band gaps', *Physics World*, Aug 1992, pp. 37-42.
- [3] YABLONOVITCH, E.: 'Photonic crystals.' *Journal of Modern Optics*, Vol. 41, No. 2, 1994, pp. 173-194.
- [4] JOANNOPOULOS J.D., MEADE R.D., WINN J.N.: 'Photonic Crystals – Molding the Flow of Light', Princeton University Press, 1995.
- [5] MEADE R.D., BROMMER K.D.; RAPPE A.M., JOANNOPOULOS J.D.: 'Existence of a photonic band gap in two dimensions', *Applied Physics Letters*, Vol. 61, No. 41, July 1992, pp. 495-497.
- [6] ROBERTSON, W.M., ARJAVALINGAM, G., MEADE R.D., BROMMER K.D.; RAPPE A.M., JOANNOPOULOS J.D.: 'Measurement of photonic band structure in a two-dimensional periodic dielectric array', *Physical Review Letters*, Vol. 68, No. 13, Mar 1992, pp. 2023-2026.
- [7] LIN S.Y., ARJAVALINGAM G., ROBERTSON, W.M.: 'Investigation of absolute photonic band gaps in two-dimensional dielectric structures', *Journal of Modern Optics*, Vol. 44, No. 2, 1994, pp. 385-393.
- [8] VILLENEUVE P.R. and PICHE M.: 'Photonic band gaps in two-dimensional square lattices: square and circular rods', *Physics Review B*, Vol. 46, No. 8, Aug. 1992, pp. 4973-4975.
- [9] VILLENEUVE P.R. and PICHE M.: 'Photonic band gaps in two-dimensional square and hexagonal lattices', *Physics Review B*, Vol. 46, No. 8, Aug. 1992, pp. 4969-4972

- [10] YANG, H.Y.D.: 'Finite difference analysis of 2-D photonic crystal', IEEE Trans. Microwave Theory and Techniques, Vol. 44, No. 12, Dec 1996, pp.2688-2695.
- [11] BROWN, E.R. and MCMAHON, O.B.: 'High zenithal directivity from a dipole antenna on a photonic crystal', Applied Physics Letters, Vol. 68, No.9, Feb 1996, pp. 1300-1302.
- [12] CHENG, S.D., BISWAS, R., OZBAY, E., MCCALMONT, S., TUTTLE, G., HO, K.M.: 'Optimized dipole antennas on photonic band gap crystals', Applied Physics Letters, VOL. 67, No. 23, Dec 1994, pp. 3399-3401.
- [13] SIGALAS, M.M., BISWAS, R., HO, K.M.: 'Theoretical study of dipole antennas on photonic band-gap materials', Microwave and Optical Technology Letters, Vol. 13, No. 4, Nov 1996, pp. 205-209.
- [14] CALOZ, C., ZURCHER, J-F., SKRIVERVIK, A.K.: 'Measurement of a 2-D photonic crystal in a waveguide', Proc. 10th IEEE Nice-International Symposium on Antennas, JINA 98, NICE, France, pp.627-630.
- [15] RADISIC, V., QIAN, Y., ITOH, T.: ' FDTD simulation and measurement of new photonic band-gap structure for microstrip circuits.' International Symposium on Electromagnetic Theory, May 1998. pp. 843-845.
- [16] RUMSEY, I., PIKET_MAY, M., KELLY, R.K.: 'Photonic bandgap structures used as filters in microstrip circuits', IEEE Microwave and Guided Wave Letters, Vol. 8, No. 10, Oct 1998, pp.336-338.
- [17] CONTOPANAGOS, H., ZHANG, L., ALEXOPOULOS, N.G., 'Thin frequency-selective lattices integrated in novel compact MIC, MMIC and PCA architectures', IEEE trans. on Microwave Theory and Techniques, Vol. 46, No. 11, Nov 1998, pp. 1936-1948.

-
- [18] QIAN, Y., COCCIOLI, R., SIEVENPIPER, D., RADISIC, V., YABLONOVITCH, E., ITOH, T.: 'A microstrip patch antenna using novel photonic band-gap structures', *Microwave Journal*, Jan 1999, pp. 66-76.
- [19] OLINER A.A.: 'Periodic structures and photonic-band-gap terminology: Historical perspectives', 29th European Microwave Conference, Munich, Germany, Oct 1999, pp. 295-298.
- [20] MCINTOSH, K.A., MCMAHON, O.B., VERGHESE, S. 'Three-dimension metalodielectric photonic crystals incorporating flat metal elements', *Microwave and Optical Technology Letters*, Vol. 17, No. 3, Feb 1998, pp.153-156.
- [21] BROWN, E.R. and MCMAHON, O.B.: 'Large electromagnetic stop bands in metalodielectric photonic crystals', *Applied Physics Letters*, Vol. 67, Oct 1995, pp. 2138.

Chapter 2

Theory of Analysis

2.0 Introduction

In this chapter, the modal analysis of an infinite planar array of a single layer FSS in a multiple dielectric substrate is presented. The approach here is based on the total fields from an array structure of a periodic nature where the tangential field TE (transverse electric) and TM (transverse magnetic) components can be expanded in terms of Floquet modes [1].

This modal analysis method was applied originally by Chen [2] for induced current on the conducting plates of a 2-D array in free space. Montgomery [3] included a dielectric substrate on which the periodic array of thin conductors were printed.

This section shows the theory of Floquet's theorem using the periodicity of the FSS. In fact Floquet's theorem is an adaptation of the Fourier series theorem for periodic functions. It enables a modal description for the field in terms of a complete, orthogonal set of modes (Floquet modes) in the vicinity of each element of the array, which are excited uniformly in amplitude but with a linearly varying phase [1].

The array element is assumed to be infinitely thin and perfectly conducting. This array is sandwiched in between the first two dielectric layers, however the modelling program allows up to four different layers behind the array. The fields near the surface in each layer are expanded in terms of Floquet modes for the different dielectric media. Using the standard electromagnetic boundary conditions, the fields are matched at the boundaries to derive an integral equation in terms of the unknown induced current on the conducting elements [4]. Using the Method of Moments [5,6], the integral equation is reduced into a linear system of simultaneous equations. These equations are solved for the induced current and then the reflected and the transmitted field amplitudes can be determined. With the reflected and the transmitted fields, the reflection and transmission coefficients can be derived.

For the modal analysis of FSS which will be presented first, the polarized incident plane wave is at an arbitrary direction with the angle θ to the z axis and the FSS array in the x - y plane (Figure 2.1).

To determine the stopband or photonic bandgap characteristic of the FSS array, the propagation of the incident wave is in the x - y plane ($\theta = 90^\circ$) at any arbitrary direction with angle ϕ , with respect to the x -axis (Figure 2.1). The array with periodicity in two dimensions will exhibit a stopband in the plane of the double periodicity. The method used here to explore the possible band gap for such an array is similar to the modal analysis of FSS. So in the first part of this chapter, the modal analysis used for FSS is presented in detail in Sections 2.1-2.4. The difference in the analysis of band gap for the array in the x - y plane is presented in Section 2.5.

To determine the completed bandgap for a structure, it is necessary to evaluate the propagation modes in all directions within the two dimensional plane. This is achieved by exploring the propagation mode within the irreducible first Brillouin zone. (Section 2.6)

In the Section 2.6, the reciprocal lattice and its respective Brillouin zone are presented [7-11]. It is discovered that the symmetrical relationship of the first Brillouin zone and the array elements do play a part in determining the irreducible first Brillouin zone.

2.1 Modal Analysis Of Planar Frequency Selective Surface (FSS)

In this section, the modal analysis of a single FSS array in a multiple-dielectric substrate is presented. With the periodic placement of the elements of the array, the modal analysis of Floquet's theorem is used to describe the fields which repeat themselves in terms of Floquet modes [4].

When the array is illuminated by an incident plane wave, currents will be induced on the conducting elements. By matching the fields at the different boundaries, an integral equation for the unknown currents is obtained. Using the Method of Moments [5,6], the integral equation can be reduced to a linear system of simultaneous equations. The unknown current is expressed as a series of basis functions. With a Numerical Algorithm Group (NAG) routine [12] which utilises Crout's factorisation, the unknown coefficients of the basis functions are obtained. The current coefficients allow one to obtain the reflected and transmitted field amplitudes. Thus, from the total reflected and transmitted field, the reflection and transmission coefficients are calculated.

The FSS array is assumed to be infinite and each element is located in a unit cell, which is distributed in a periodic configuration. The conducting elements are printed on a dielectric substrate and the conductors are assumed to be infinitely thin and perfectly conducting.

The array on the dielectric substrate is considered to lie in the x - y plane and it is excited by a linearly polarised plane wave incident in an arbitrary direction with angle θ to the z -axis and ϕ to the x -axis (Figure 2.1). The lattice vectors D_x and D_y specify the two periodicity axis on which the conducting elements are arranged.

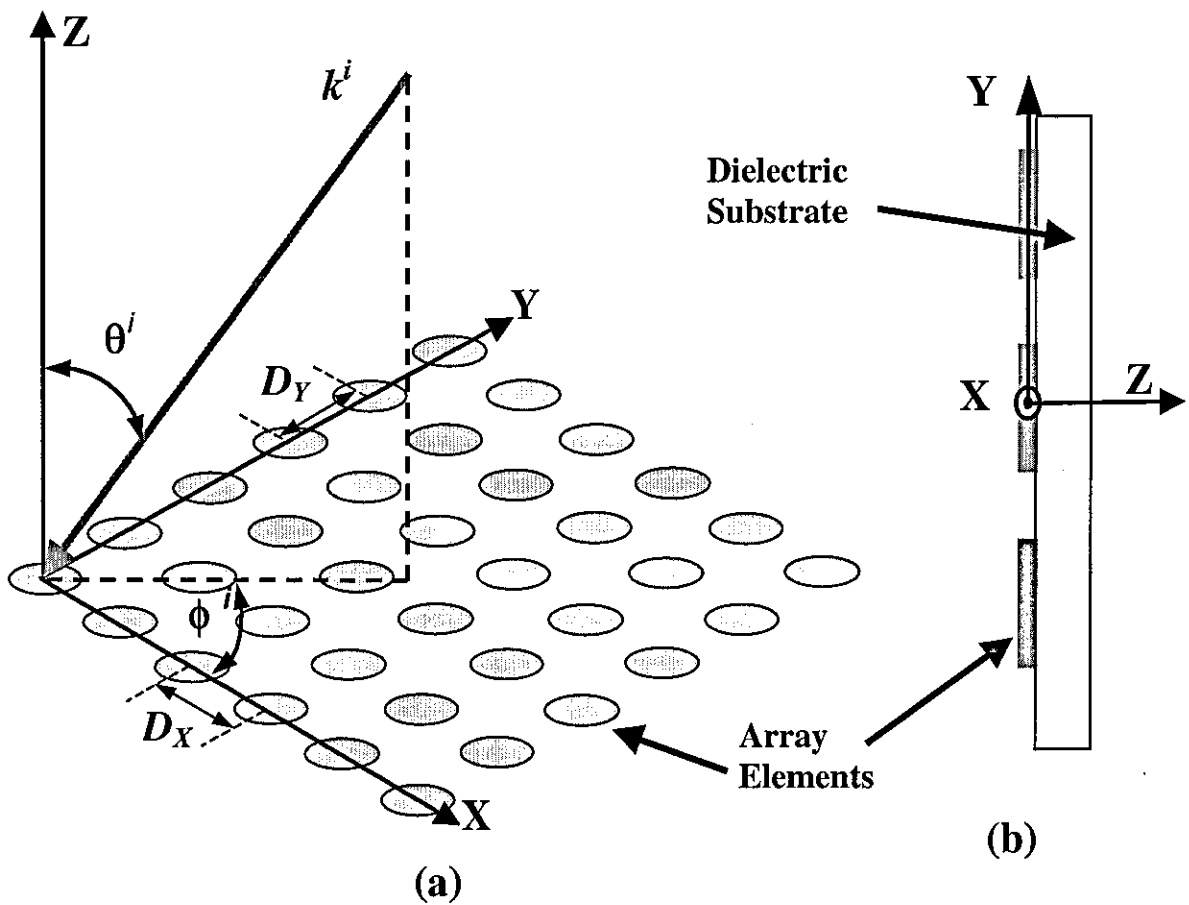


Figure 2.1 : (a) Geometry of a square lattice array, (b) side view of the FSS array

For an arbitrary lattice (Figure 2.2), where the element is placed along an arbitrary axis say \hat{u} and \hat{v} vectors. The arbitrary lattice vectors \underline{D}_u and \underline{D}_v with α as the angle between \underline{D}_u and \underline{D}_v and α_1 as the angle between \underline{D}_u and the x -axis.

$$\begin{aligned} \underline{D}_u &= D_u (\cos \alpha_1 \hat{x} + \sin \alpha_1 \hat{y}) \\ \underline{D}_v &= D_v (\cos \alpha_2 \hat{x} + \sin \alpha_2 \hat{y}) \end{aligned} \tag{2.1}$$

Where $\alpha_2 = \alpha + \alpha_1$ and $D_u = |\underline{D}_u|$, $D_v = |\underline{D}_v|$

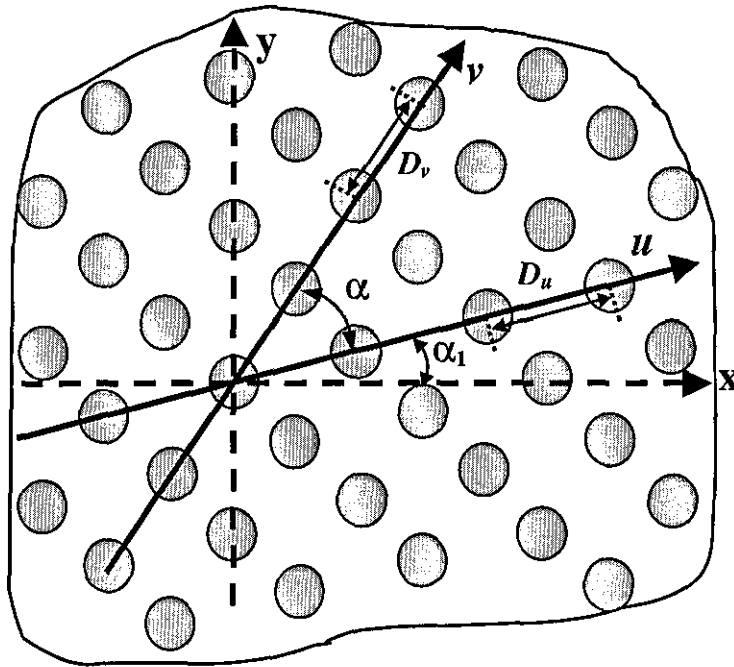


Figure 2.2 : A FSS array on an arbitrary lattice

2.1.1 Modal Field Representation

The modal representation of the field of the array in scalar Floquet modes [1] are given

$$\underline{E}_{pq}(x, y, z) = \Psi_{pq}(x, y) e^{\pm j\beta_{pq} z} \quad (2.2)$$

Where the Floquet indices $p, q = 0, \pm 1, \pm 2, \pm 3, \dots$

The negative j term denotes propagation in the positive direction and the positive j term denotes propagation in the negative direction.

Where

$$\Psi_{pq}(x, y) = e^{-jk_{tpq} \cdot \underline{r}} \quad (2.3)$$

Thus from Eq.(2.2) and Eq.(2.3)

$$\underline{E}_{pq}(\underline{r}, z) = e^{-j\underline{k}_{tpq} \cdot \underline{r}} e^{\pm j\beta_{pq} z} \quad (2.4)$$

Where $\underline{r} = x \hat{x} + y \hat{y}$

And

$$\begin{aligned} \underline{k}_{tpq} &= k_x \hat{x} + k_y \hat{y} \\ \underline{k}_{tpq} &= \underline{k}_{t00} + p \underline{k}_1 + q \underline{k}_2 \\ &= (\underline{k}_{0x} + p \underline{k}_{1x} + q \underline{k}_{2x}) \hat{x} + (\underline{k}_{0y} + p \underline{k}_{1y} + q \underline{k}_{2y}) \hat{y} \end{aligned} \quad (2.5)$$

And

$$\begin{aligned} \underline{k}_{t00} &= \underline{k}_{00x} + \underline{k}_{00y} \\ &= k_0 \sin \theta \cos \phi + k_0 \sin \theta \sin \phi \quad \text{where } k_0 = \frac{2\pi}{\lambda} \end{aligned}$$

$$\underline{k}_1 = -\frac{2\pi}{A} \hat{z} \times \underline{D}_v \quad \underline{k}_2 = \frac{2\pi}{A} \hat{z} \times \underline{D}_u \quad A = |\underline{D}_u \times \underline{D}_v|$$

where A - Periodic unit cell area

Using the relationship given, \underline{k}_1 and \underline{k}_2 can be shown to be

$$\underline{k}_1 = \underline{k}_{1x} + \underline{k}_{1y} \quad \underline{k}_2 = \underline{k}_{2x} + \underline{k}_{2y} \quad A = D_u D_v \sin \alpha$$

$$\begin{aligned} \underline{k}_{1x} &= \frac{2\pi \sin \alpha_2}{D_u \sin \alpha} & \underline{k}_{2x} &= -\frac{2\pi \sin \alpha_1}{D_v \sin \alpha} \\ \underline{k}_{1y} &= -\frac{2\pi \cos \alpha_2}{D_u \sin \alpha} & \underline{k}_{2y} &= \frac{2\pi \cos \alpha_1}{D_v \sin \alpha} \end{aligned}$$

The propagation constant is given as

$$\begin{aligned}\beta_{pq} &= \sqrt{k^2 - (k_x^2 + k_y^2)} \\ &= \sqrt{k^2 - \underline{k}_{tpq} \cdot \underline{k}_{tpq}}\end{aligned}\quad (2.6)$$

Where $k = k_o \sqrt{\epsilon_r}$

For the propagating wave, $k^2 \geq k_x^2 + k_y^2$ and

$$\beta_{pq} = \sqrt{k^2 - \underline{k}_{tpq} \cdot \underline{k}_{tpq}}, \quad \beta_{pq} \text{ is real and positive.}$$

For the evanescent wave, $k^2 < k_x^2 + k_y^2$ and

$$\beta_{pq} = -j \sqrt{\underline{k}_{tpq} \cdot \underline{k}_{tpq} - k^2} \quad \beta_{pq} \text{ is imaginary and negative.}$$

The tangential electromagnetic field in the plane of the array can be expressed in terms of both Transverse Magnetic (TM) and Transverse Electric (TE) vector Floquet modes.

The subscript m that has the value 1 and 2 denotes TM and TE mode respectively.

The Transverse Magnetic vector has its magnetic component parallel to the plane of the array ($H_{zpq} = 0$).

TM modes – The transverse component of the TM modes

$$\underline{E}_{tpq} = \frac{k_{tpq}}{|\underline{k}_{tpq}|} \Psi_{pq} = \underline{\kappa}_{1pq} \Psi_{pq} \quad (2.7)$$

$$\underline{H}_{tpq} = \eta_{1pq} \hat{z} \times \underline{\kappa}_{1pq} \Psi_{pq} \quad (2.8)$$

The transverse electric vector has its electric component parallel to the plane of the array ($E_{zpq} = 0$).

TE modes - The transverse component of the TE modes

$$\underline{E}_{tpq} = \underline{k}_{2pq} \Psi_{pq} \quad (2.9)$$

$$\underline{H}_{tpq} = \eta_{2pq} \hat{z} \times \underline{\kappa}_{2pq} \Psi_{pq} \quad (2.10)$$

Where η_{1pq} and η_{2pq} are the modal admittance of TM and TE modes respectively

$$(TM) \quad \eta_{1pq} = \frac{k\eta}{\beta_{pq}} \quad (2.11)$$

$$(TE) \quad \eta_{2pq} = \frac{\beta_{pq}\eta}{k} \quad (2.12)$$

Where $\eta = \sqrt{\frac{\epsilon}{\mu}}$, ϵ and μ are the permittivity and permeability of the medium.

Thus the tangential field can be expressed as a combination of the vectors TM and TE Floquet modes. For example, the electric field can be written as;

$$\begin{aligned} \underline{E}(\underline{r}, z) &= \sum_{pq} (a_{1pq} E_{1pq}(\underline{r}, z) + a_{2pq} E_{2pq}(\underline{r}, z)) \\ &= \sum_{pq} (a_{1pq} \Psi_{pq}(\underline{r}) \underline{\kappa}_{1pq} e^{\pm j\beta_{pq}z} + a_{2pq} \Psi_{pq}(\underline{r}) \underline{\kappa}_{2pq} e^{\pm j\beta_{pq}z}) \\ \underline{E}(\underline{r}, z) &= \sum_{mpq} a_{mpq} \Psi_{pq}(\underline{r}) \underline{\kappa}_{mpq} e^{\pm j\beta_{pq}z} \end{aligned} \quad (2.13)$$

Where a_{1pq} and a_{2pq} are the amplitude of the TM and TE modes

And the similarly, the magnetic field,

$$\underline{H}(\underline{r}, z) = \pm \sum_{mpq} \eta_{mpq} a_{mpq} \Psi_{pq}(\underline{r}) e^{\pm j\beta_{pq}z} \hat{z} \times \underline{\kappa}_{mpq} \quad (2.14)$$

2.2 Formulation of Scattering for a Single FSS Structure

2.2.1 Fields at different interfaces

Figure 2.4 shows the cross-sectional view of an FSS array embedded in five layers of dielectric substrates surround by air. The different dielectric substrates will modify the admittance seen by the wave when travelling through them. The superscript presented here in the equation denotes the different dielectric layer substrates. With S_n as the thickness, η^n as the modal admittance and T^n with the negative z dependence as the field amplitude of the forward direction travelling wave. Likewise R^n with the positive z dependence would be the field amplitude of the backward travelling waves.

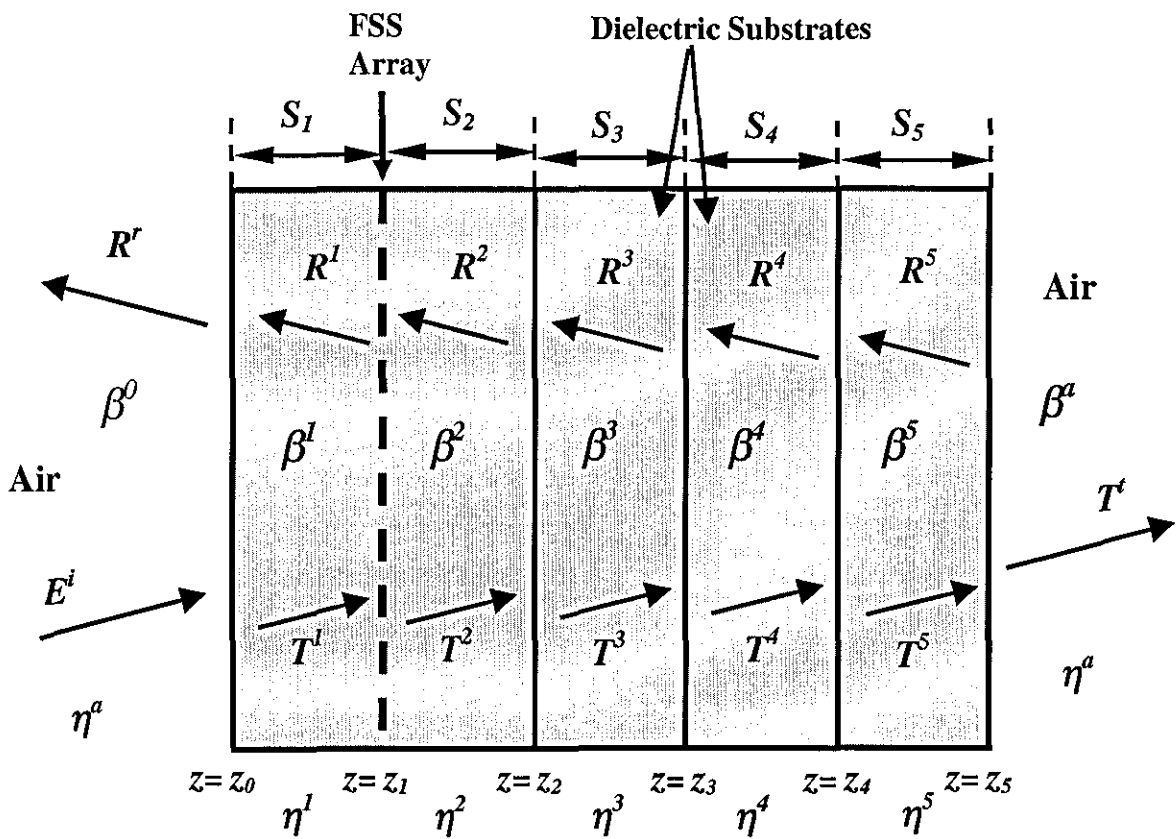


Figure 2.4 : A single FSS array embedded in between the first two dielectric layers.

For this example, the FSS array is assumed to be sandwiched between the first and second layer [4]. With the incident field \underline{E}^{inc} , the modal tangential electromagnetic field for each region is as follows.

For $z \leq z_0$

$$\underline{E}^-(\underline{r}, z) = \underline{E}^{inc} + \sum_{mpq} R_{mpq}^- e^{+j\beta_{pq}^0 z} \Psi_{pq}(\underline{r}) \underline{\kappa}_{mpq} \quad (2.15)$$

$$\underline{H}^-(\underline{r}, z) = \underline{H}^{inc} - \sum_{mpq} \eta_{mpq}^a R_{mpq}^- e^{+j\beta_{pq}^0 z} \Psi_{pq}(\underline{r}) \hat{z} \times \underline{\kappa}_{mpq}$$

For $z_n \leq z \leq z_{n+1}$ (For layer $n = 1, 2, 3, 4$)

$$\underline{E}^n(\underline{r}, z) = \sum_{mpq} \left(T_{mpq}^n e^{-j\beta_{pq}^n z^n} + R_{mpq}^n e^{+j\beta_{pq}^n z^n} \right) \Psi_{pq}(\underline{r}) \underline{\kappa}_{mpq} \quad (2.16)$$

$$\underline{H}^n(\underline{r}, z) = \sum_{mpq} \eta_{mpq}^n \left(T_{mpq}^n e^{-j\beta_{pq}^n z^n} - R_{mpq}^n e^{+j\beta_{pq}^n z^n} \right) \Psi_{pq}(\underline{r}) \hat{z} \times \underline{\kappa}_{mpq}$$

For $z \geq z_5$

$$\underline{E}^+(\underline{r}, z) = \sum_{mpq} T_{mpq}^+ e^{-j\beta_{pq} z} \Psi_{pq}(\underline{r}) \underline{\kappa}_{mpq} \quad (2.17)$$

$$\underline{H}^+(\underline{r}, z) = \sum_{mpq} \eta_{mpq}^a T_{mpq}^+ e^{-j\beta_{pq} z} \Psi_{pq}(\underline{r}) \hat{z} \times \underline{\kappa}_{mpq}$$

For a single FSS structure, the incident field is given in terms of the zeroth order Floquet mode ($p, q = 0$) as

$$\underline{E}^{inc}(\underline{r}, z) = \sum_{m=1}^2 T_{m00}^{inc} e^{-j\beta_{00} z} \Psi_{00}(\underline{r}) \underline{\kappa}_{m00} \quad (2.18)$$

$$\underline{H}^{inc}(\underline{r}, z) = \sum_{m=1}^2 \eta_{m00}^a T_{m00}^{inc} e^{-j\beta_{00} z} \Psi_{00}(\underline{r}) \hat{z} \times \underline{\kappa}_{m00}$$

However, the prediction program for propagation constants (β_x, β_y) along in the x - y plane does not have any incidence fields; the incidence fields and scattered fields are combined as the total fields (see Section 2.6).

With the modal tangential electromagnetic fields for each dielectric layer defined in Eq. (2.15 – 2.17), boundary conditions are applied by matching or equating the fields between 2 layers at their common boundary. Working backwards from the last layer towards the first boundary, an expression of the reflected amplitude R_{mpq}^- in terms of the surface current density \underline{J} can be derived

The field amplitudes can be formed using mode orthogonality in Eq.(2.16) and Eq.(2.17) and matching at boundary $Z = Z_5$,

(Magnetic field)

$$\eta_{mpq}^5 \left(T_{mpq}^5 e^{-j\beta_{pq}^5 z_5} - R_{mpq}^5 e^{+j\beta_{pq}^5 z_5} \right) = \eta_{mpq}^a T_{mpq}^+ e^{-j\beta_{pq}^a z_5} \quad (2.19)$$

(Electric Field)

$$T_{mpq}^5 e^{-j\beta_{pq}^5 z_5} + R_{mpq}^5 e^{+j\beta_{pq}^5 z_5} = T_{mpq}^+ e^{-j\beta_{pq}^a z_5} \quad (2.20)$$

Placing the magnetic field equation Eq.(2.19) over the electric field Eq.(2.20) at boundary Z_5 , an expression can be obtain that related the reflective field to that of the transmitted field for that boundary. (Magnetic field / Electric field)

$$\frac{\eta_{mpq}^5 \left(T_{mpq}^5 e^{-j\beta_{pq}^5 z_5} - R_{mpq}^5 e^{+j\beta_{pq}^5 z_5} \right)}{\left(T_{mpq}^5 e^{-j\beta_{pq}^5 z_5} + R_{mpq}^5 e^{+j\beta_{pq}^5 z_5} \right)} = \frac{\eta_{mpq}^a T_{mpq}^+ e^{-j\beta_{pq}^a z_5}}{T_{mpq}^+ e^{-j\beta_{pq}^a z_5}}$$

$$R_{mpq}^5 = \left(\frac{\eta_{mpq}^5 - \eta_{mpq}^a}{\eta_{mpq}^5 + \eta_{mpq}^a} \right) e^{-j2\beta_{pq}^5 z_5} T_{mpq}^5$$

$$R_{mpq}^5 = \rho_{mpq}^5 T_{mpq}^5 \quad (2.21)$$

Likewise at boundary $Z = Z_4$, matching the fields and equating the magnetic field over the electric field using Eq.(2.21) gives,

$$\frac{\eta_{mpq}^4 \left(T_{mpq}^4 e^{-j\beta_{pq}^4 z_4} - R_{mpq}^4 e^{+j\beta_{pq}^4 z_4} \right)}{\left(T_{mpq}^4 e^{-j\beta_{pq}^4 z_4} + R_{mpq}^4 e^{+j\beta_{pq}^4 z_4} \right)} = \frac{\eta_{mpq}^5 T_{mpq}^5 \left(e^{-j\beta_{pq}^5 z_4} - \rho_{mpq}^5 e^{+j\beta_{pq}^5 z_4} \right)}{T_{mpq}^5 \left(e^{-j\beta_{pq}^5 z_4} + \rho_{mpq}^5 e^{+j\beta_{pq}^5 z_4} \right)}$$

$$\frac{\eta_{mpq}^4 \left(T_{mpq}^4 e^{-j\beta_{pq}^4 z_4} - R_{mpq}^4 e^{+j\beta_{pq}^4 z_4} \right)}{\left(T_{mpq}^4 e^{-j\beta_{pq}^4 z_4} + R_{mpq}^4 e^{+j\beta_{pq}^4 z_4} \right)} = \eta_{mpq}^5 \omega_4^5 \quad (2.22)$$

$$R_{mpq}^4 = \rho_{mpq}^4 T_{mpq}^4$$

For all boundaries,

$$\rho_{mpq}^n = \left(\frac{\eta_{mpq}^n - \omega_n^{n+1} \eta_{mpq}^{n+1}}{\eta_{mpq}^n + \omega_n^{n+1} \eta_{mpq}^{n+1}} \right) e^{-j2\beta_{pq}^n z_n} \quad (2.23)$$

Where ω_n^{n+1} is denote as ω_n^{n+1}

$$\text{And } \omega_n^{n+1} = \frac{e^{-j\beta_{pq}^n z_{n-1}} - \rho_{mpq}^n e^{+j\beta_{pq}^n z_{n-1}}}{e^{-j\beta_{pq}^n z_{n-1}} + \rho_{mpq}^n e^{+j\beta_{pq}^n z_{n-1}}} \quad (2.24)$$

At the last medium ($Z \geq Z_5$), $\omega_5^a = 1$

Working towards $Z = Z_1$, where the FSS array is located, the electric field is continuous ($\underline{E}_1 = \underline{E}_2$). The magnetic field is continuous except on the conductors where it is discontinuous; $\underline{H}_1 - \underline{H}_2 = \hat{z} \times \underline{J}$ where \underline{J} is the unknown surface current density.

At $Z = Z_1$ (Magnetic field)

$$H_1(z, z_1) - H_2(z, z_2) = \frac{\tilde{J}_{mpq}}{A}$$

$$\eta_{mpq}^1 \left(T_{mpq}^1 e^{-j\beta_{pq}^1 z_1} - R_{mpq}^1 e^{+j\beta_{pq}^1 z_1} \right) - \eta_{mpq}^2 \left(T_{mpq}^2 e^{-j\beta_{pq}^2 z_2} - \rho_{mpq}^2 e^{+j\beta_{pq}^2 z_2} \right) = \frac{\tilde{J}_{mpq}}{A}$$

(Electric Field)

$$T_{mpq}^1 e^{-j\beta_{pq}^1 z_1} + R_{mpq}^1 e^{+j\beta_{pq}^1 z_1} = T_{mpq}^2 \left(e^{-j\beta_{pq}^2 z_2} - \rho_{mpq}^2 e^{+j\beta_{pq}^2 z_2} \right)$$

Likewise working with the magnetic and electric fields at $Z = Z_1$,

$$R_{mpq}^1 = \rho_{mpq}^1 T_{mpq}^1 - \frac{e^{-j\beta_{pq}^1 z_1}}{\left(\eta_{mpq}^1 + \omega_1^2 \eta_{mpq}^2 \right)} \frac{\tilde{J}_{mpq}}{A} \quad (2.25a)$$

$$\text{Where } \alpha = \frac{e^{-j\beta_{pq}^1 z_1}}{\left(\eta_{mpq}^1 + \omega_1^2 \eta_{mpq}^2 \right)}$$

With some algebraic manipulation,

$$R_{mpq}^1 = \rho_{mpq}^1 T_{mpq}^1 - \left(e^{-j\beta_{pq}^1 z_0} + \rho_{mpq}^1 e^{+j\beta_{pq}^1 z_0} \right) \tau_{mpq}^1 \frac{\tilde{J}_{mpq}}{2\eta_{mpq}^1 A} \quad (2.25b)$$

Where $n > 0$

$$\tau_{mpq}^n = \frac{e^{-j\beta_{pq}^n z_n} + \rho_{mpq}^n e^{+j\beta_{pq}^n z_n}}{e^{-j\beta_{pq}^n z_{n-1}} + \rho_{mpq}^n e^{+j\beta_{pq}^n z_{n-1}}} \quad (2.26a)$$

$$\tau_{mpq}^0 = \frac{e^{-j\beta_{pq}^0 z_0} + \rho_{mpq}^0 e^{+j\beta_{pq}^0 z_0}}{2\eta_{mpq}^0} \quad (2.26b)$$

Similarly working at Z_0 , the reflected field amplitude R_{mpq}^- can be arrived at

$$R_{mpq}^- = \rho_{m00}^0 T_{m00}^{inc} - \tau_{mpq}^0 \tau_{mpq}^1 \frac{\tilde{J}_{mpq}}{A} \quad (2.27)$$

Having attained reflected field amplitude, for the transmitted field amplitude; working at $Z = Z_1$ with R_{mpq}^1 from Eq.(2.25a)

$$T_{mpq}^1 e^{-j\beta_{pq}^1 z_1} + R_{mpq}^1 e^{+j\beta_{pq}^1 z_1} = T_{mpq}^1 \left(e^{-j\beta_{pq}^2 z_2} - \rho_{mpq}^1 e^{+j\beta_{pq}^2 z_2} \right) - \alpha \frac{\tilde{J}_{mpq}}{A} e^{-j\beta_{pq}^2 z_2} \quad (2.28)$$

Working towards $Z = Z_5$ with some algebraic manipulation, the transmitted field amplitude [4] can be arrived at

$$T_{mpq}^+ e^{-j\beta_{pq} z_5} = \tau_4^5 \tau_3^4 \tau_2^3 \tau_1^2 \tau_0^1 \left(e^{j\beta_{pq} z_0} (1 + \rho_{m00}^0) T_{m00}^{inc} - \Omega_{mpq} \frac{\tilde{J}_{mpq}}{A} \right) \quad (2.29)$$

$$\text{Where } \Omega_{mpq} = \tau_{mpq}^0 \tau_{mpq}^1 e^{j\beta_{pq} z_0} + \frac{e^{j\beta_{pq}^1 s_1} - e^{-j\beta_{pq}^1 s_1}}{2\eta_{mpq}^1} \quad (2.30)$$

Where s_1 is the thickness of the first layer dielectric substrate

2.2.2 Electric Field Integral equation (EFIE)

With the boundary condition, that is the electric field will vanish over the perfect conductor at $Z = Z_1$,

$$\underline{E}^I(\underline{r}, z_1) = 0 \quad \underline{r} \in A'$$

$$\sum_{mpq} \left(T_{mpq}^I e^{-j\beta_{pq}' z_1} + R_{mpq}^I e^{+j\beta_{pq}' z_1} \right) \Psi_{pq}(\underline{r}) \underline{\kappa}_{mpq} = 0 \quad (2.31)$$

Working with Eq.(2.28), substituting T_{mpq}^I into T_{mpq}^- and express it in terms of R_{mpq}^- using Eq. (2.27)

$$T_{mpq}^I e^{-j\beta_{pq}' z_1} + R_{mpq}^I e^{+j\beta_{pq}' z_1} = \tau_{mpq}^I \left(e^{j\beta_{pq} z_0} (1 + \rho_{m00}^0) T_{m00}^{inc} - \Omega \frac{\tilde{J}_{mpq}}{A} \right)$$

Substituting back to Eq.(2.31)

$$\sum_{mpq} \left[\tau_{mpq}^I \left(e^{j\beta_{pq} z_0} (1 + \rho_{m00}^0) T_{m00}^{inc} - \Omega \frac{\tilde{J}_{mpq}}{A} \right) \right] \Psi_{pq}(\underline{r}) \underline{\kappa}_{mpq} = 0$$

Therefore the Electric Field Integral equation (EFIE) is

$$\sum_{mpq} C_{mpq}^{scat} \tilde{J}_{mpq} \Psi_{pq}(\underline{r}) \underline{\kappa}_{mpq} = \sum_{m=1}^2 C_{m00}^{nsc} T_m^{inc} \Psi_{00}(\underline{r}) \underline{\kappa}_{m00} \quad (2.32)$$

Where

$$C_{mpq}^{scat} = \frac{\tau_{mpq}^I \Omega_{mpq}}{A} \quad (2.33a)$$

$$C_{m00}^{nsc} = e^{j\beta_{00} z_0} \tau_{m00}^I (1 + \rho_{m00}^0) \quad (2.33b)$$

2.3 Method of Moments

The Method of Moment (MoM) is used here is to solve the integral equation by reducing it to a linear system of simultaneous equations [5-6].

The purpose is to approximate the unknown current induced on the conductors within the unit cell in terms of an infinite series of N orthogonal basis functions. But the solution converges as $N \rightarrow \infty$. Therefore for computational efficiency, a certain N is chosen when the results converged. Although the approximation of the induced current will be better if N is increased, this is at the expense of computation time and resources. To save computation time and resources, a finite N is chosen such that with N increased the result will only differ by a very small amount. In section 4.2, N and the pq (Floquet modes) will be tested to ensure satisfactory modes are chosen to represent the problem.

With N series of basis functions, the induced current can be expressed as

$$\underline{J}(\underline{r}) = \sum_{n=1}^N c_n \underline{h}_n(\underline{r}_n) \quad \underline{r}_n \in A' \quad (2.34)$$

Where A' is the conducting area of the unit cell.

$\underline{h}_n(\underline{r}_n)$ are the current basis functions.

c_n are the complex amplitude of the unknown currents.

The choice of the basis functions depends on the type of conductor (dipole, tripole). The choice of basis functions for each type of conductor will be dealt with in their respective chapters (Section 4.2 and 5.1).

By substituting Eq.(2.34) into EFIE Eq.(2.32) and taking the inner product with the weighting functions h_i according to Galerkin's method, the result is in a set of equations that can be written in matrix form as:

$$\begin{bmatrix} \mathbf{Z}_{11} & \mathbf{Z}_{12} & \cdot & \cdot & \mathbf{Z}_{1N} \\ \mathbf{Z}_{21} & \mathbf{Z}_{22} & \cdot & \cdot & \mathbf{Z}_{2N} \\ \cdot & \cdot & \mathbf{Z}_{in} & \cdot & \cdot \\ \cdot & \cdot & \cdot & \cdot & \cdot \\ \mathbf{Z}_{M1} & \mathbf{Z}_{M2} & \cdot & \cdot & \mathbf{Z}_{MN} \end{bmatrix} \begin{bmatrix} \mathbf{c}_1 \\ \mathbf{c}_2 \\ \cdot \\ \cdot \\ \mathbf{c}_n \end{bmatrix} = \begin{bmatrix} \tilde{\mathbf{E}}_1^{nsc} \\ \tilde{\mathbf{E}}_2^{nsc} \\ \cdot \\ \cdot \\ \tilde{\mathbf{E}}_M^{nsc} \end{bmatrix} \quad (2.35)$$

Where $\tilde{\mathbf{E}}_i^{nsc}$ is the excitation vector. Eq.(2.36)

$[\mathbf{Z}_{MN}]$ is a matrix $M \times N$ and is independent of the excitation. Eq.(2.37)

\mathbf{c}_n is the unknown coefficient of the current

And

$$\tilde{\mathbf{E}}_i^{nsc} = \sum_{m=1}^2 C_{m00}^{nsc} T_{m00}^{inc} \tilde{h}^*(\underline{k}_{tpq}) \quad (2.36)$$

$$\mathbf{Z}_{in} = \sum_{mpq} C_{mpq}^{scat} \tilde{h}_i^*(\underline{k}_{tpq}) \tilde{h}_n(\underline{k}_{tpq}) \quad (2.37)$$

Where * is the conjugate

Here the weighting functions are the same as the basis functions; a method known as the Ritz-Galerkin method. Therefore to obtain the unknown coefficients \mathbf{c}_n in Eq.(2.35); a matrix inversion of $[\mathbf{Z}_{MN}]$ is performed which utilises the Crout's factorisation in a NAG routine [12] from the Numerical Algorithms Group Library (NAG).

$$[\mathbf{c}_n] = [\mathbf{Z}_{MN}]^{-1} [\tilde{\mathbf{E}}_i^{nsc}] \quad (2.38)$$

With the coefficients, \mathbf{c}_n computed, the unknown induced current can be determined from Eq.(2.34). Substituting the induced current Eq.(2.27) and Eq.(2.29), the reflected and the transmitted field amplitudes can be determined. And in Section 2.4, with the reflected and the transmitted fields, the reflection and transmission coefficients can be derived.

2.4 Reflection and Transmission Coefficients

This section is not used in the analysis of propagation constant along the surface for this research. However, for completeness sake, the study of FSS structures would require the attaining of reflection and transmission coefficients.

From electric field equation Eq.(2.15) and substituting the reflected field amplitude Eq.(2.27) into it and takes only the total reflected field at $Z = Z_0$.

$$\underline{E}_t^r(\underline{r}, z_0) = \sum_{mpq} R_{mpq}^- e^{+j\beta_{pq}z_0} \Psi_{pq}(\underline{r}) \underline{K}_{mpq} \quad (2.39)$$

The zero order mode being the dominant mode and always propagating; the total reflected electric field is given by

$$\underline{E}_t^r(\underline{r}, z_0) = \sum_m \rho_{m00}^0 T_{m00}^{inc} \Psi_{00}(\underline{r}) \underline{k}_{m00} - \sum_{mpq} \tau_{mpq}^0 \tau_{mpq}^I \frac{J_{mpq}}{A} \Psi_{pq}(\underline{r}) \underline{K}_{mpq} \quad (2.40)$$

And for the total tangential transmitted electric field at $Z = Z_5$

$$\underline{E}_T^t(\underline{r}, z_5) = \sum_{mpq} T_{mpq}^+ e^{-j\beta_{pq}z_5} \Psi_{pq}(\underline{r}) \underline{K}_{mpq} \quad (2.41)$$

Likewise substituting the transmitted field amplitude Eq.(2.29) into the total tangential transmitted electric field. Eq.(2.41)

$$\begin{aligned} \underline{E}_T^t(\underline{r}, z_5) = & \tau_{mpq}^\alpha \sum_{mpq} e^{j\beta_{pq}z_0} (1 + \rho_{m00}^0) T_{m00}^{inc} \Psi_{00}(\underline{r}) \underline{K}_{m00} \\ & - \sum_{mpq} \Omega_{mpq} \frac{J_{mpq}}{A} \Psi_{pq}(\underline{r}) \underline{K}_{mpq} \end{aligned} \quad (2.42)$$

$$\text{Where } \tau_{mpq}^{\alpha} = \tau_{mpq}^5 \tau_{mpq}^4 \tau_{mpq}^3 \tau_{mpq}^2 \tau_{mpq}^1$$

The total reflected electric field at $Z = Z_0$ and total transmitted electric field at $Z = Z_5$ can also be expressed in terms of

$$\underline{E}^{rT}(\underline{r}, z_0) = \left(R_x^r \hat{x} + R_y^r \hat{y} + R_z^r \hat{z} \right) e^{j\beta_{pq}z_0} \Psi_{pq}(\underline{r}) \quad (2.43)$$

$$\text{Where } R_x^r = R_{mpq}^- \underline{K}_{m00x} \quad (2.43a)$$

$$R_y^r = R_{mpq}^- \underline{K}_{m00y} \quad (2.43b)$$

$$R_z^r = -\frac{\left(R_x^r \sin\theta \cos\phi + R_y^r \sin\theta \sin\phi \right)}{\cos\theta} \quad (2.43c)$$

The total transmitted electric field at $Z = Z_5$

$$\underline{E}^{tT}(\underline{r}, z_5) = \left(T_x^t \hat{x} + T_y^t \hat{y} + T_z^t \hat{z} \right) e^{-j\beta_{pq}z_5} \Psi_{pq}(\underline{r}) \quad (2.44)$$

$$\text{Where } T_x^t = T_{mpq}^+ \underline{K}_{m00x} \quad (2.43a)$$

$$T_y^t = T_{mpq}^+ \underline{K}_{m00y} \quad (2.43b)$$

$$T_z^t = -\frac{\left(T_x^t \sin\theta \cos\phi + T_y^t \sin\theta \sin\phi \right)}{\cos\theta} \quad (2.43c)$$

The copolar components of the total reflected and transmitted field are obtained by projecting them onto the total incident field direction \underline{B}^i

$$\underline{E}^{rc}(\underline{r}, z_0) = E^{rc}(\underline{r}, z_0) \underline{B}^{inc} \quad (2.44)$$

$$\text{Where } E^{rc}(\underline{r}, z_0) = \underline{E}^{rT}(\underline{r}, z_0) \cdot \underline{B}^{inc}$$

And for the copolar component of the transmitted electric field

$$\underline{E}^{tc}(\underline{r}, z_5) = E^{tc}(\underline{r}, z_5) \underline{B}^{inc} \quad (2.45)$$

Where $E^{tc}(\underline{r}, z_5) = \underline{E}^{tT}(\underline{r}, z_5) \cdot \underline{B}^{inc}$

For a given FSS with a plane wave incident at an arbitrary direction with the angle θ to the Z-axis; the reflection and transmission coefficient in the copolar direction is given as,

$$R_{coeff}^{cpo} = \frac{E^{rc}(\underline{r}, z_0)}{E^{Tinc}(\underline{r}, z_0)} = R_x^r B_x^{inc} + R_y^r B_y^{inc} + R_z^r B_z^{inc} \quad (2.46)$$

$$T_{coeff}^{cpo} = \frac{E^{tc}(\underline{r}, z_5)}{E^{Tinc}(\underline{r}, z_5)} = T_x^t B_x^{inc} + T_y^t B_y^{inc} + T_z^t B_z^{inc} \quad (2.47)$$

2.5 Propagation along the surface (X-Y plane)

The purpose of this research is to determine if there exist any bandgap (stopband) that appeared in the 2-D plane of periodicity. Thus it is essential to explore all possible propagation mode that exist along the two dimensional plane of the array. For the analysis of propagation along the xy plane the angle θ from Eq.(2.5) is set to 90° giving

$$\underline{k}_{tpq} = \underline{k}_{t00} + p\underline{k}_1 + q\underline{k}_2 \quad (2.48)$$

$$\text{Where } \underline{k}_{T00} = \underline{k}_{00x} + \underline{k}_{00y} \quad (2.48a)$$

$$= k_0 \sin \theta \cos \phi + k_0 \sin \theta \sin \phi$$

And $\sin \theta = 1$

For a lossless case, $k_{00x} = \beta_x$, $k_{00y} = \beta_y$

The analysis is similar to that described in the derivation for the planar FSS problem up to the Method of Moments in Eq.(2.35). Solving for the total fields where $\underline{E}^i + \underline{E}^s = 0$, the equation Eq.(2.35) becomes

$$\begin{bmatrix} Z_{11} & Z_{12} & \cdot & \cdot & Z_{1N} \\ Z_{21} & Z_{22} & \cdot & \cdot & Z_{2N} \\ \cdot & \cdot & Z_{in} & \cdot & \cdot \\ \cdot & \cdot & \cdot & \cdot & \cdot \\ Z_{M1} & Z_{M2} & \cdot & \cdot & Z_{MN} \end{bmatrix} \begin{bmatrix} c_1 \\ c_2 \\ \cdot \\ \cdot \\ c_n \end{bmatrix} = \begin{bmatrix} 0 \\ 0 \\ \cdot \\ \cdot \\ 0 \end{bmatrix} \quad (2.49)$$

$$\text{which is } [Z_{mn}][c_n] = [0] \quad (2.50)$$

For this set of homogeneous linear equation to have non-trivial solutions [13], the determinant of the matrix $[Z]$ must be zero. This is known as the characteristic determinant of $[Z]$. Likewise, with Eq.(2.37), the matrix $[Z]$ is determined with another NAG routine [12] which also utilises Crout's factorisation to determine the characteristic

determinant. By varying the β from zero to the boundary of the irreducible Brillouin zone (see explanation in Section 2.6), all the corresponding characteristic determinants of $[Z]$ are plotted out for each β . From the characteristic determinant plot, all the true set minima obtained correspond to each individual propagation mode.

In Figure 2.5, an example shows a graph of computed characteristic determinant. In this case, β is varied from 0 to π/a (boundary of the irreducible Brillouin zone). From the graph, it shows that there is a propagation mode for β normalised values 0.133, 0.152, 0.173, 0.193 and 0.22 at frequencies 5.5 GHz, 6 GHz, 6.5 GHz, 7 GHz and 7.5 GHz.

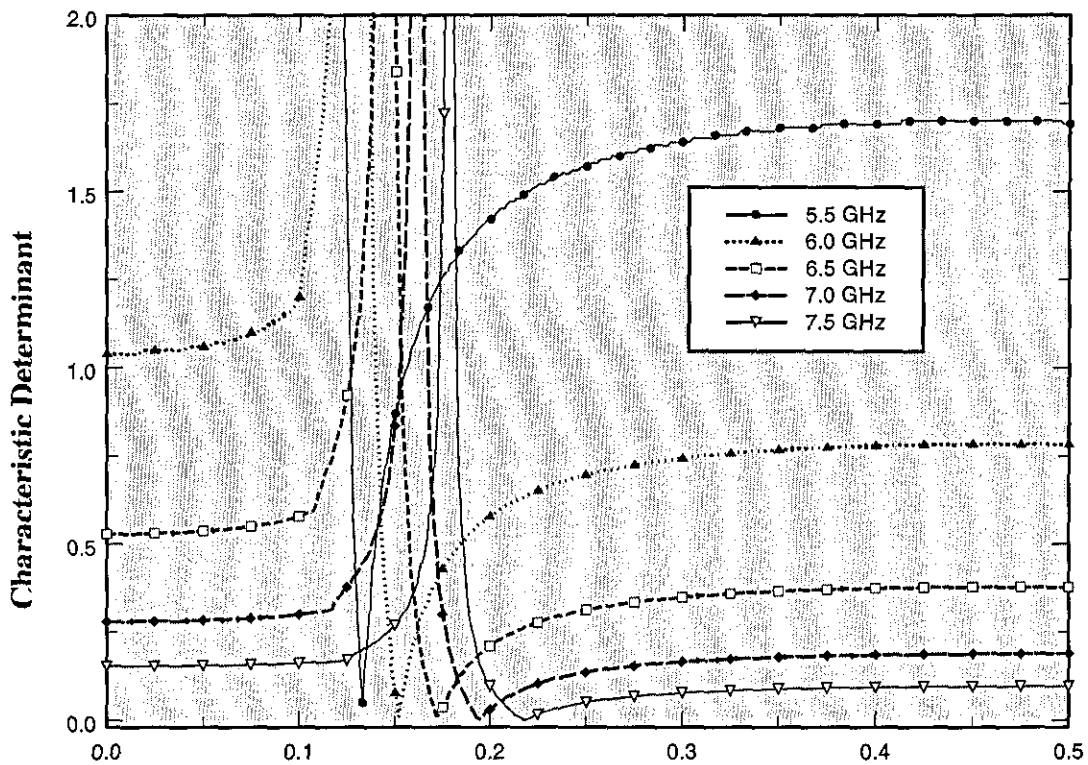


Figure 2.5 : Propagation mode determined from the plot of characteristic determinant

Using a simple bisection method, which is evaluating the characteristic determinant values before and after each point; all the propagation constants associate to each of the minima, are recorded.

By exploring the whole 2-D irreducible Brillouin zone, all the possible modes that exist on the x - y plane could be found. For the range of frequencies where there is an absence of any propagation mode, that range of frequencies is considered a bandgap (stopband).

2.6 Direct and Reciprocal Lattices in Two Dimensions

A direct lattice describes the way the physical elements are arranged [11]. Usually it is a periodic array in which the identical elements are spaced at equal distances from one another along two lines intersecting at an arbitrary angle α . In other words, it is an array with an arrangement and orientation that appears exactly the same from whichever point the array is viewed. This type of lattice is also called a Bravais lattice. From the triangular lattice shown in Figure 2.6, taking a_1 and a_2 as basis vectors drawn from the element chosen as the origin of the lattice. The vector coordinate of any element in the lattice is given by

$$R_{n_1, n_2} = n_1 a_1 + n_2 a_2 \quad (2.51)$$

Where n_1 and n_2 are integers.

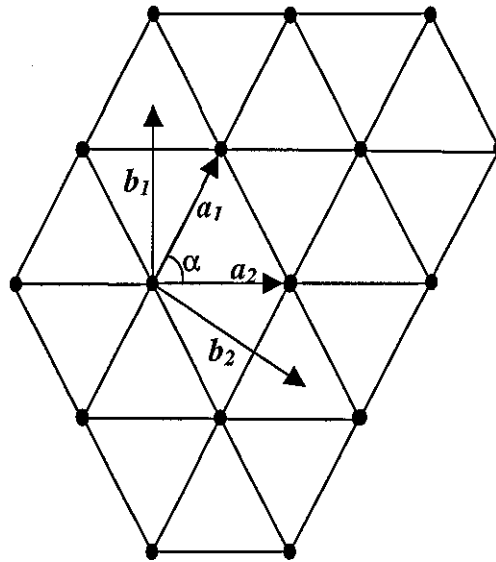


Figure 2.6 : Direct Triangle Lattice

From the direct lattice, the vectors a_1 and a_2 , if written in their matrix Cartesian coordinates as row vectors are given by:

$$A = \begin{bmatrix} a_{1X} & a_{1Y} \\ a_{2X} & a_{2Y} \end{bmatrix} \quad (2.52)$$

The concept of a reciprocal lattice can be found in many solid-state physics book [7 – 11]. From the example above, the reciprocal lattice which is transposed from the matrix A will arrange its vectors b_1 and b_2 as column vectors:

$$B = \begin{bmatrix} b_{1X} & b_{2X} \\ b_{1Y} & b_{2Y} \end{bmatrix} \quad (2.53)$$

For the given direct lattice with vectors a_1 and a_2 ; a reciprocal lattice can be define with its own basis vector b_1 and b_2 given by the Eq.(2.53).

$$(a_i \cdot b_k) = \delta_{ik} \quad \text{where } i = 1,2 \quad (2.54)$$

$$k = 1,2$$

Where δ_{ik} is the Kronecker δ symbol, defined by

$$\delta_{ik} = 1 \quad i = k \quad (2.56)$$

$$= 0 \quad i \neq k$$

Therefore the matrix product of the direct lattice and the reciprocal lattice are:

$$A \cdot B = \begin{bmatrix} a_{1X} & a_{1Y} \\ a_{2X} & a_{2Y} \end{bmatrix} \begin{bmatrix} b_{1X} & b_{2X} \\ b_{1Y} & b_{2Y} \end{bmatrix} \quad (2.57)$$

$$= \begin{bmatrix} (a_1 \cdot b_1) & (a_1 \cdot b_2) \\ (b_2 \cdot a_1) & (a_2 \cdot b_2) \end{bmatrix}$$

From Eq.(2.56),

$$A \cdot B = \begin{bmatrix} 1 & 0 \\ 0 & 1 \end{bmatrix} = U \quad (2.58)$$

Where U is the unit matrix. From this it follows that

$$B = A^{-1}$$

$$B = \frac{1}{|A|} \times C^T \quad (2.59)$$

Where C^T is the adjoint of matrix A

And matrix C consist the cofactors of the elements in A

It can be concluded from the above equation, Eq.(2.59), that a_1 is perpendicular to b_2 and a_2 is perpendicular to b_1 (see Figure 2.6). The components of the reciprocal lattice can be obtained from the direct lattice by the relationship given by Eq.(2.59) [8]:

$$b_{1X} = \frac{a_{2Y}}{a_{1X} a_{2Y} - a_{1Y} a_{2X}} \quad b_{2X} = \frac{-a_{1Y}}{a_{1X} a_{2Y} - a_{1Y} a_{2X}}$$

$$b_{1Y} = \frac{-a_{2X}}{a_{1X} a_{2Y} - a_{1Y} a_{2X}} \quad b_{2Y} = \frac{a_{1X}}{a_{1X} a_{2Y} - a_{1Y} a_{2X}}$$

With a hexagonal direct lattice based on the vectors a_1 and a_2 with an angle α of $\pi/3$ between them, the respective reciprocal lattice is another hexagonal lattice, turned through an angle $\pi/6$ with vectors b_1 and b_2 .

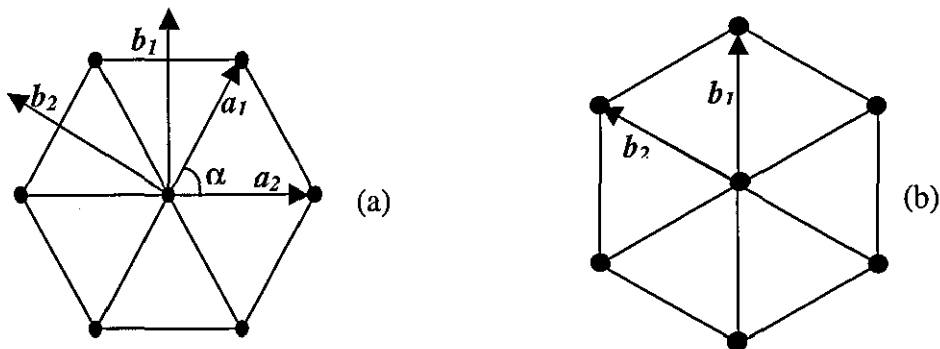


Figure 2.7 : (a) The direct lattice and (b) its respective reciprocal lattice

The parallelogram formed by b_1 and b_2 defines the unit cell of the two dimensional reciprocal lattice (Figure 2.8). The reciprocal lattice is also a periodic array with its elements spaced at equal distances from one another along two lines, b_1 and b_2 , intersecting at a arbitrary angle which in this case is also equal α .

However, it is more convenient to build a unit cell of the same area but which is symmetrical with respect to the elements of the reciprocal lattice Figure 2.8 [11]. This is defined as the two dimensional first Brillouin zone. The first Brillouin zone also known as the Wigner-Seitz cell [12] of the reciprocal lattice, states that the region of space in the reciprocal lattice that is closer to the lattice element than any other, is known the first Brillouin zone. For each element, there exists higher order zones and each of these zones covers an area equal to that of the first zone.

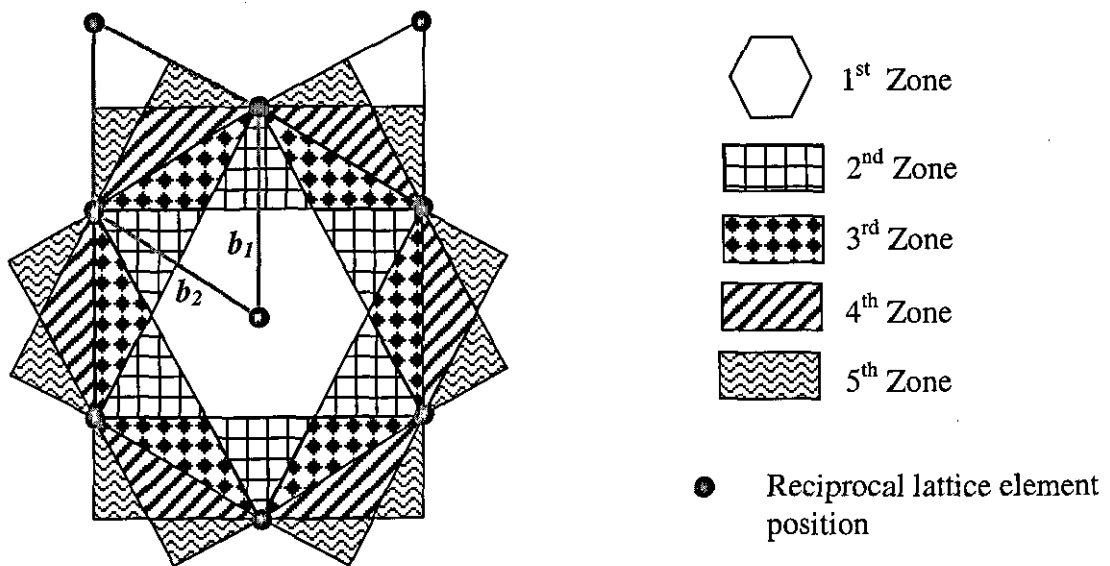


Figure 2.8 : The reciprocal lattice of Figure 2.6 and its zones distribution

Any individual zone can be reduced to the first zone by taking its sections and giving them a translation parallel and equal to one of the vectors of the reciprocal lattice. This is obvious for the second zone in Figure 2.8. For the third zone, by a mosaic arrangement, the different sections of the third zone can be exactly put together to cover the first one given the necessary translation.

Due to the symmetric and periodic properties within the first Brillouin zone, the smallest region (the shaded portion in Figure 2.9) of the first Brillouin zone is irreducible. Thus it will be sufficient to just consider only the irreducible zone as the rest are just mirror images of it.

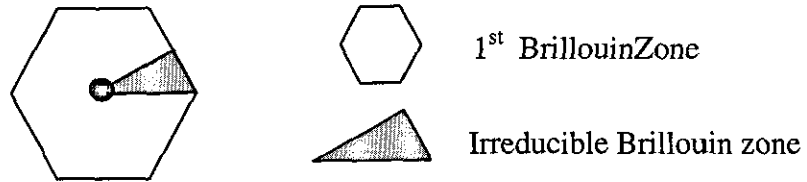


Figure 2.9 : The irreducible first Brillouin zone

As another example, for a two dimension square direct lattice, the corresponding reciprocal lattice is also a square lattice with its vector b .

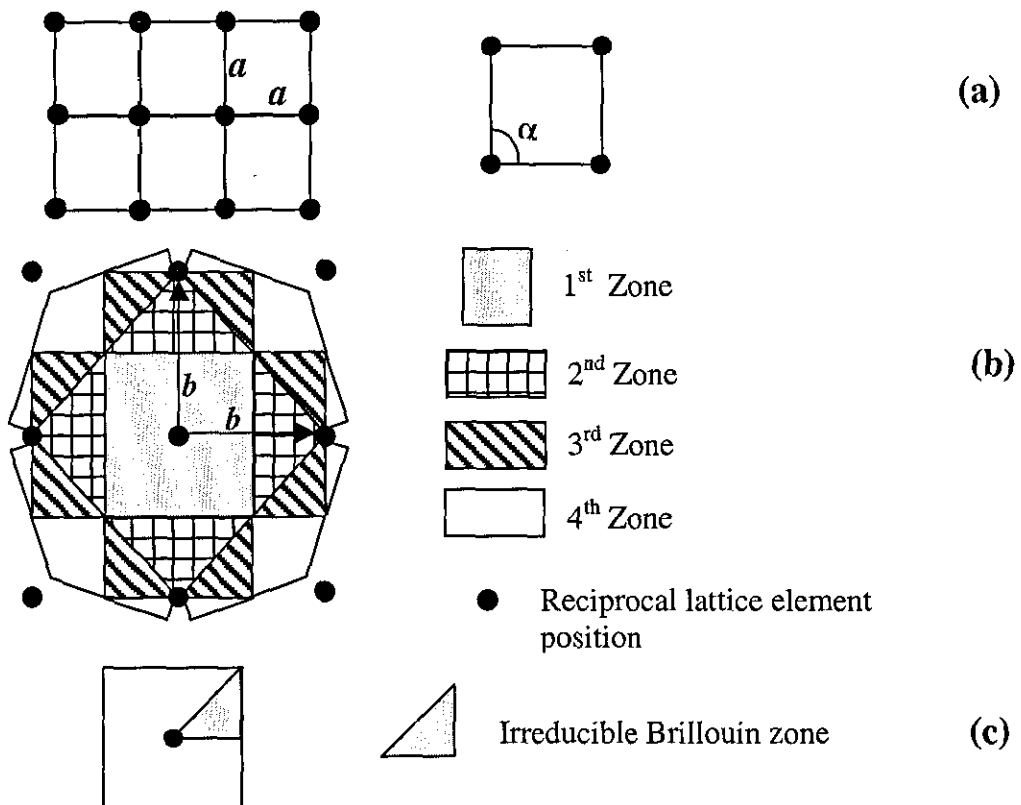


Figure 2.10 : (a) Square direct lattice, (b) the respective reciprocal lattice, (c) its irreducible first Brillouin zone

2.6.1 Irreducible Brillouin zone and the array element

It has been discovered in the course of this research through modeling results from the whole first Brillouin zone that the irreducible Brillouin zone also depends on the circularly symmetrical nature of the array element. This is also been verified in both the modeling and measurement results for dipole arrays in Chapter 4. The angles between lines of symmetry for the array element and the first Brillouin zone of the lattice must be taken into the consideration. The larger angle of the two symmetry properties is chosen for the irreducible Brillouin zone provided that the smaller angle is a multiple factor of it. If not, the next larger angle is chosen as the irreducible Brillouin zone which is a multiple factor of the two angles.

As in Figure 2.9, if the array element is assumed to have circular symmetry like a dot or circle, the irreducible Brillouin zone will be determined by the angle between the lines of symmetry of its first Brillouin zone. In Figure 2.11a, for a triangular lattice, the angle between the lines of symmetry of its first Brillouin zone is 30° . For the square lattice in Figure 2.11b the angle will be 45° .

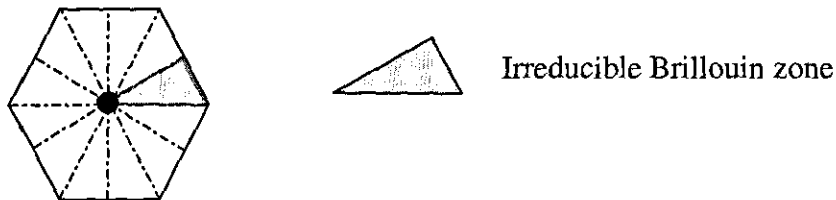


Figure 2.11a : Lines of symmetry in the first Brillouin zone of a triangular lattice

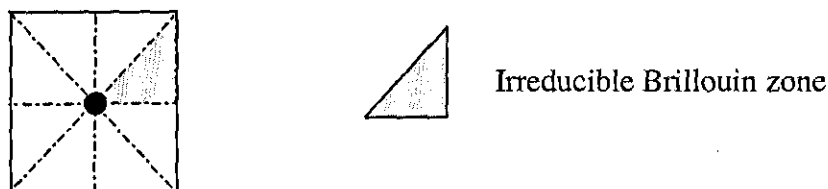


Figure 2.11b : Lines of symmetry in the first Brillouin zone of a square lattice

In the case of a dipole as the array element, it has only two lines of symmetry (Figure 2.12a). Thus the dipole is only quarterly circular symmetric (90°). Whereas the angle of symmetry for first Brillouin zone of a square and triangular lattice is 45° and 30° (Figure 2.11a,b) respectively. Therefore the irreducible Brillouin zone must cover at least 90° of the first Brillouin zone. (Figure 2.12)

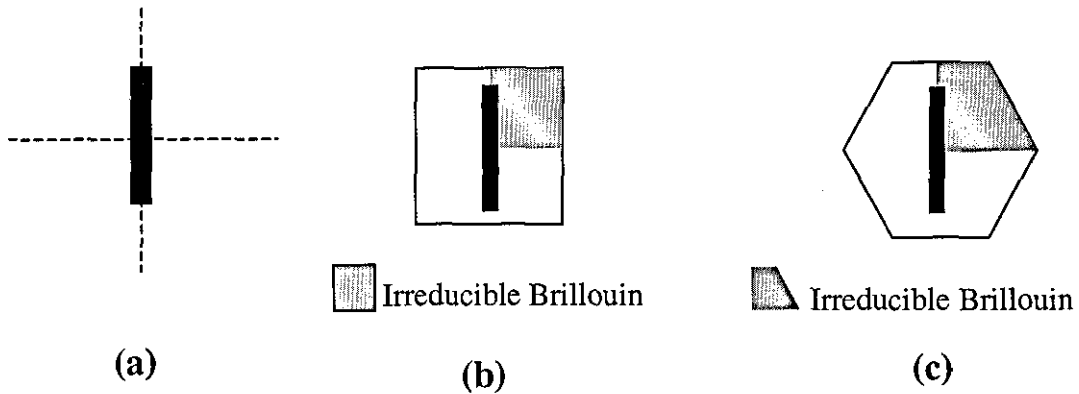


Figure 2.12 : (a) Line of symmetry of the dipole, (b) Irreducible first Brillouin zone of a dipole in a square reciprocal lattice. (c) Irreducible first Brillouin zone of a dipole in a hexagonal reciprocal lattice.

For the tripole array element, the response depends on the contribution of the current in each of the three legs of the tripole. The response would be the same in the direction of A and A', B and B' and C and C'. Thus the angle of symmetry for the tripole array is 30° , coincidentally for the first Brillouin zone of the triangular lattice is also 30° (Figure 2.13). So the irreducible Brillouin zone will be 30° .

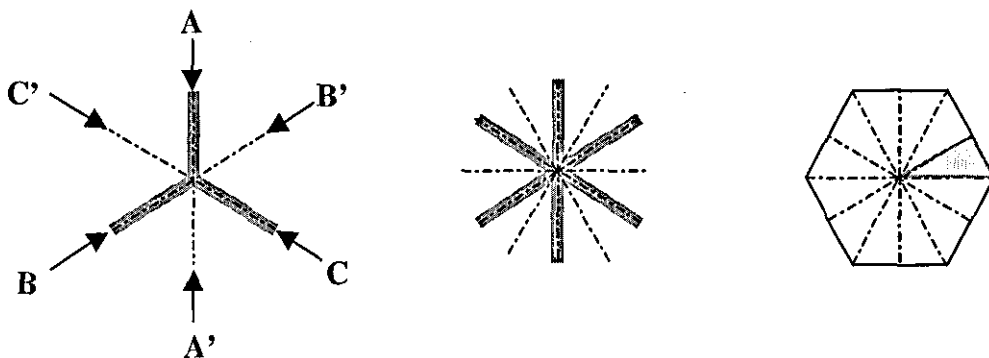


Figure 2.13 : Lines of symmetry for a tripole and the first Brillouin zone of a triangular lattice

For a tripole on a square lattice, the angle of symmetry for its first Brillouin zone is 45° and the angle of symmetry for the tripole array is 30° . The angle of 45° cannot be chosen as the irreducible Brillouin zone because 30° is not a factor of it, thus the next higher angle is chosen. In this case it is 90° which both angles are a factor of it.

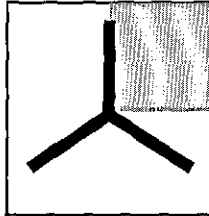


Figure 2.14 : The irreducible Brillouin zone of a tripole in a square lattice.

2.7 Conclusions

This chapter discusses the theory of the research, which draws upon techniques used in analysis of FSS. Changes were made for the first time to the computer modelling to enable calculation of propagation modes in the plane of the array. In the first part of this chapter, the modal analysis used for FSS is presented in detail in Sections 2.1-2.4.

The difference in the analysis of band gap for the array in the xy plane is presented in Section 2.5. The analysis of propagation along the surface is achieved by evaluating the propagation constant within the irreducible Brillouin zone to predict the propagation modes in all directions within the two dimensional plane.

Finally, in Section 2.6, the reciprocal lattice and its respective Brillouin zone are presented. It is found that the symmetrical relationship of the first Brillouin zone of the lattice and the array elements do play a part in determining the irreducible first Brillouin zone.

REFERENCES

- [1] AMITAY, N., GALINDO, V. and WU, C.P.: 'Theory and Analysis of Phased Array Antennas' ,New York, NY: Wiley-Interscience, 1972, pp.37-42 and 310-313.
- [2] CHEN, C.C.: 'Scattering by a two dimensional periodic array of conducting plates', IEEE Transactions on Antennas and Propagation, Vol. AP-18, No 5, September 1970, pp. 660 – 665.
- [3] MONTGOMERY, J.P.: 'Scattering by an infinite periodic array of thin conductors on a dielectric sheet', IEEE Transactions on Antennas and Propagation, Vol. AP-23, No 1, January 1975, pp. 70-75.
- [4] VARDAXOGLU J.C.: 'Frequency Selective Surfaces : Analysis and Design.' , Research Studies Press, 1997, Chapter 2.
- [5] HARRINGTON R.F.: 'Matrix methods for field problems' , Proc. IEEE, Vol 55, No2, February 1967, pp. 136-149.
- [6] HARRINGTON R.F.: 'Field Computation by Moment Methods', New York: MacMillian, 1968.
- [7] BRILLOUIN L.: 'Wave Propagation in Periodic Structures.', Dover Publications, 1953, Chapter 6.
- [8] DESJONQUERES M. C. and SPANJAARD D.: 'Concepts in Surface Physics.' , Springer –Verlag, 1993, Chapter 3.
- [9] ASHCROFT N.W. and MERMIN N.D.: 'Solid State Physics' , Saunders College, 1976, Chapter 4-5.

- [10] KITTEL,C. : 'Introduction to Solid State Physics', John Wiley, 1996, Chapter 1-2.

- [11] JOANNOPOULOS J.D. MEADE R.D. ,WINN J.N.: 'Photonic Crystals–Molding the Flow of Light.' Princeton University Press. 1995.

- [12] 'Subroutine F04ADF and F03ADF', Numerical Algorithm Group (NAG) MK. 13.

- [13] STROUD K.A.: 'Further Engineering Mathematics' , English Language Book Society/Macmillan. 1990, Program 11.

Chapter 3

Surface Waves on a Dielectric Slab

3.0 Introduction

A surface wave is defined simply as a wave propagating along an interface between two different media without radiating. It is distinguished from a leaky wave by the fact that there is not a continuous radiation of energy but rather a wave that is bounded closely to the surface. The chief characteristic of a surface wave is that its phase velocity is less than the surrounding medium, which is usually free space. Another characteristic is that for a plane uniform structure, the fields decay exponentially away from the structure [1].

Surface waves have been investigated here on two types of dielectric slabs; the dielectric slab with and without a ground plane [2-4].

For the propagating modes on the dielectric slab, there exist similar modes for a dielectric slab with twice the thickness as one with a ground plane. So the evaluation in this Chapter is of a dielectric slab with a thickness $2d$ and a grounded dielectric slab with a dielectric thickness of d .

The planar structure lies in the y - z plane with the propagation in the z direction.

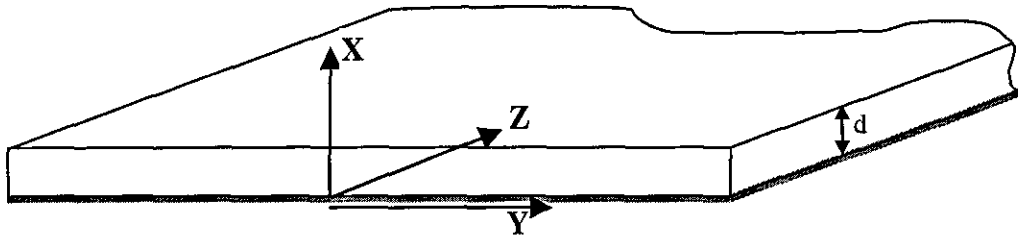


Figure 3.1 : Geometry of a grounded dielectric slab with thickness d

3.1 Propagation Modes of a Dielectric Slab on a Ground Plane

3.1.1 TM modes

For the TM modes ($H_z = 0$) and no variation in the y -direction ($\frac{\partial}{\partial y} = 0$), E_z is obtained from the wave equation for each region [2].

$$\left(\frac{\partial}{\partial x^2} + \epsilon_r k_0^2 - \beta^2 \right) e_z(x, y) = 0 \quad 0 \leq x \leq d \quad (3.1)$$

$$\left(\frac{\partial}{\partial x^2} + k_0^2 - \beta^2 \right) e_z(x, y) = 0 \quad 0 \leq x \leq \infty \quad (3.2)$$

Where $E_z(x, y, z) = e_z(x, y) e^{-j\beta z}$

$$k_c^2 = \epsilon_r k_0^2 - \beta^2 \quad (3.3)$$

$$h^2 = \beta^2 - k_0^2 \quad (3.4)$$

The cutoff wave number for the two regions is expressed in Eq.(3.3) and Eq.(3.4).

Matching the solution of Eq.(3.1) and Eq.(3.2), the general solution is

$$e_z(x, y) = A \sin k_c x + B \cos k_c x \quad 0 \leq x \leq d \quad (3.5)$$

$$e_z(x, y) = C e^{hx} + D e^{-hx} \quad 0 \leq x \leq \infty \quad (3.6)$$

With $E_z(x, y, z)$ specified in its respective regions, Eq.(3.6) is equal:

$$E_z(x, y, z) = 0 \quad X = 0 \quad (3.6a)$$

$$E_z(x, y, z) < \infty \quad X \rightarrow \infty \quad (3.6b)$$

$$E_z(x, y, z) \text{ continuous} \quad X = d \quad (3.6c)$$

$$H_y(x, y, z) \text{ continuous} \quad X = d \quad (3.6d)$$

And by matching the boundary condition at $x = d$. The continuity of E_x and H_y lead Eq.(3.4) and Eq.(3.5) to

$$k_c \tan k_c d = \epsilon_r h \quad (3.7)$$

The plot of the positive real solutions of Eq.(3.6) implies that TM modes exist on the grounded dielectric slab. It is shown in the plot of Eq.(3.6) [2] with any non-zero thickness of dielectric slab, there is at least one propagating mode which is the TM_0 . This is the dominant mode that has zero cutoff frequency.

The cutoff frequencies of all the TM modes are defined as

$$f_c = \frac{nc}{2d\sqrt{\epsilon_r - 1}} \quad n = 0, 1, 2, 3, \dots \quad (3.8)$$

Where d is the thickness of the dielectric slab

Or

$$\frac{d}{\lambda_0} = \frac{n}{2\sqrt{\epsilon_r - 1}} \quad n = 0, 1, 2, 3, \dots \quad (3.9)$$

3.1.2 TE modes

Likewise for TE modes ($E_z = 0$), the H_z field for the two regions are

$$\left(\frac{\partial}{\partial x^2} + k_c^2 \right) h_z(x, y) = 0 \quad 0 \leq x \leq d \quad (3.10)$$

$$\left(\frac{\partial}{\partial x^2} + h^2 \right) h_z(x, y) = 0 \quad 0 \leq x \leq \infty \quad (3.11)$$

Where $H_z(x, y, z) = h_z(x, y) e^{-j\beta z}$

Where K_c is defined in Eq.(3.3) and h^2 in Eq.(3.4), the general solution of Eq.(3.10) and Eq.(3.11) is

$$h_z(x, y) = A \sin k_c x + B \cos k_c x \quad 0 \leq x \leq d \quad (3.12)$$

$$h_z(x, y) = C e^{hx} + D e^{-hx} \quad 0 \leq x \leq \infty \quad (3.13)$$

Likewise with the solution from $H_z(x, y)$ and the cutoff wave numbers of both region, by matching the boundary condition at $x = 0$ and $x = d$. The field of E_y and continuity H_y lead Eq.(3.12) and Eq.(3.13) to

$$-k_c \cot k_c d = h \quad (3.14)$$

Plotting out Eq.(3.14) which is a cotangent function (with positive real solutions) implied that there is no TE_0 mode on the grounded dielectric slab. It is shown in the plot of Eq.(3.14), that the first TE mode is TE_1

The cutoff frequencies of the TE modes are

$$f_c = \frac{(2n-1)c}{2d\sqrt{\epsilon_r - 1}}, \quad n = 0, 1, 2, 3, \dots \quad (3.15)$$

And the TE modes are

$$\frac{d}{\lambda_0} = \frac{(2n-1)}{4\sqrt{\epsilon_r - 1}} \quad n = 0, 1, 2, 3, \dots \quad (3.16)$$

The propagation modes that exist for a grounded dielectric slab stated in [3-4] is said to be TM (EVEN) and TE (ODD) such as $TM_0, TE_1, TM_2, TE_3, TM_4, \dots$

As for a dielectric slab without a ground plane, it will exhibit both TM (EVEN and ODD) and TE (EVEN and ODD) modes [2,3]. If the dielectric slab without a ground plane has twice the thickness as a grounded dielectric slab; their TM (EVEN) and TE (ODD) will be the same.

3.2 Program simulation and results

From the theory in Section 2.5, computer simulations were carried out to check if they could predict propagation modes along the surface of the dielectric substrate, in another words along the x - y plane specified in Section 2.5.

By setting the parameters of the conducting elements of the array to be infinitely small. The array will be almost nonexistent on the dielectric sheet, thus it should provide the same response as a normal dielectric slab.

To simulate a dielectric slab with a ground plane, a very thin layer with a very high loss tangent is introduced behind the dielectric sheet. Alternatively for its respective dielectric slab without a ground plane, the dielectric thickness is doubled.

With the simulation of each frequency, the values of β are obtained at the occurrence of each characteristic determinant minima. These β are associated with each of the true minima for the predicted propagation modes of the surface waves that exist on the dielectric structure.

For comparison, the example in [2] is used and the result for each mode is calculated.

The example given is a grounded dielectric slab with $\epsilon_r = 2.55$ and thickness $d = 6\text{mm}$, plotting d/λ_0 with β/k_0 in Figure 3.2.

Applying Eq.(3.8) and Eq.(3.9) for TM modes (EVEN),

$$\text{TM}_0, \quad f_c = 0 \text{ Ghz}; \quad \frac{d}{\lambda_0} = 0$$

$$\text{TM}_2, \quad f_c = 20 \text{ Ghz}; \quad \frac{d}{\lambda_0} = 0.4016$$

$$\text{TM}_4, \quad f_c = 40 \text{ Ghz}; \quad \frac{d}{\lambda_0} = 0.8032$$

Applying Eq.(3.15) and Eq.(3.16) for TE modes (ODD),

$$\text{TE}_1, \quad f_c = 10 \text{ Ghz}; \quad \frac{d}{\lambda_0} = 0.2008$$

$$\text{TE}_3, \quad f_c = 30 \text{ Ghz}; \quad \frac{d}{\lambda_0} = 0.6024$$

The comparisons between simulated results for the grounded dielectric slab and the example from Pozar [2] shown in Figure 3.2 are in excellent agreement.

The simulated results for a dielectric slab without the ground plane (Figure 3.3a and Figure 3.3b) with twice the thickness also show that its TM (EVEN) and TE (ODD) are in excellent agreement with the example in [2].

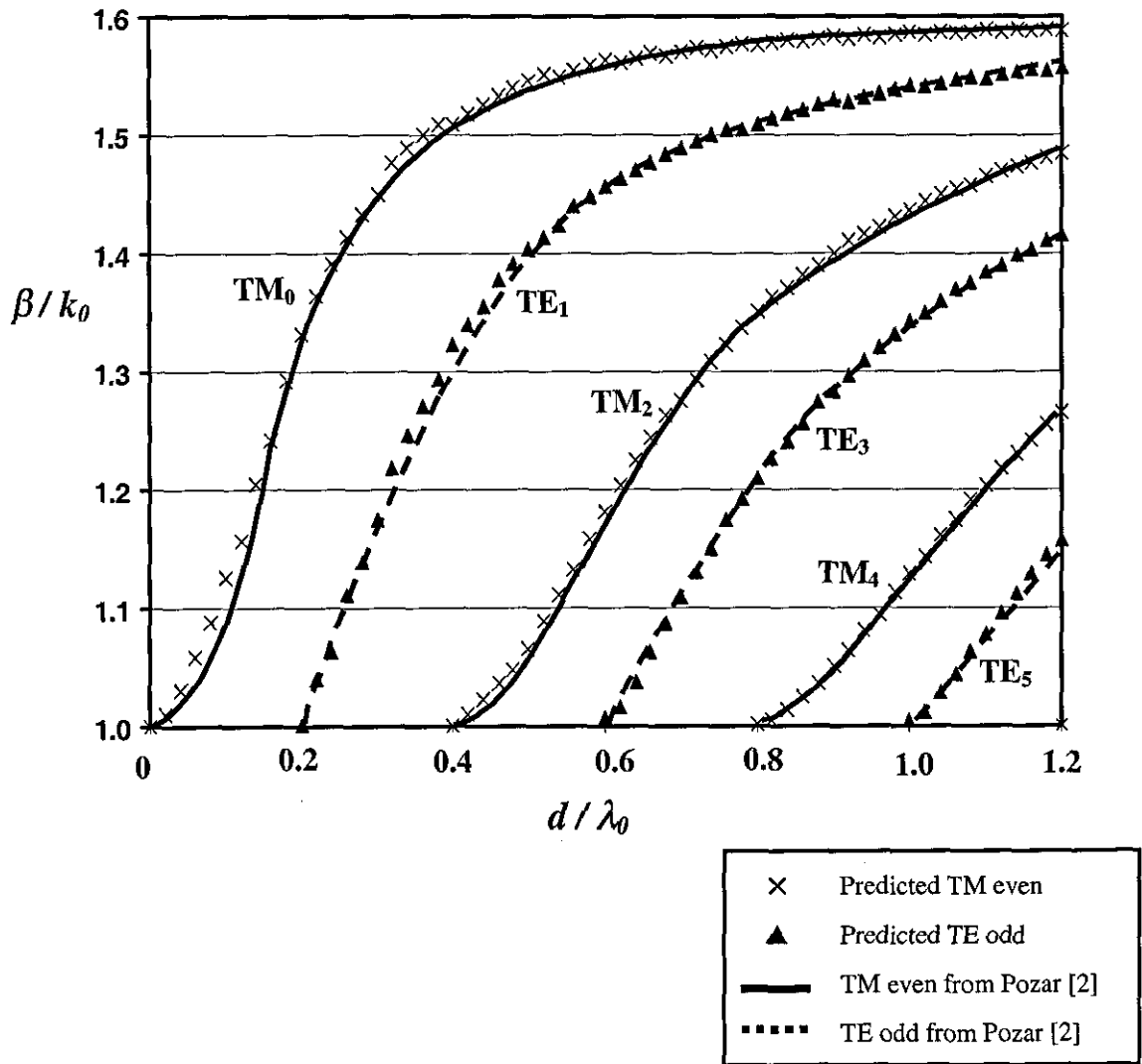


Figure 3.2 : Simulation results for TM EVEN and TE ODD modes of a grounded dielectric slab with $\epsilon_r = 2.55$, TM Even and TE odd from Pozar [2] example.

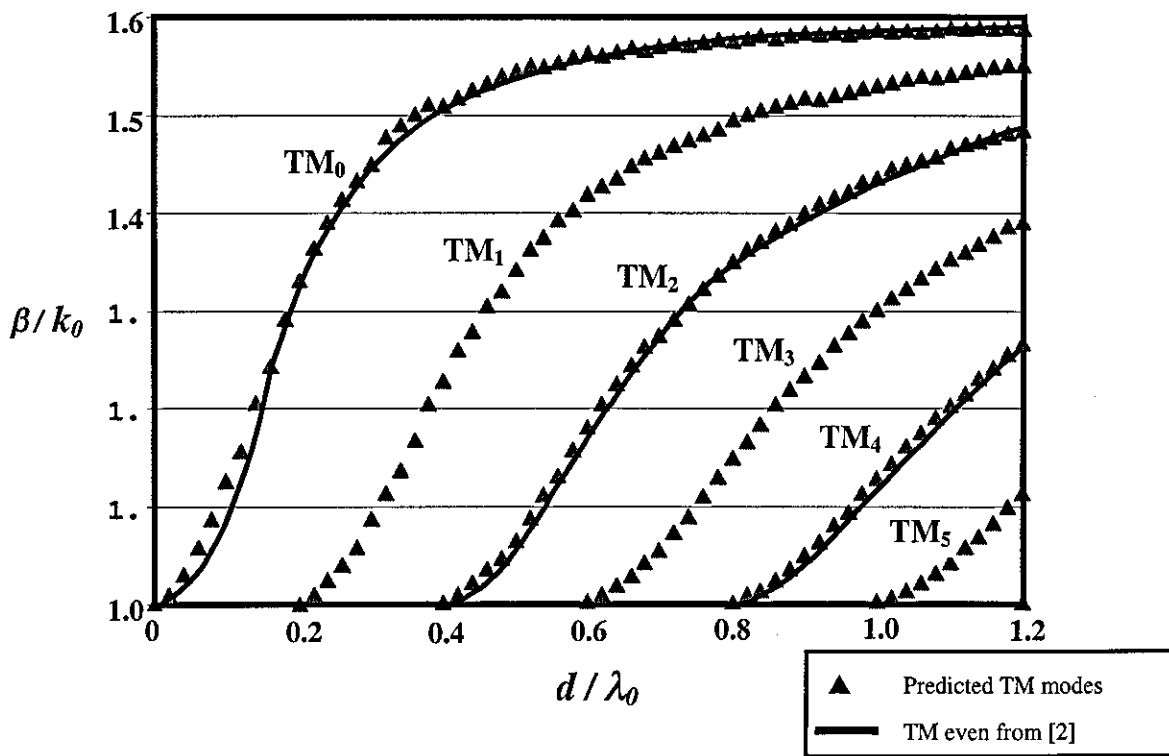


Figure 3.3a : Simulation results for TM ODD and EVEN modes of a dielectric slab with thickness $2d$, TM EVEN from Pozar [2] of a grounded dielectric slab with thickness d .

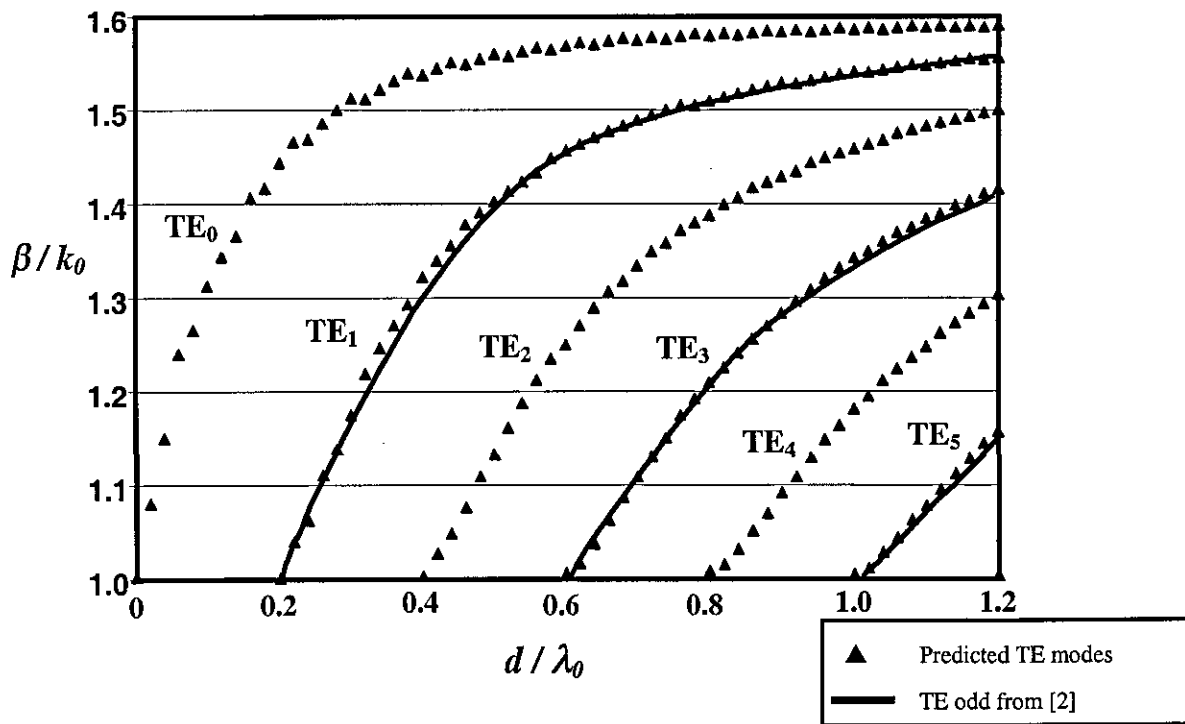


Figure 3.3b : Simulation results for TE ODD and EVEN modes of a dielectric slab with thickness $2d$, TE ODD from Pozar [2] of a grounded dielectric slab with thickness d .

3.3 Conclusions

This chapter looked into surface waves that exist on the dielectric slab with and without a ground plane. From the theory in Section 2.5, the program simulation was carried out to derive the propagation constant along the surface of the dielectric substrate.

By setting the parameters of the conducting elements of the array to be infinitely small. The array will be almost nonexistent on the dielectric sheet and it provided the same response as a normal dielectric slab. To simulate a dielectric slab with a ground plane, a very thin layer with a very high loss tangent is introduced behind the dielectric sheet.

The TM/TE surface wave modes predicted by the simulation are compared with the theoretical values from Pozar [2] verified the method and prediction accuracy.

REFERENCES

- [1] BARLOW,H.M and BROWN,J.: 'Radio Surface waves', Oxford, Fair Lawn, 1962, Chapter 1.

- [2] POZAR, M.D.: 'Microwave Engineering', John Wiley, 1998, pp.147 – 152.

- [3] WALTER, C.: 'Traveling Wave Antennas', McGraw-Hill, 1965, Chapter 6.

- [4] BALANIS, C.A.: ' Advanced Engineering Electromagnetics', John-Wiley, 1989 pp. 414-444.

Chapter 4

Planar 2-D Array using Dipole and Cross Dipole Conductors

4.0 Introduction

This chapter covers the investigation of dipoles and cross dipoles as the conductor elements for the 2-D planar metallodielectric structure referred to in Chapter 2. It incorporates the study of propagation and bandgap properties of surface waves present on such structures with arrays printed on them.

First, the experimental set-up is presented with the choice of antenna and the method used to study the propagation of surface waves along all direction over a large frequency range.

The predicted and measured results of propagation in all planar directions for the dipole and cross dipole arrays are also presented to validate the modelling. The objective is to achieve an absolute bandgap where propagation is prohibited in all planar directions.

Different lattice and element dimensions are also studied in order to design and control the bandgap to any desired frequency.

Finally, the test of convergence is also investigated to ensure adequate Floquet modes and basis functions are used for the predictions.

4.1 Practical Measurement

To study surface wave propagation on a dielectric slab over a wide range of frequencies, a wide bandwidth antenna which is able to excite surface waves is needed.

For this research work, the antenna chosen is a Vivaldi antenna (Figure 4.1a) which is an ultrawide bandwidth slow leaky end-fire travelling wave antenna [1,2]. It is printed on a dielectric slab made of RT-Duriod 5880 with a dielectric constant of 2.2 and has a thickness of 1.125mm.

The Vivaldi antenna on the dielectric slab is a slow wave structure, and the wave generated by it will be bound to the surface of the slab until a discontinuity or nonuniformities appear where subsequently it will be radiated.

The feeding of the Vivaldi antenna is by a smooth transition from a microstrip line to a parallel strip line and then to a symmetrically flared out slot line, which is the antenna element itself. The radiating part of the antenna is the inner edge of the antenna, which is exponentially curved out. Therefore at different frequencies, different locations of the antenna inner edge radiate. The distance between the radiating edge is constant with the wavelength of the radiating frequency (Figures 4.1b,c).

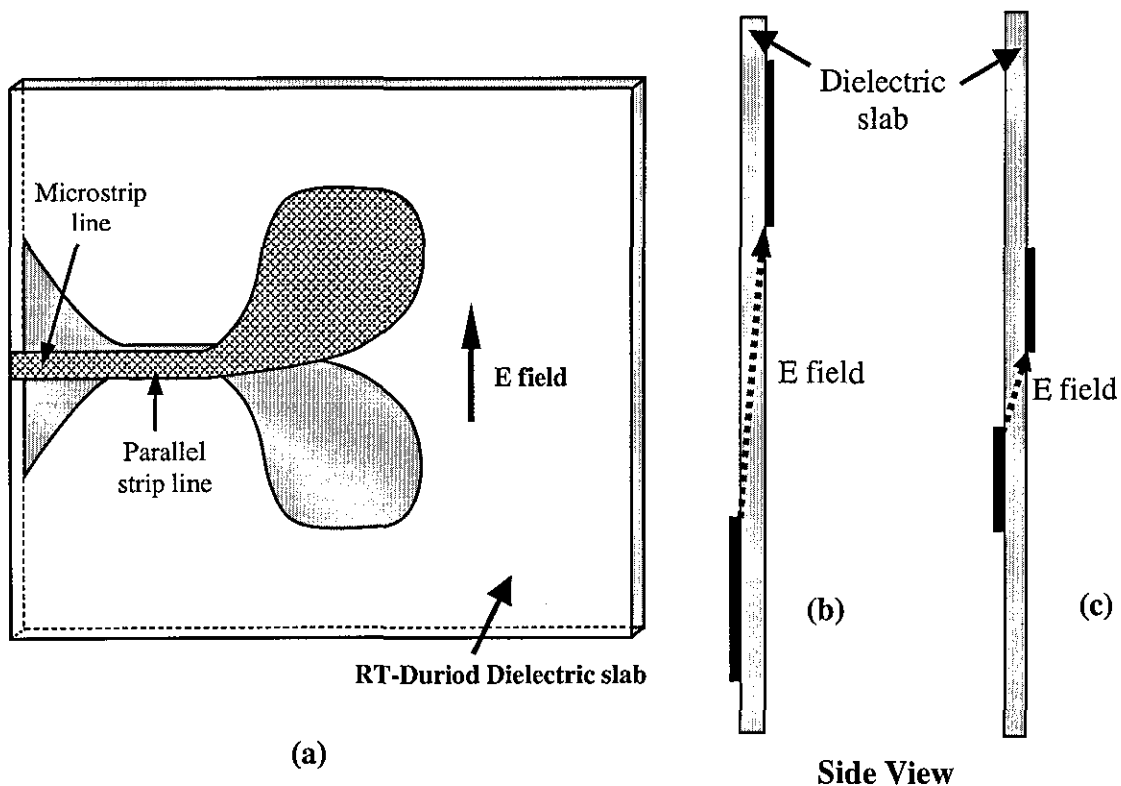


Figure 4.1: (a) Vivaldi antenna on RT-Duriod slab, thickness(s) = 1.125mm (b) Vivaldi antenna radiating at a low frequency, (c) Vivaldi antenna radiating at a higher frequency

It can be seen from Figure 4.1 that the E field component is skewed with respect to the alignment of the antenna. With a small dielectric slab thickness, at low frequencies the ratio of the radiating E field component to the thickness of the slab is large thus the skew will be small (Figure 4.1b). But at high frequency, the skew angle will increase and give high crosspolarisation. The Vivaldi antenna in this case is mainly a TE mode slow leaky end-fire travelling wave antenna but the skew angle due by the finite thickness of the slab enables it to pick up the TM mode with low efficiency.

The Vivaldi antenna was designed to operate in the range 6–20 GHz. Figure 4.2 shows the plot of the reflection coefficient (S_{11}) of the transition and the antenna. It has an insertion loss of about -15 dB from 8.3 to 20 GHz. The gain was measured to be between 6 dB and 3 dB over this frequency range.

The normalised radiation pattern measured for the E and H plane at 10 GHz is shown in Figure 4.3.

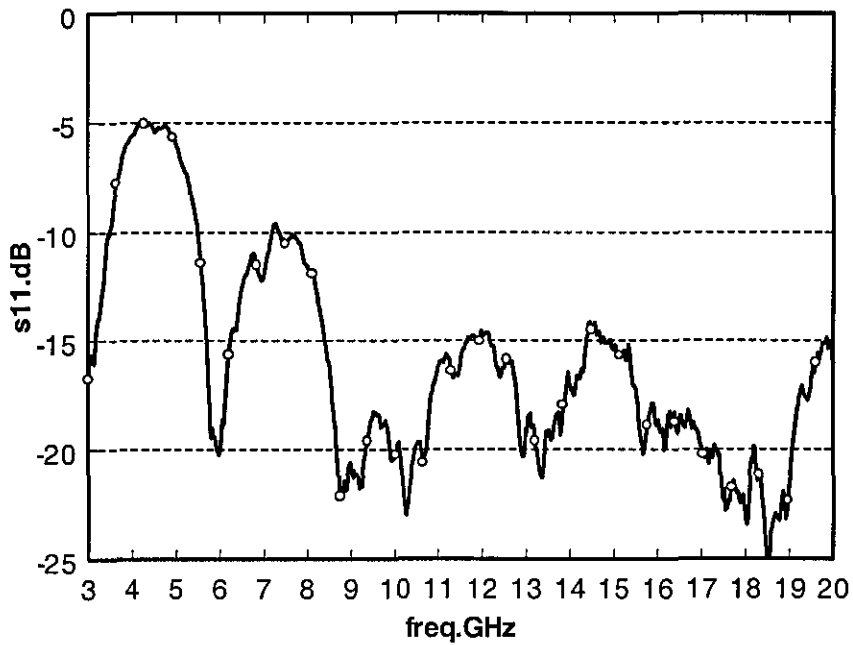


Figure 4.2: Reflection coefficient (S11) of the transition and the Vivaldi antenna.

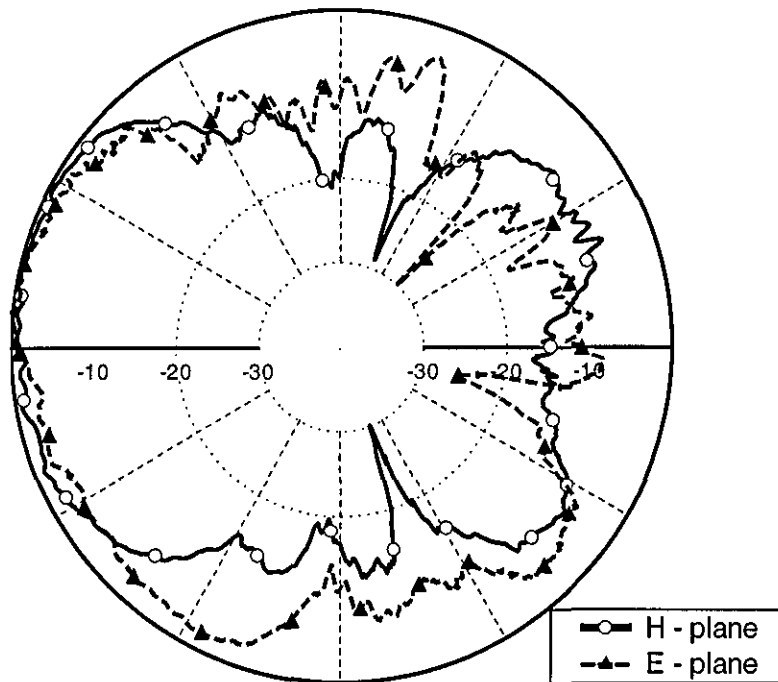


Figure 4.3: Normalised radiation pattern measured for the E and H plane at 10 GHz.

To examine surface wave propagation on a dielectric slab, two Vivaldi antennas are printed directly opposite each other on the RT-Duriod slab (Figure 4.4). The transmitting antenna will concentrate most of its field as surface waves bounded on the dielectric slab, while the receiving Vivaldi antenna printed directly at the opposite end will measure the surface waves propagated on the slab. Given that Vivaldi antenna is mainly a TE mode slow leaky end-fire travelling wave antenna, it will transmit and detect mainly TE modes only.

To investigate the surface wave propagation modes properties for the 2-D conducting element arrays, they can be printed on the dielectric slab between the two antennas. However, this technique only enables the study of the bandgap properties along one direction from the transmitting to the receiving antenna with respect to the 2-D conductor array. To study the bandgap properties in all directions along the surface, either the receiving antenna must scan in all directions by moving all around the array or the array must be rotated on the slab while fixing the receiving antenna. The first method is not feasible as it is desirable to keep the receiving antenna at a fixed distance from the transmitter. Furthermore judging from the radiation pattern, the received power is different at different angle position, even if the distance is kept the same. The latter method would be a better method as the distance and positions of the antenna are fixed.

The latter method is achieved by printing the array on a very thin dielectric sheet, which is then placed on the slab for measurement. To study the propagation in all directions with respect to the array, it is achieved simply by rotating the dielectric sheet on which the array is printed. The thin dielectric sheet used has a thickness of 0.05mm and a dielectric constant of 3. The modelling program that was written to accommodate up to five different dielectric layers can readily include this. It is also noticed that the dielectric sheet has very little effect on the bandgap properties of the slab as it has a dielectric constant close to the RT-Duriod used, and its thickness is small compared to the thickness of the slab. This is also a cost effective method as it not only enables the study of different propagation directions by rotating the array on the dielectric sheet, but it can also provide measurements for different arrays just by printing them on different dielectric sheets.

Finally, the measurements presented in this Chapter are calibrated with the inclusive of the cable and the two Vivaldi antennas printed on the RT-Duriod slab. Using the HP8757A Network Analyser, the dynamic range is about $\pm 60\text{dB}$. The supply power is 5dbm ; taking into the account of the cable loss and the two Vivaldi antennas performance over this range of frequency, the measured s_{21} is about -25 dB . This limits the negative dynamic range for the measurement to around -30 dB .

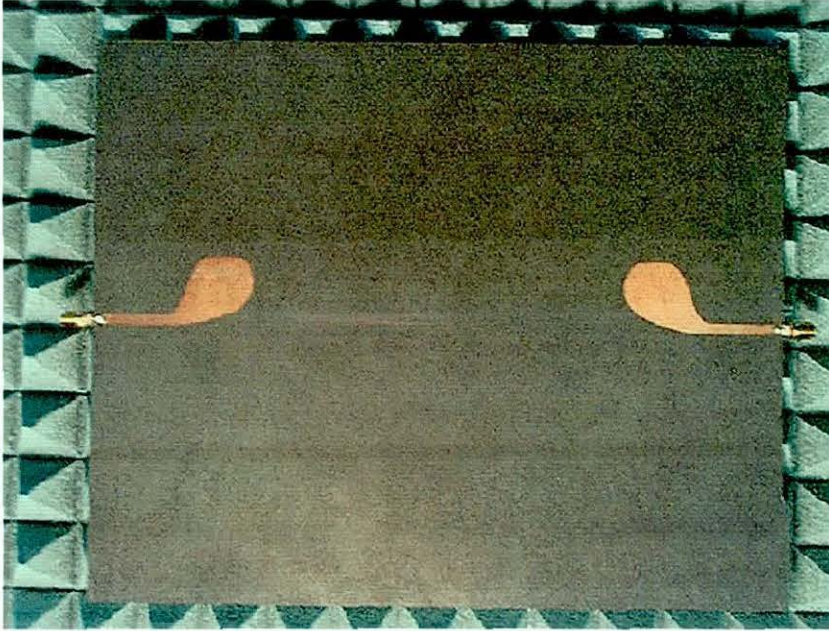


Figure 4.4a : Top side of a Vivaldi antenna

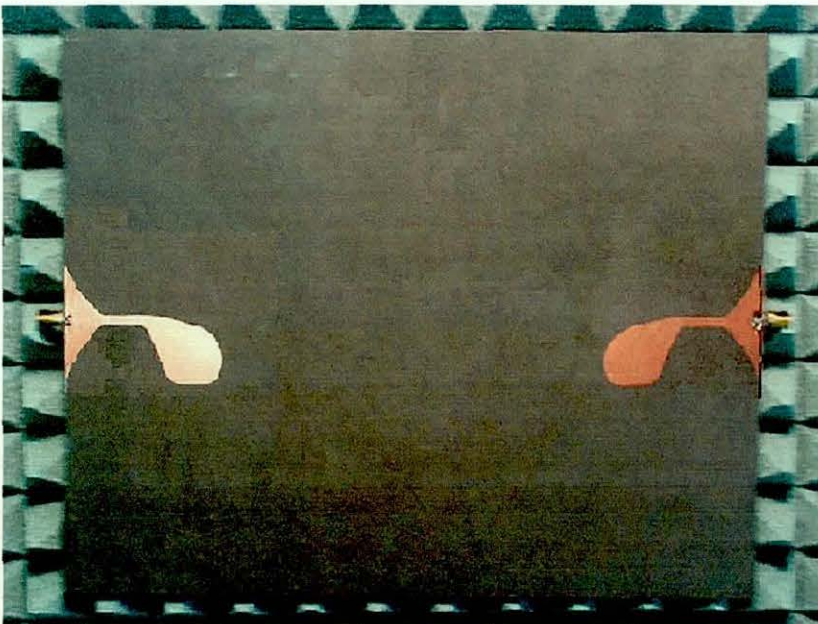


Figure 4.4b : Bottom side of a Vivaldi antenna

4.2 Planar 2-D array using Dipole and Cross Dipole conductor

The first choice for the initial modeling is be the dipole conductor array. This is due to its simple geometry and relatively straightforward computational demands.

From Section 2.5, the characteristic determinants of $[Z]$ are needed to determine propagation constants for all possible propagation modes that exist along the two dimension plane of the array. For the calculation of Z_{in} Eq.(2.37) to form the matrix $[Z_{MN}]$, assuming the width of the dipole element is small compared to the length and does not contribute to the computing of the basis functions. Thus the current induced in the dipole elements will be along its length. The bases functions are sinusoidal and in an arbitrary direction \hat{v} [3].

$$h_n^c = \frac{1}{\sqrt{NR}} \cos \frac{n\pi v}{L} \quad (4.1a)$$

$$h_n^s = \frac{1}{\sqrt{NR}} \sin \frac{n\pi v}{L} \quad (4.1b)$$

Where n is the number of the basis function

$$NR = \frac{WL}{2} \text{ is the normalisation factor due to the orthogonality of these bases}$$

For example, assuming five basis functions across the conductors ($n = 5$), which would consist of cosine terms $n = 1, 3, 5$ and sine terms $n = 2, 4$. In Figure 4.5, the conductor is aligned along the y -axis ($\hat{y} = \hat{v}$).

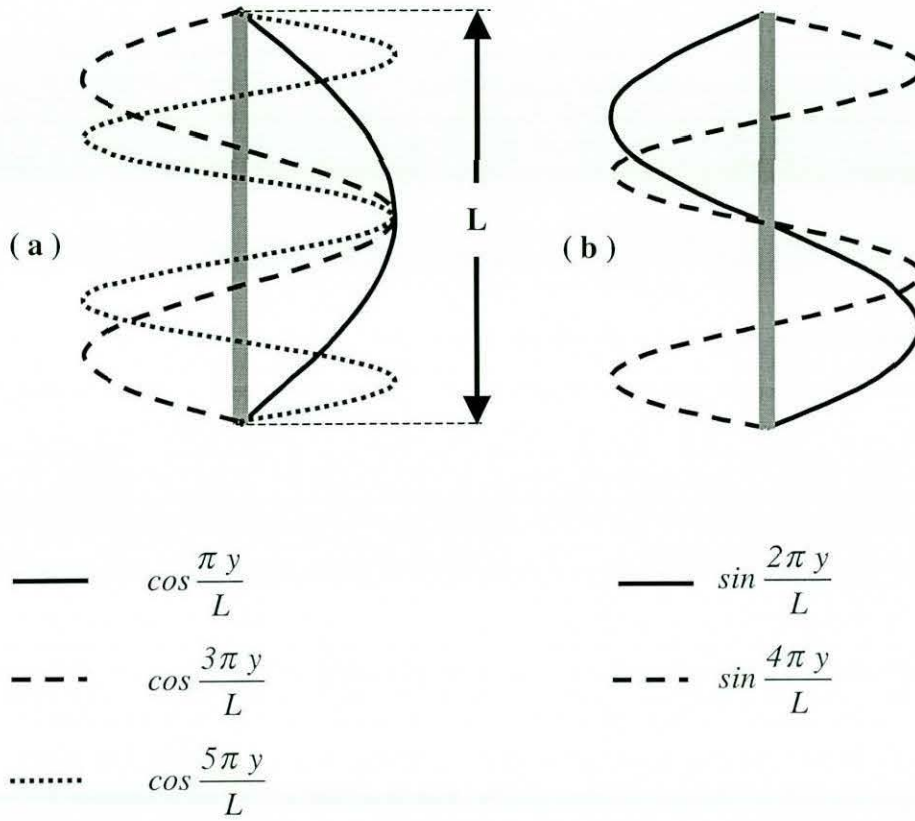


Figure 4.5 : Dipole with 5 bases functions along the y-axis, (a) cosine terms (b) sine terms

Assuming the width of the dipole to be small, thus the contribution to the basis functions will come from the length of the dipole (which is position along the y axis). The Floquet transform of Eq.(4.1a) and Eq.(4.1b) are

$$\tilde{\underline{h}}_n^c = \tilde{h}_{ny}^c \hat{y} \quad (4.2a)$$

$$\tilde{\underline{h}}_n^s = \tilde{h}_{ny}^s \hat{y} \quad (4.2b)$$

And

$$\tilde{h}_{ny}^c = \tilde{m}_x (\tilde{p}_{ny} + \tilde{q}_{ny}) \quad (4.3a)$$

$$\tilde{h}_{ny}^s = j \tilde{m}_x (-\tilde{p}_{ny} + \tilde{q}_{ny}) \quad (4.3b)$$

Where

$$\tilde{p}_{ny} = \frac{\sin \left[\left(\frac{n\pi}{L} + k_y \right) \frac{L}{2} \right]}{\left(\frac{n\pi}{L} + k_y \right) \frac{L}{2}} \quad \tilde{q}_{ny} = \frac{\sin \left[\left(\frac{n\pi}{L} - k_y \right) \frac{L}{2} \right]}{\left(\frac{n\pi}{L} - k_y \right) \frac{L}{2}}$$

And

$$\tilde{m}_x = \sqrt{NR} \frac{\sin \left(k_x \frac{W}{2} \right)}{k_x \frac{W}{2}}$$

For the cross dipole, 8 basis functions are applied, 4 basis functions will represent the vertical conductor element as in dipole element case (Figure 4.5) and another 4 basis functions will represent the horizontal element (Figure 4.6). The Floquet transform of the basis functions for the horizontal element can be readily obtained from Eq.(4.2) and Eq.(4.3) with changes made for the contribution comes from the x -axis.

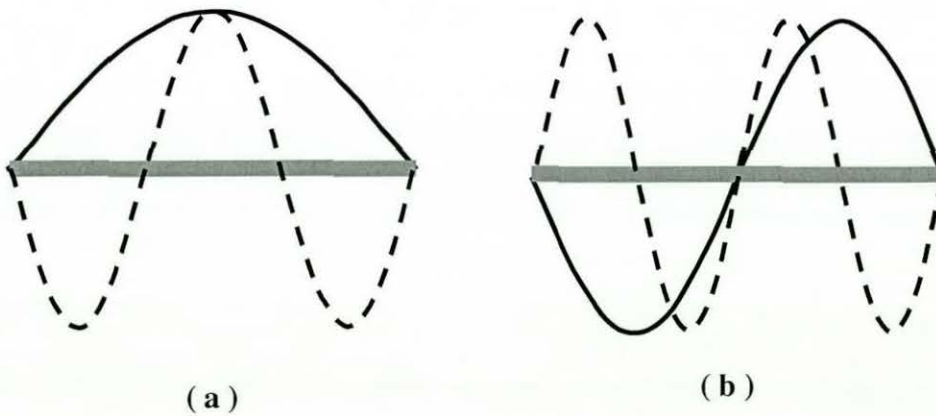


Figure 4.6 : Cross dipole with another 4 bases functions representing the horizontal element,
(a) cosine terms (b) sine terms

4.3 Dipole array results and discussion

The process of prediction is to scan the phase constants (β) for each frequency and obtain the respective characteristic determinant of the matrix $[Z]$ in Eq.(2.37). The whole range of the characteristic determinant for each frequency is plotted out. From the plot, all minimas are recorded (see Section 2.5) and this is repeated for the whole range of frequencies. Finally, the corresponding phase constants (β) for all the true minimas are plotted out against frequency to determine the location of the bandgap.

The process of determining the minima of the characteristic determinant Eq.(2.37) while scanning the irreducible Brillouin zone is a tedious and time consuming task. The condition for selection is that the minima should be of a sharp and deep nature. But sometimes the minima might not be obvious. A few selection criteria have to be taken into consideration to determine a true set of minima that represent a propagation mode. First, the minima should be obvious and of a sharp and deep nature. Second, the set of true minimas will shift as the frequency increases. Third, the set of true minimas will continue when the Brillouin zone scan change directions. Fourth, when the Brillouin zone scan ends in a closed loop, the set of minima must meet at the same frequency that the scan began.

Finally, caution has to be taken to discard the minimas that correspond to the TEM mode (Transverse Electromagnetic) which does not exist that will also appear as a true set of minima in the simulation result.

The step size used for the frequency and phase constants (β) have to be tested to ensure that all the propagating modes are recorded. This is a case of accuracy at the expense of computational time and resources. The usual step size used is 0.2 GHz and 0.00167 rad/m but in cases of ambiguity that arise, finer step sizes are taken to extract the solution.

The dipole arrays are modeled with different lattice and element dimension. The array discussed in this section has a lattice of periodicity $D = 10\text{mm}$ and 8mm , the dipole length $L = 7.5\text{ mm}$ and 6 mm and width $W = 0.6\text{mm}$.

4.3.1 Dipole Dimension ($D = 10\text{mm}$, $L = 7.5\text{mm}$)

The square lattice has its element spaced out periodically on two axes separated by angle $\alpha = 90^\circ$. The two arrays modeled have a dielectric constant of 2.2 and thickness(s) 1.125mm. Due to the symmetric and periodic properties of the first Brillouin zone and the dipole element (Section 2.6.1), the shaded region is determined as the irreducible Brillouin zone (Figure 4.7b). Propagation in this region is the same as the other 3 quadrants and this has been verified from the modeling. The maximum phase constant (β_x and β_y) in the direction of x and y -axis within the irreducible Brillouin zone is $\frac{\pi}{a}$.

For the graph in Figure 4.7, the horizontal axis represent the phase constant of the propagation mode in various directions, and the vertical axes are the normalised frequency and frequency respectively.

For the dipole array in Figure 4.7, with $\epsilon_r = 2.2$, thickness $s = 1.125\text{mm}$, the first mode which is the surface wave starts at zero frequency. In the direction ($\Gamma - X$) where the plane of propagation is parallel to the dipole; the surface wave has ceased at 11.6 GHz. (reached a stop band). This is the beginning of the bandgap along the x -direction, which starts at 11.6 GHz and ends at 30.5 GHz. As the propagation direction moves from x towards the y -axis, the stopband narrows until it meets at 14.7 GHz and in the y -direction, it ceased to have a stopband. Thus from the modelling, it showed that there is no absolute bandgap for this dipole array.

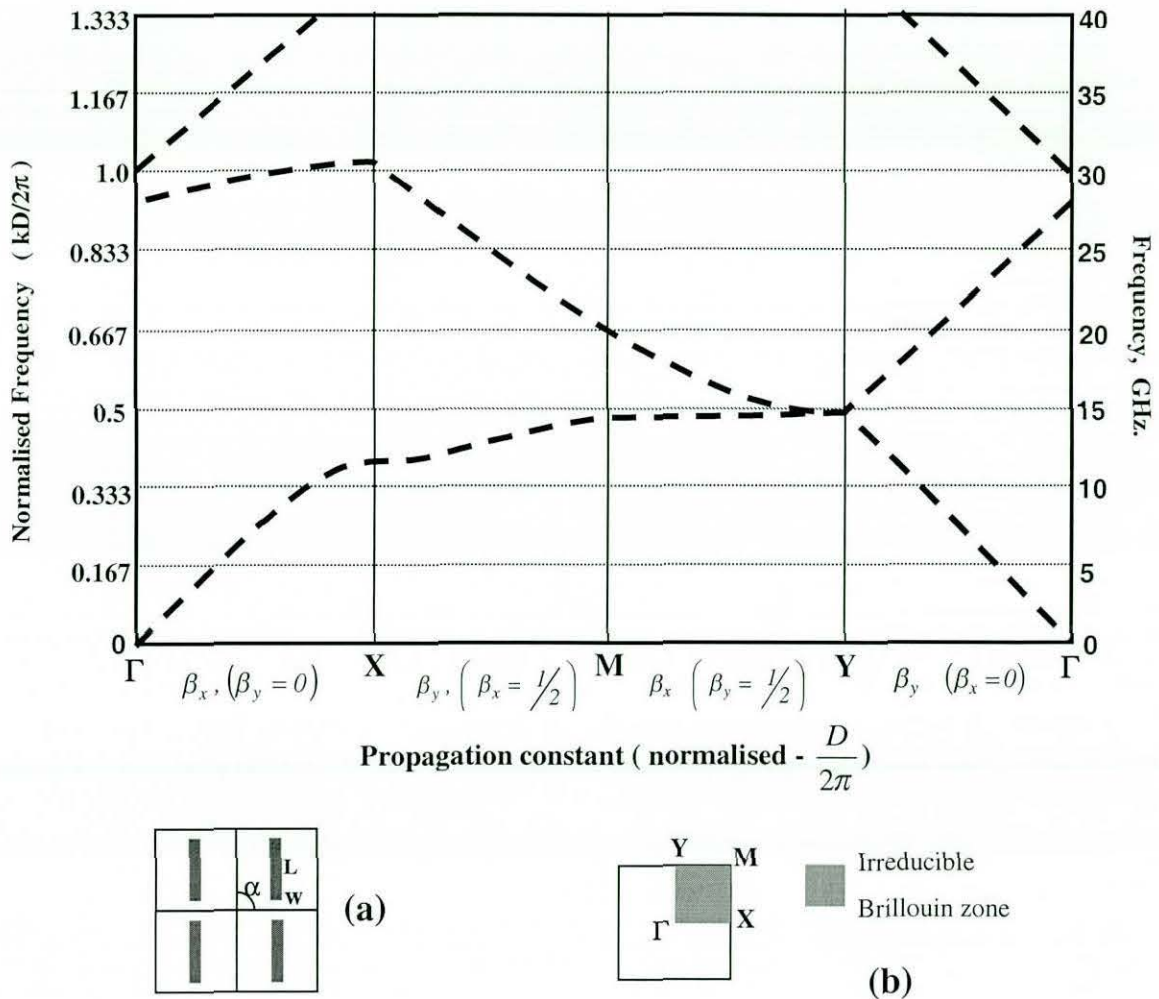


Figure 4.7 : Band structure for the first few TE modes of the vertical dipole array, (a) direct lattice, (b) reciprocal lattice and its first Brillouin zone $L = 7.5\text{mm}$, $W = 0.6\text{mm}$, $D = 10\text{mm}$, $\epsilon_r = 2.2$, Thickness $s = 1.125\text{mm}$, $\alpha = 90^\circ$.

Figure 4.8 shows the s_{21} measurements carried out with the Vivaldi transmitting and receiving antennas in three different directions with respect to the dipole element array. Assuming that the band gap is determined at a level of -6 dB of the s_{21} measurement. At 0° which is propagation in the x -axis, the beginning of the bandgap is measured to be 11.7 GHz. As the propagation direction changes to 75° the bandgap closes up to around 1 GHz, from $14.5 - 15.5$ GHz. Finally, at 90° (which is the y -direction) there is full propagation.

Figure 4.9 shows the photo of the dipole array with the transmitting and measuring Vivaldi antennas. It is observed that there is a gain of 5 dB before the stopband in the x -direction, this is because the dipole array behaves as guiding slow wave elements for the transmitting Vivaldi antenna. In the passband frequencies, it concentrates the fields on the dielectric slab in the direction of the receiving antenna. Naturally, in the y -direction, where the dipole is aligned along the propagation direction, this gain diminishes. A more detailed explanation of the gain is included in Section 5.3.

From the measurement results, it agrees well with the modelling prediction that there is no bandgap in the y -direction. The predicted bandgap of this array for all the planar directions from the modelling also coincide well with the measurements.

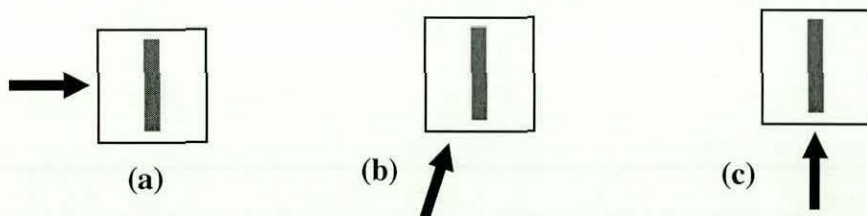
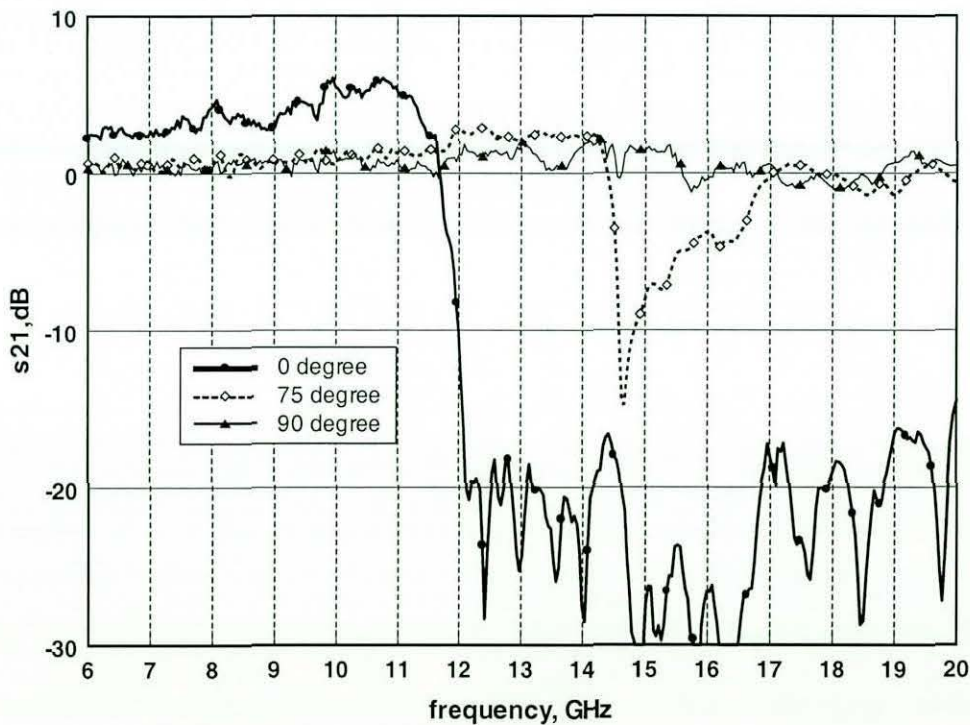


Figure 4.8 : Measurement results of the dipole array from Figure 4.7

(a) 0° (x -direction), (b) 75° , (c) 90° (y -direction)

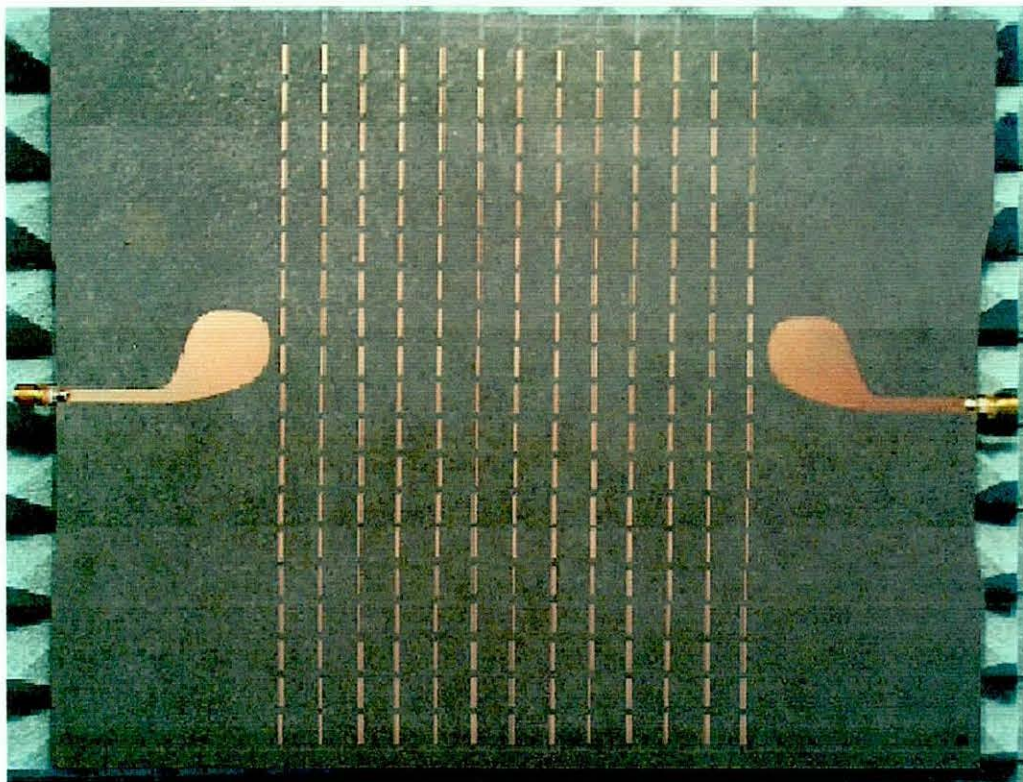


Figure 4.9 : Photo of a dipole array with the transmitting and measuring Vivaldi antennas

4.3.2 Dipole Dimension ($D = 8\text{mm}$, $L = 6\text{mm}$)

The second dipole array (Figure 4.10) has a square lattice of 8mm and dipole length of 6mm with the same dielectric constant and thickness as in Section 4.3.1. The bandgap starts at 14.2 GHz in the x -direction for this array. Likewise the bandgap narrows as the propagation direction changes towards the y -axis. Finally, when the propagation direction is along the length of the dipole, there is full propagation. The reason that the dipole does not have an absolute bandgap is because the width of the dipole is small, thus the contribution will come from the length of the dipole. With respect to the length of the dipole along the y -axis, the propagation in the x -axis will evidently achieve the largest bandgap.

It is observed that as the lattice and dipole dimensions reduces, the bandgap frequency shifts up. The beginning of the stop band for the x -direction shifts up from 11.6 GHz to 14.2 GHz between these two dipole arrays. In the y -direction, the bandgap narrows and end at 14.7 GHz and 17.9 GHz for the two dipole arrays. From these examples, different arrays can be designed to control the desired frequency stopband for a dielectric slab.

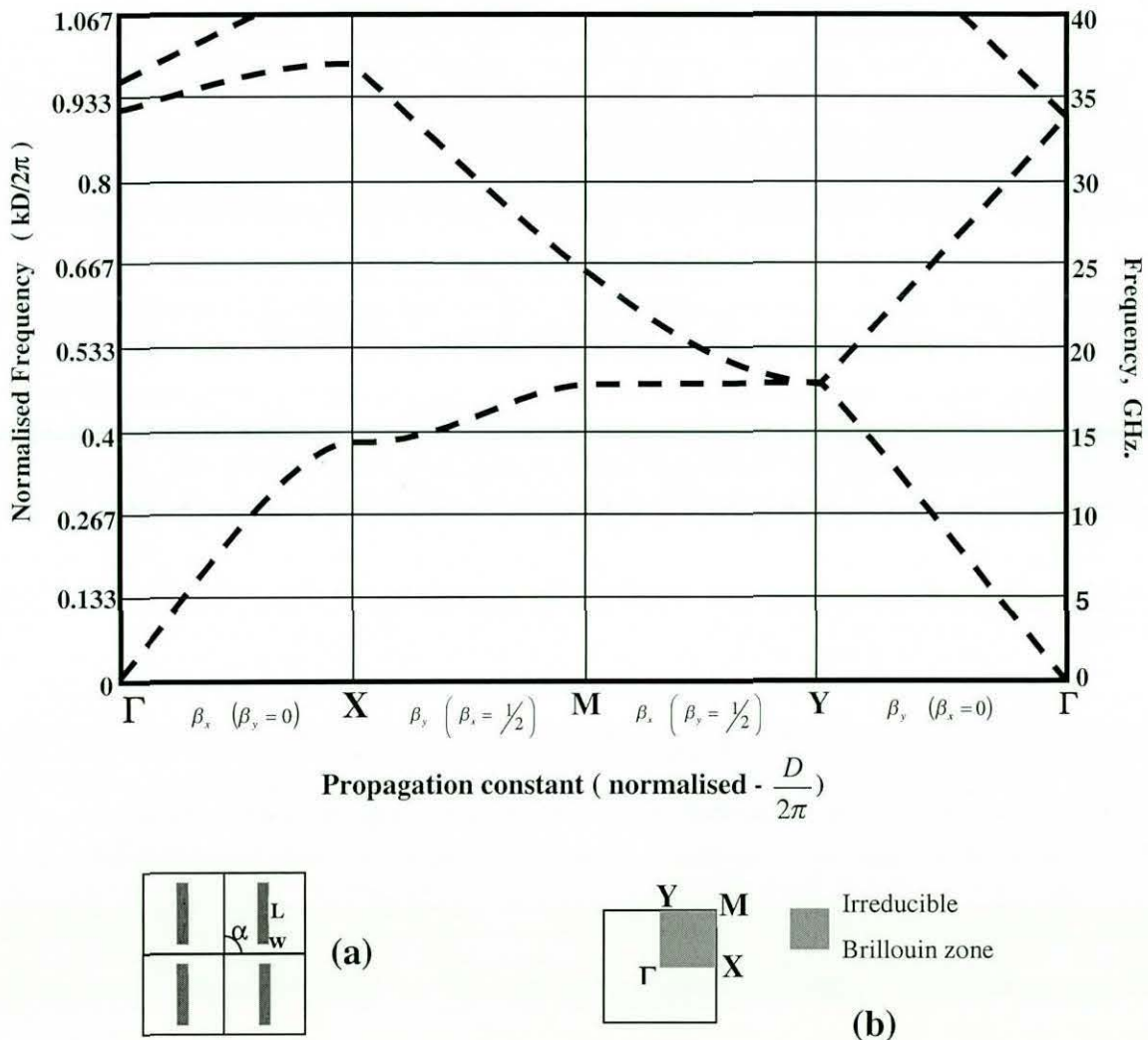


Figure 4.10 : Band structure for the first few modes of the vertical dipole array, (a) direct lattice, (b) reciprocal lattice and its first Brillouin zone $L = 6\text{mm}$, $W = 0.6\text{mm}$, $D = 8\text{mm}$, $\epsilon_r = 2$, Thickness $T = 1.125\text{mm}$, $\alpha = 90^\circ$.

The measurements for this dipole array are also presented in three directions with respect to the dipole element (Figure 4.11). At 0° where propagation is in the x -direction, the beginning of the bandgap is measured to be at 14.3 GHz. At 75° where the band gap narrows to 17.75 GHz and ends at 19.1 GHz before full propagation at 90° (y-direction). The measurements agree well with the modeling of the bandgap frequency for this array in all the planar directions on the plane.

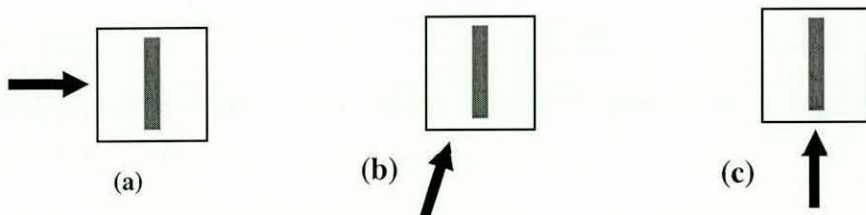
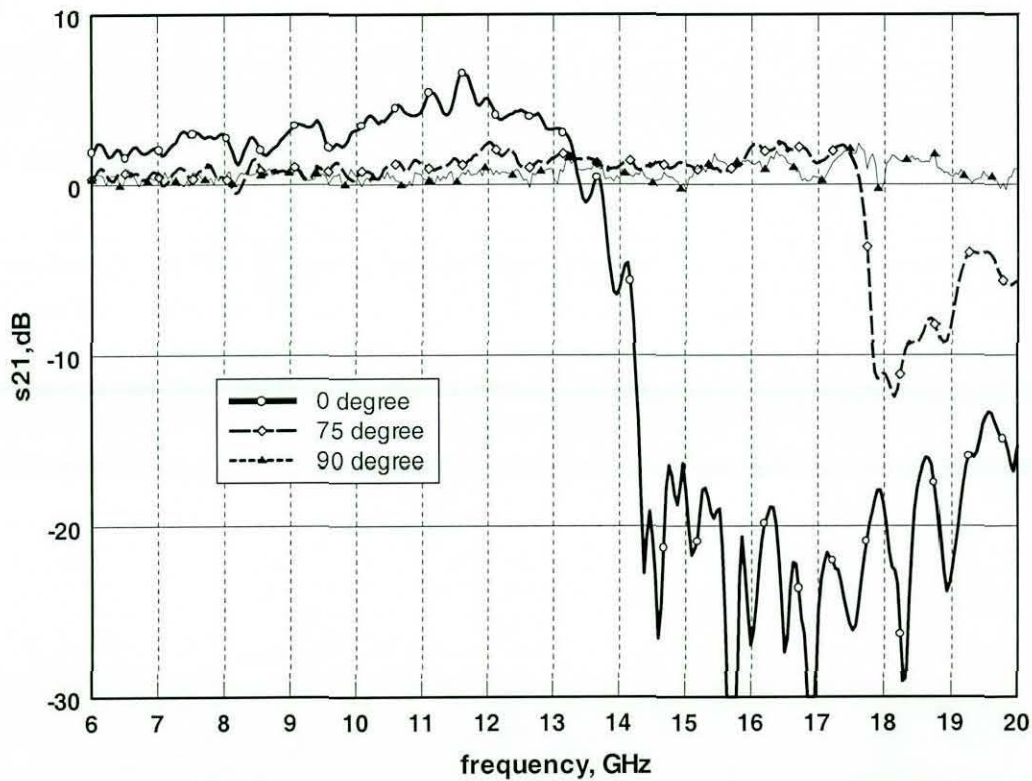


Figure 4.11 : Measurement results of the dipole array from Figure 4.10

(a) 0° (x -direction), (b) 75° , (c) 90° (y -direction)

4.4 Cross Dipole Array Results and Discussion

The next obvious choice for a square lattice would be the cross dipole array to achieve an absolute bandgap. The reason is that the horizontal arm of the cross dipole will account for the propagation in the y -direction.

The cross dipole is also the natural choice for a square lattice as the symmetry properties of the cross dipole and the first Brillouin zone of the square lattice is 45° . As the propagation direction changes from x -axis to the xy -axis then to the y -axis, the beginning of the bandgap will shift from $(\Gamma - X)$ to $(\Gamma - M)$ and back to $(\Gamma - X)$ again (Figure 4.12). Hence it would only be necessary to explore only 45° of the first Brillouin zone to determine the propagation in all directions along the plane of the array.

The cross dipole array presented in Figure 4.12 has an array periodicity of 10mm and the cross dipole length is 8mm with the same dielectric constant ($\epsilon_r = 2.2$) and thickness ($s = 1.125\text{mm}$). From the modelling, the TE mode bandgap starts at 11.1 GHz in the x -direction for this array. The bandgap narrows as the propagation direction changes towards the xy -axis (45°) where it achieved a TE absolute bandgap of 7 GHz from 14 GHz to 21 GHz.

The graph also includes the TM modes, the predicted TM mode bandgap starts at 14 GHz in the xy -direction and it shifts up to 14.5 GHz in the x -direction. The TM absolute bandgap for this array is 3.1 GHz from 14.5 GHz to 17.6 GHz. It is observed that the TE and TM bandgap overlap each other and thus achieve a common absolute bandgap from 14.5 GHz to 17.6 GHz, refer by the gray block in Figure 4.12.

In Figure 4.12, the long dash line represents the TM_0 mode above the TEM line (small dash line) of the medium. The TM_0 mode here is in the fast wave region and it is internally reflected within the substrate [6].

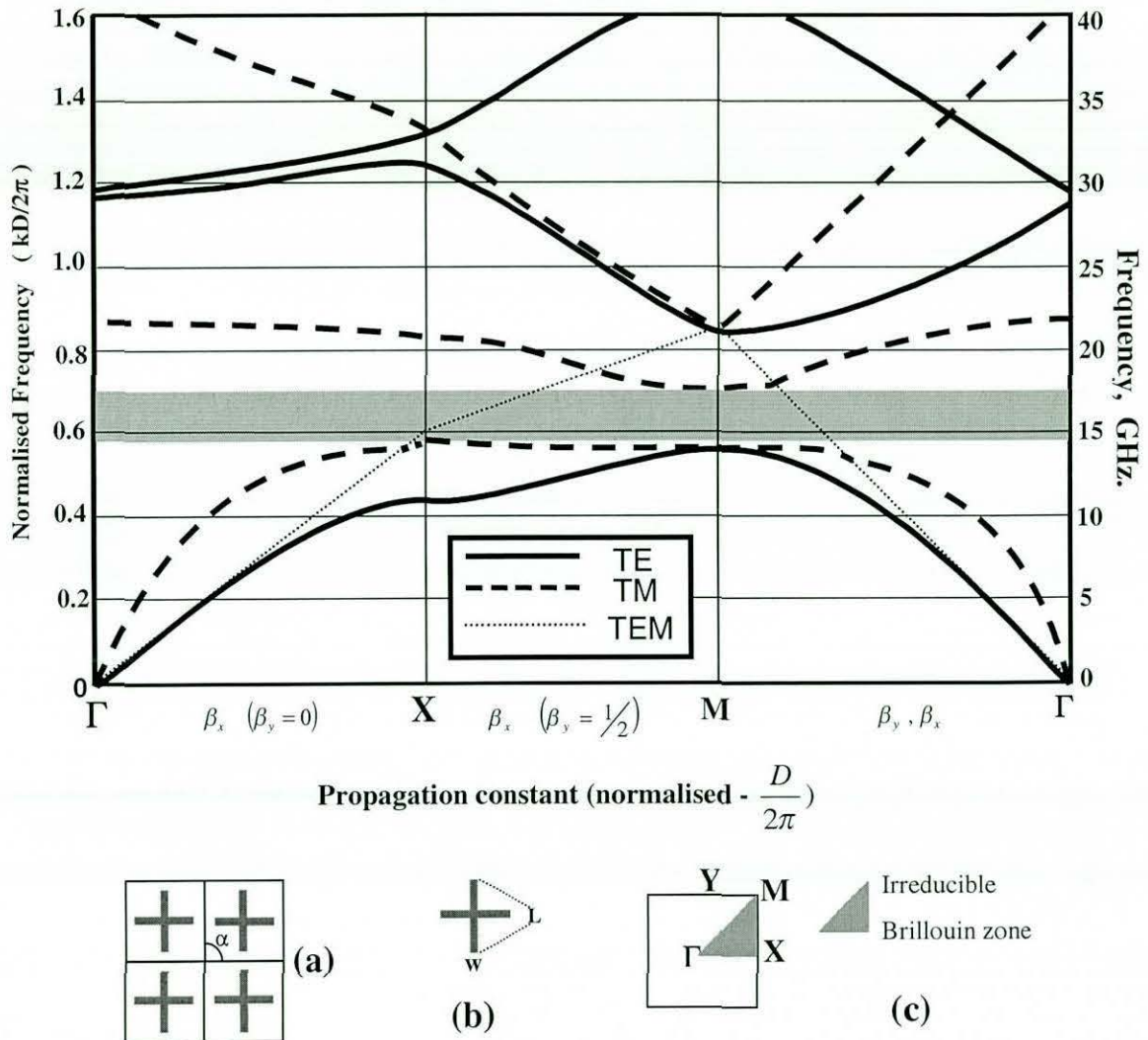


Figure 4.12 : Band structure for the first few TE modes (lines) and TM modes (dash) of the cross dipole array in a square lattice. (a) Direct lattice, (b) cross dipole dimensions (c) The first Brillouin zone of its reciprocal lattice and its irreducible Brillouin zone, $L = 8$ m, $W = 0.6$ mm, $D = 10$ mm, $\epsilon_r = 2.2$, Thickness $s = 1.125$ mm, $\alpha = 90^\circ$.

The measurement results are shown in Figure 4.13. The stopband in the x -direction starts at 11.25 GHz and it extends up to the measurement limit of 20 GHz. The beginning of stopband frequency increases as the propagation direction moves towards the xy -direction. It is noted that as the propagation direction moves from the xy -direction to the y -direction, the start of the bandgap moves back to 11.25 GHz, which is the same as that in the x -direction.

From the measurement results in the xy -direction, the start of the bandgap begins at around 14.2 GHz. It is observed that there is some sort of propagation starting from 18 GHz to 20 GHz. in the xy -direction but the received power is low, from the prediction in Figure 4.12, this would be the TM_1 mode. The Vivaldi antenna used is not a perfect TE mode antenna, the slew angle caused by the finite thickness of the slab enables it to pick up this TM_1 mode with a low efficiency.

Once again the measurements agree well with the modeling prediction regarding the location of the stopband. The common absolute bandgap of both the TE/TM modes is also observed to exist at around 14.5 GHz to 18 GHz. From the results, the maximum gain in the passband is about 6 dB in the x -direction and 9.8 dB in the xy -direction.

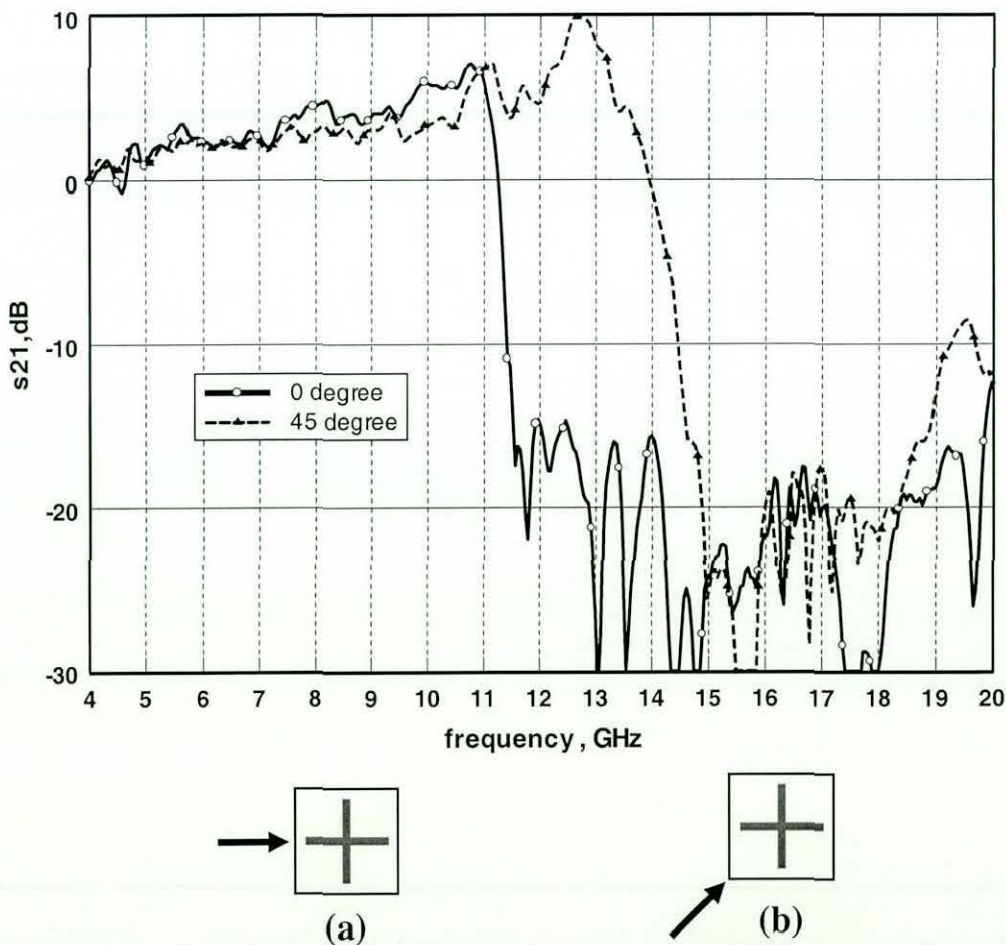


Figure 4.13 : Measurement results of the cross dipole array from Figure 4.12,

(a) 0° (x -direction), (b) 45° (xy -direction)

4.5 Testing for convergence

Since only a finite number of basis functions, N , are used (Section 2.5), it is important to test for convergence of the solution. The purpose is to choose an appropriate number of basis functions N to represent the problem [3]. Also, a sufficient number of Floquet modes (p, q) are needed to included at least the main lobe of the spectrum. The ratio $\Delta = PQ/N$ can be used as a figure of merit and it is recommended to keep the ratio fixed once convergence is achieved.

The first convergence test is carried out by fixing the bases functions at $N = 5$ and varying the number of Floquet modes until there is little different in the results. In Figure 4.14, the horizontal axis refers to the number of Floquet modes used and on the vertical axis, it represents the beginning and end frequencies of its corresponding bandgap for the TE mode. From the results for modeling a dipole, it can be observed that the bandgap converges to a fixed range when the number of Floquet modes increase above 13. The ratio $\Delta \approx 34$ for 13 Floquet modes and 5 bases functions. As for a cross dipole, it was found to have 4 basis functions is sufficient for each arm ($\Delta \approx 21$).

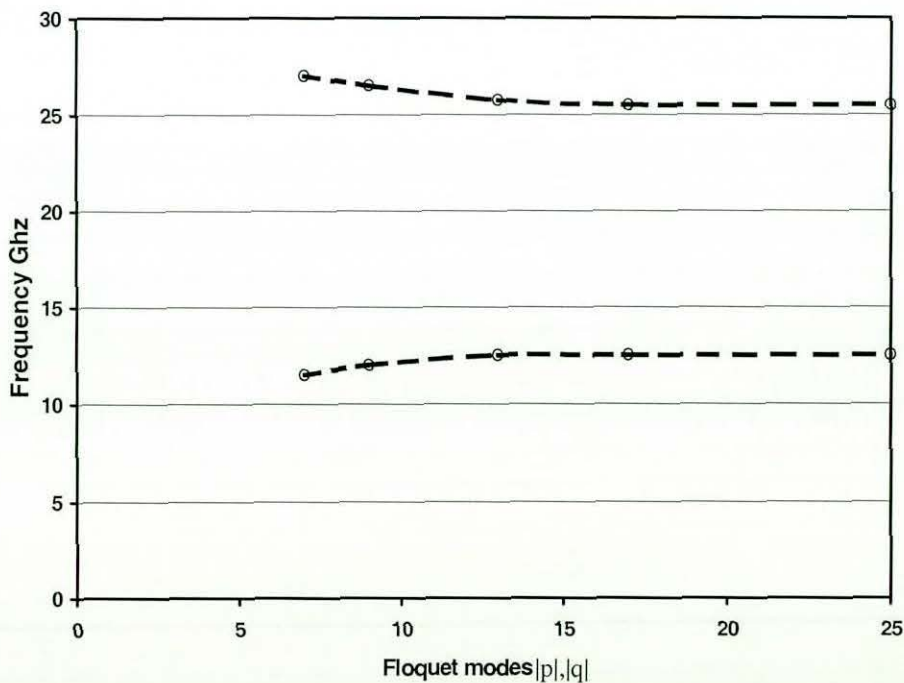


Figure 4.14 : TE bandgap of a dipole array with different number of Floquet modes for $N = 5$.

The second convergence test carried out was to vary the number of basis functions with the number of Floquet modes fixed. Floquet modes of 13 and 25 were used and as the number of basis functions increased, the ratio Δ will decrease with 13 Floquet modes, the results (Figure 4.15) deteriorated when the number of basis functions used increased above 10

($\Delta = 17$). Whereas, using 25 Floquet modes, the result remains constant but it is very computationally taxing. Also it is noted from Figure 4.7 that 5 basis functions would be sufficient to approximate the solution for a dipole array.

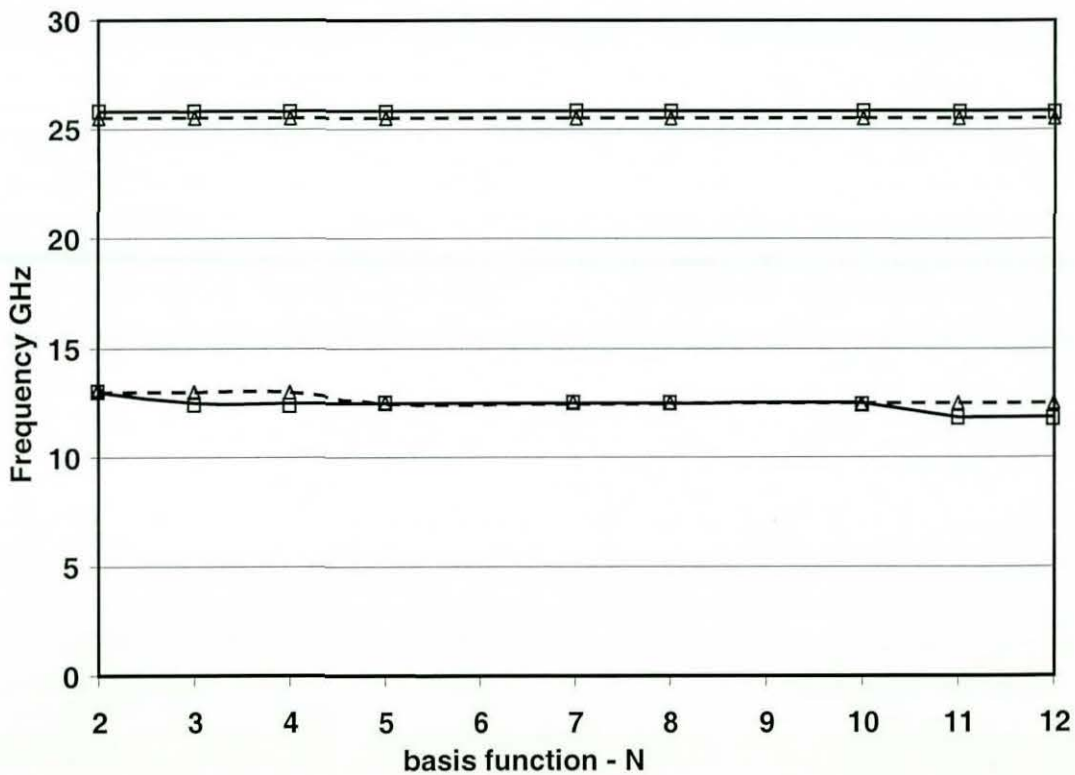


Figure 4.15 : TE bandgap with different number of bases functions; 13 Floquet modes (line),
25 Floquet modes (dash)

4.6 Conclusions

For the predicted and measured results shown, by varying the element dimension and lattice periodicity, the bandgap frequency can readily be changed. This means that there is a possibility of designing and controlling the bandgap frequency [4]. In Section 5.3, an investigation is carried out to study the effects of the element dimension have on the bandgap.

In Section 4.2, the dipole array does not exhibit an absolute bandgap [5]. The dipole element, that is a polarised element, produces the largest bandgap when the direction of the incident field is perpendicular to its length. Thus the dipole is not suitable for achieving an absolute bandgap for 2-D planar propagation. However, it is suitable to be used as a 1-D 'photonic crystal' where the propagation incidence is only restricted to one direction that is perpendicular to the length of the dipole [6]. With the shape of a dipole element, it can be packed closely together thus increasing the packing density. For applications where there is a limited space available, the dipole array might be a good choice to achieve the bandgap properties needed.

In Section 4.3, the cross dipole array does exhibit an absolute bandgap for all planar propagation directions [5]. It can be chosen as a 2-D planar 'photonic crystal'. However, the beginning of the bandgap varies over a large frequency range as the propagation direction changes. The next research effort will be looking into 'stabilising' the bandgap so that the beginning of the bandgap does not vary with the direction of propagation.

Finally, the test of convergence was carried out to ensure enough Floquet modes and basis functions are used for the modelling. From the modelling, the predicted bandgap of the arrays agree well with the measurements in all planar directions.

REFERENCES

- [1] GAZIT, E.: 'Improved Design of the Vivaldi Antenna', IEE Proc. H, Vol. 135, No 2, April 1988, pp 89-92.
- [2] LANGLEY J.D.S., HALL P.S., NEWHAM P.: 'Novel Ultrawide-bandwidth Vivaldi Antenna with Low Crosspolarisation', Electronics Letters, Vol. 29, No. 23, Nov 1993, pp 2004-2005.
- [3] VARDAXOGLU J.C.: 'Frequency Selective Surfaces: Analysis and Design', Research Studies Press, 1997, Chapter 2.
- [4] VARDAXOGLU J.C., LOCKYER D.S., KEARNEY M.J., LEE Y.L.R.: 'Photonicallly Induced Antenna Arrays and Their Bandgap Properties', International Conference on Electromagnetices in Advanced Applications 1999, Torino, Italy, pp 485-488.
- [5] VARDAXOGLU J.C. and LEE Y.L.R.: 'Dipole and Cross Dipole Array as 2-D Planer Photonic Crystal', preparing for publication.
- [6] JOANNOPOULOS J.D., MEADE R.D., WINN J.N.: 'Photonic Crystals – Molding the Flow of Light', Princeton University Press, 1995, Chapter 4.

Chapter 5

Planar 2-D Array using Tripole Conductors and Applications

5.0 Introduction

Tripole arrays were initially designed on hexagonal lattice for curved FSS. They have revealed good reflection bandwidth and band spacing [1,2].

One disadvantage of using dipole element is that it is a singly polarised element hence it does not produce the desired absolute bandgap. Although a cross dipole array does have an absolute bandgap but the large variation of the TE bandgap starting frequency with respect to the different propagation directions might make the cross dipole array undesirable for certain applications. It is suggested that a tripole element would be a more desirable element as it is not polarised only in one direction and it also possess the same symmetric properties as the brillouin zone of a triangle lattice (Section 2.6.1).

This chapter covers the investigation of a tripole as the conductor element for 2-D planar metallodielectric structure. It incorporates both the prediction and measurement of bandpass and bandgap properties of the surface waves presence on such structures.

Radiation patterns with regard to the Vivaldi antenna with and without the array are also measured to study the bandgap properties in the E- and H-planes.

A more thorough study is presented for controlling the bandgap with different element dimensions and dielectric constant.

Finally, the chapter covers some novel applications that were investigated for these structures.

5.1 Planar 2-D array using Tripole conductor

The tripole consists of three dipoles arranged at 120° angularly with respect to each other and connected together at the centre of the unit cell. Its is sufficient to use only one basis function for each arm of the tripole for the modal analysis. The method used is to calculate the basis function of one arm that is aligned at an arbitrary angle φ with respect to the y-axis. By changing the angle φ to the angular position of each arm, all the three basis functions of the tripole can be obtained.

Like modeling the dipole element, the width of the arms of the tripole is assumed to be small and current only flows along the arm of the tripole. The basis functions [3] are

$$h_n^c = \frac{1}{\sqrt{NR}} \cos \frac{n\pi v}{2L} \quad (5.1a)$$

$$h_n^s = \frac{1}{\sqrt{NR}} \sin \frac{n\pi v}{2L} \quad (5.1b)$$

Where n is the number of the basis function

$$NR = \frac{WL}{2} \text{ is the normalisation factor due to the orthogonality of these bases}$$

The Floquet transform of Eq.(5.1a) and Eq.(5.1b) set of bases functions in an arbitrary direction.

$$\underline{\tilde{h}}_n^c = \tilde{h}_{nv}^c (\cos \varphi \hat{y} - \sin \varphi \hat{x}) \quad (5.2a)$$

$$\underline{\tilde{h}}_n^s = \tilde{h}_{nv}^s (\cos \varphi \hat{y} - \sin \varphi \hat{x}) \quad (5.2b)$$

And

$$\tilde{h}_{nv}^c = \tilde{m}_u (\tilde{p}_{nv} + \tilde{q}_{nv}) \hat{v} \quad (5.3a)$$

$$\tilde{h}_{nv}^s = j \tilde{m}_u (-\tilde{p}_{nv} + \tilde{q}_{nv}) \hat{v} \quad (5.3b)$$

Where

$$\tilde{p}_{ny} = \frac{1 - e^{j(\frac{n\pi}{2L} + k_v)L}}{\frac{n\pi}{2L} + k_v} \quad \tilde{q}_{ny} = \frac{1 - e^{-j(\frac{n\pi}{2L} - k_v)L}}{\frac{n\pi}{2L} - k_v} \quad (5.4)$$

$$\tilde{m}_u = \frac{\sqrt{NR} \sin\left(k_u \frac{W}{2}\right)}{2 k_u \frac{W}{2}}$$

and

$$\begin{pmatrix} k_u \\ k_v \end{pmatrix} = \begin{pmatrix} \cos \varphi & \sin \varphi \\ -\sin \varphi & \cos \varphi \end{pmatrix} \begin{pmatrix} k_{tx} \\ k_{ty} \end{pmatrix} \quad (5.5)$$

5.2 Tripole Array Simulation Results and Discussion

The method of obtaining the results and selection is described in section 4.3. The tripoles are modeled with the similar parameters as the dipole array but in a triangular lattice with $\alpha = 60^\circ$ [4].

Figure 5.1 shows a photo of a tripole array printed on RT-Duriod 5880 with the transmitting and receiving Vivaldi antennas.

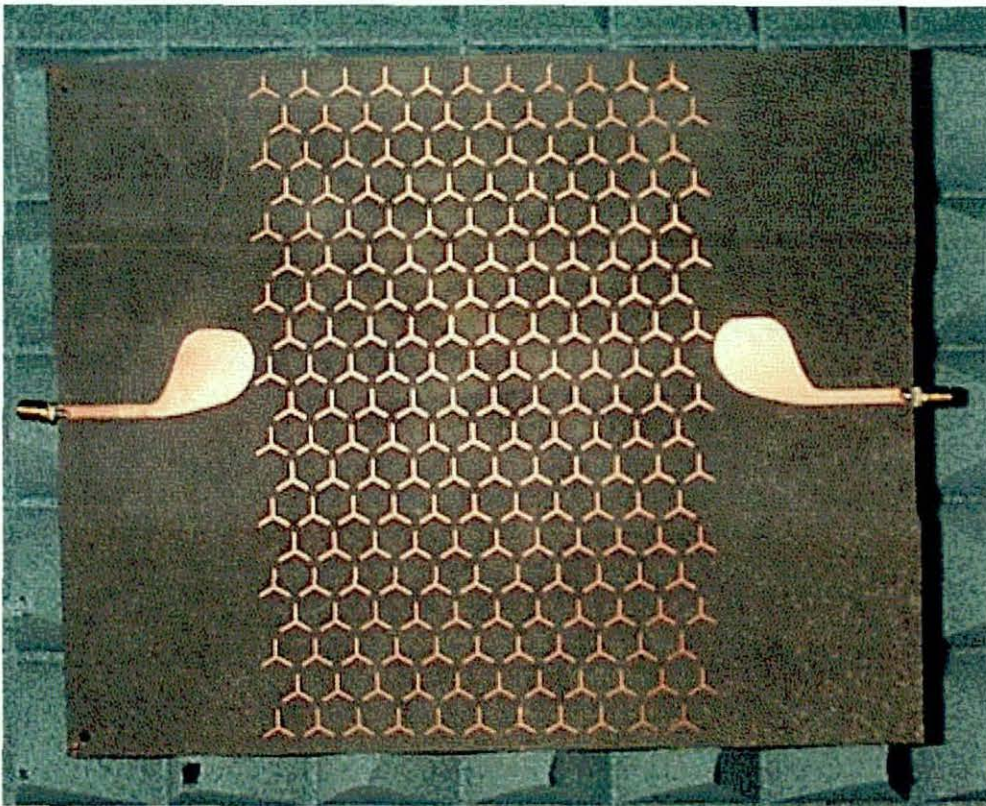


Figure 5.1: Prototype fabricated to measure propagation properties of a tripole periodic array

The tripole modeled in Figure 5.2 has the lattice periodicity $D = 8\text{mm}$, length $L = 3.5\text{mm}$, dielectric constant $\epsilon_r = 2.2$, Thickness = 1.125mm and $\alpha = 60^\circ$. The results show an absolute stopband of 3.5 GHz, starting from 18.3 GHz. to 21.8 GHz. The TM stopband of 6.7 GHz starts from 18.3 Ghz to 25 Ghz and the TE bandgap of 6.6 GHz starts at 15.2 GHz to 21.8 GHz.

Comparing the tripole array to the cross dipole array (Section 4.4), the TE mode starting bandgap frequency of the tripole array does not vary over a large range with the propagation direction. This would be an advantage in an application that requires a 'stable' bandgap.

It is observed that the TM_0 mode which begins at 0 Hz is above the TEM line of the dielectric slab until approximately 17.4 GHz in the ($\Gamma - X$) direction and 17.3 GHz in the ($\Gamma - M$) direction; then the TM_0 mode goes below the TEM line into the slow wave region. The TM_0 mode above the TEM line of the dielectric slab yields very shallow minima from its characteristic determinant. The TM mode in this fast wave region is classified as transmitted wave off the substrate [5].

From the measurement (Figure 5.3), the TE bandgap starts at 14.2 GHz in the 30° propagation direction ($\Gamma - X$) and moves up to 14.5 GHz at 0° propagation direction ($\Gamma - M$). The result does show the tripole is a more stable element for achieving TE bandgap in all planar directions.

From Figure 5.3, it is also observed that there is some sort of propagation around 17.15 GHz in the 0° direction ($\Gamma - M$) and 17.6 GHz in the 30° direction ($\Gamma - X$); from the modelling this would be the TM_0 mode. In addition, it is noticed that the TM_0 mode is only being measured after it goes below the TEM line of the dielectric slab into the slow wave region.

It is found that there is a gain of 6-8 dB before the stopband, likewise the tripole elements have also become guiding elements for the transmitting Vivaldi antenna. In the passband frequencies, it concentrates the fields in the direction of the antenna onto the dielectric slab thus increasing its directivity. In fact, from the prediction in Figure 5.2, the TE_0 surface mode is below the TEM line of the dielectric substrate. This means that the array

is slowing the wave propagation down even more and effectively it is like increasing the effective dielectric constant of the substrate. From the point of view of a higher dielectric constant substrate, the fields are naturally more bounded to the substrate and therefore increases its directivity and gain.

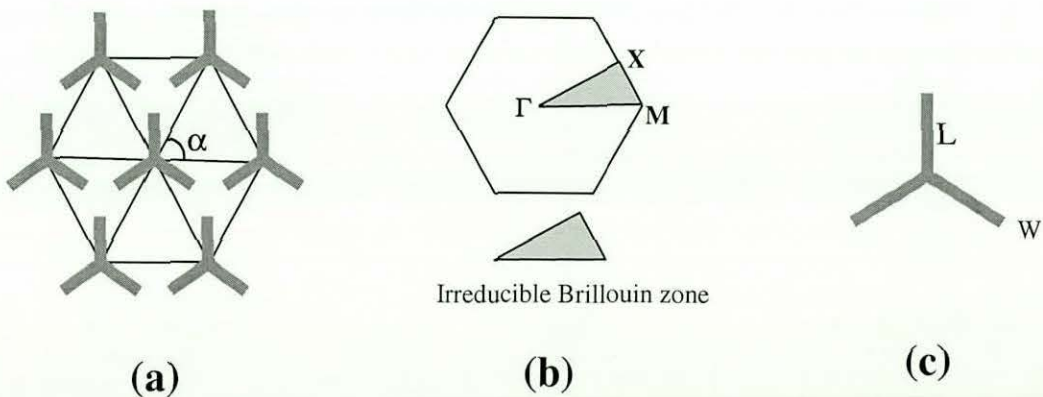
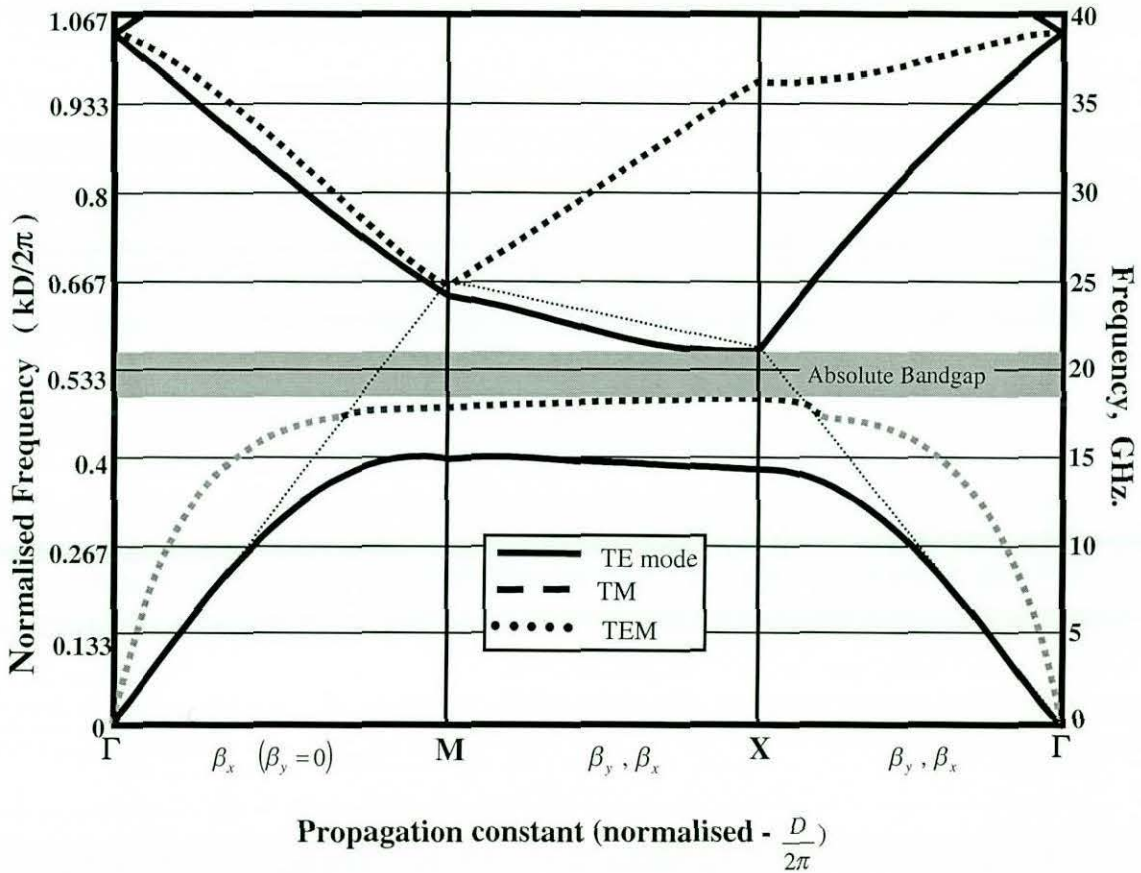


Figure 5.2 : TE (line) and TM (dash) modes of a tripole array in a triangle lattice. (a) Direct lattice, (b) Reciprocal lattice and its irreducible Brillouin zone, (c) $L = 3.5\text{mm}$, $W = 0.5\text{mm}$, periodicity $D = 8\text{mm}$, $\epsilon_r = 12$, Thickness $s = 0.5\text{mm}$, $\alpha = 60^\circ$.

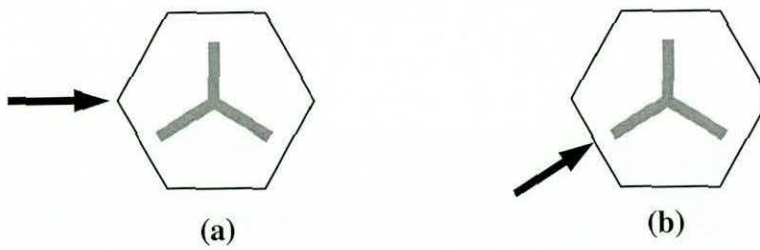
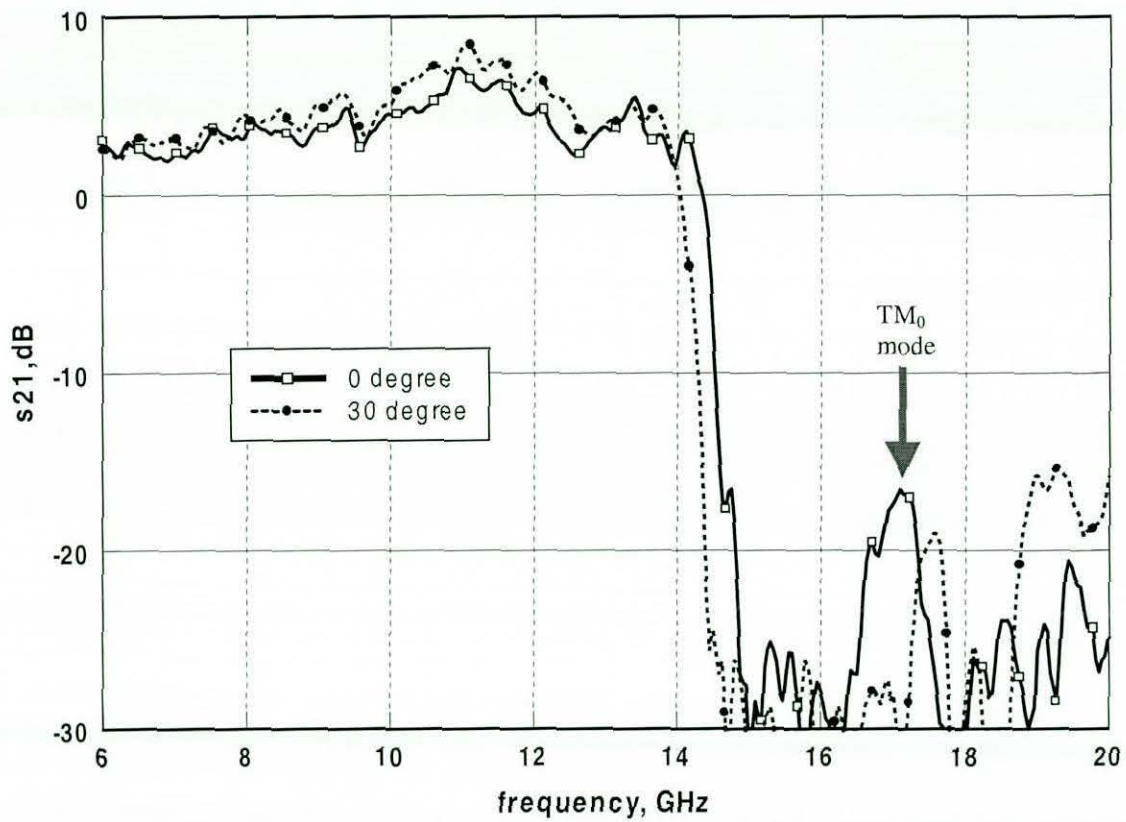


Figure 5.3 : Measurement results of the tripole array from Figure 5.2,
 (a) 0° (x direction), (b) 30° (xy direction)

5.3 Radiation Pattern of a Tripole Periodic Array on a Vivaldi Antenna

The tripole array used for the measurement of radiation pattern has a triangular lattice ($\alpha = 60^\circ$) with the periodicity $D = 12\text{mm}$, Length $L = 5\text{mm}$ and it is printed on a RT-Duroid dielectric slab with $\epsilon_r \approx 2.2$ and Thickness $s \approx 1.125\text{mm}$ [6].

The predicted dispersion diagram of the tripole array is shown in Figure 5.4. The TE bandgap begins at 10.4 GHz in the ($\Gamma - X$) direction and increase to 10.7 GHz in the ($\Gamma - M$) direction. The TM bandgap start around 12.3 GHz for all directions.

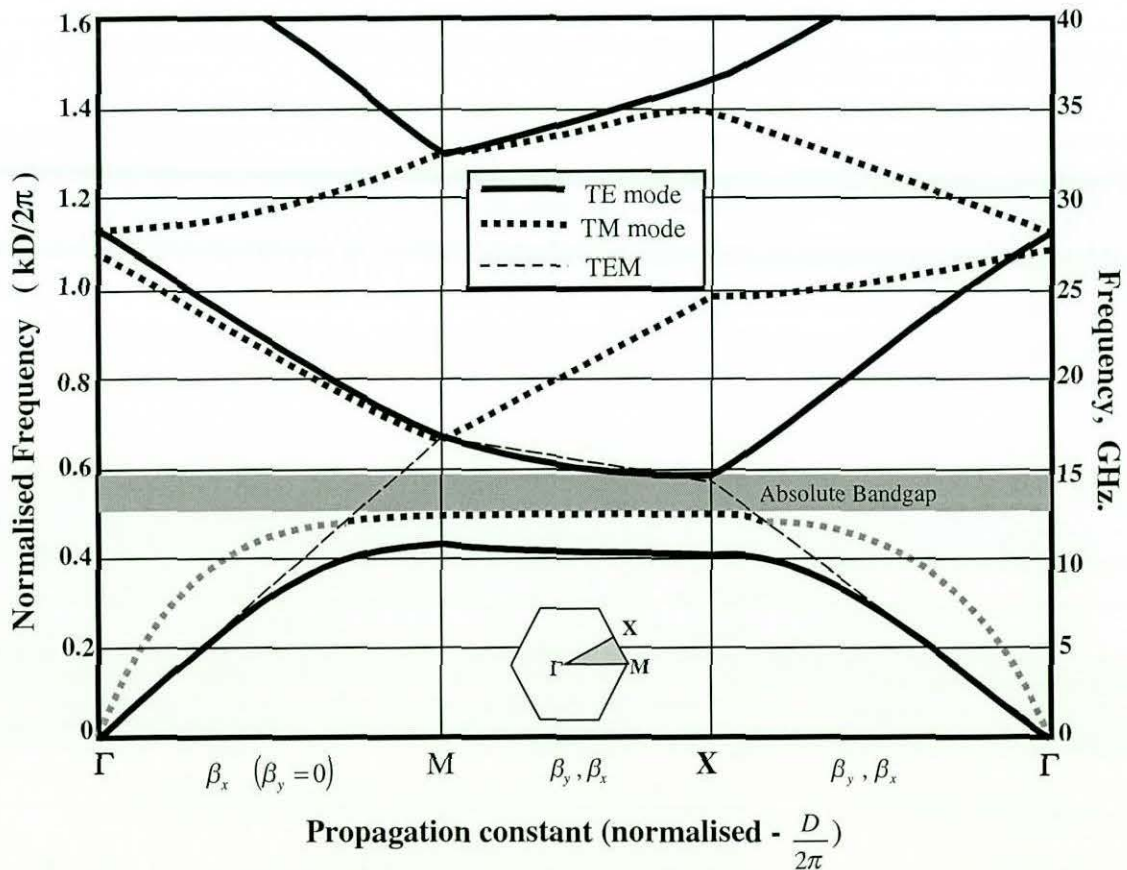


Figure 5.4 : TE (line) and TM (dash) modes of a tripole array in a triangle lattice (insert - Reciprocal lattice and its irreducible Brillouin zone), $L = 5\text{mm}$, $W = 0.5\text{mm}$, periodicity $D = 12\text{mm}$, $\epsilon_r = 12$, Thickness $s = 0.5\text{mm}$, $\alpha = 60^\circ$.

From the measured results in Figure 5.5 which are of good agreement with the prediction, the TE bandgap begins at 10.3 GHz in (Γ - X) direction and increases to 10.7 GHz in (Γ - M) direction. The TM bandgap starts at 12.2 GHz in (Γ - M) direction and increases to 12.4 GHz in (Γ - X) direction.

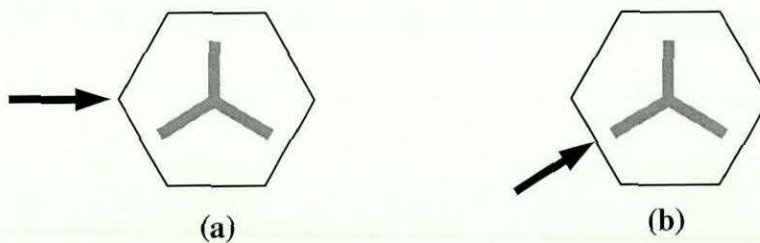
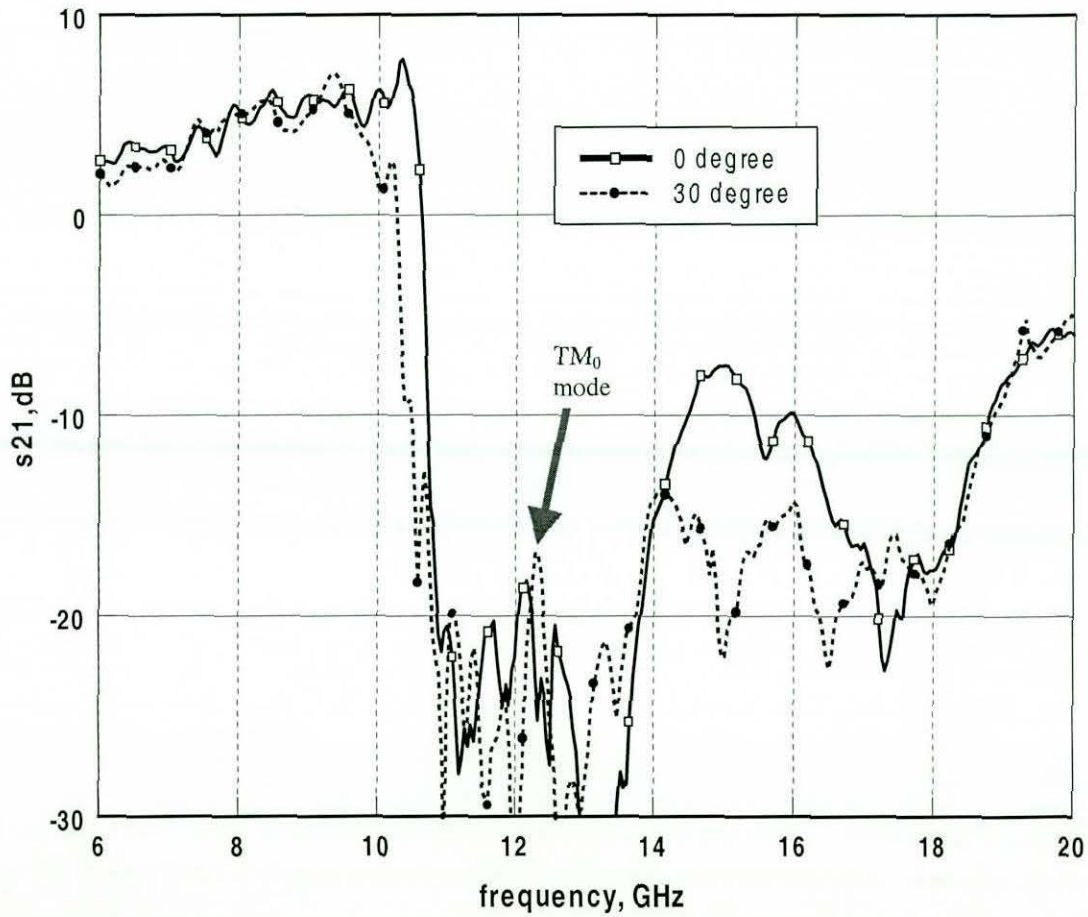


Figure 5.5 : Measurement results of the tripole array from Figure 5.4,

(a) 0° (x direction), (b) 30° (xy direction)

The radiation patterns presented for comparison are of a Vivaldi antenna with and without a tripole periodic array. The setup of radiation pattern measurement is shown in Figure 5.6a. The displayed result shows the radiation patterns for 4 frequencies before and after the bandgap in the E- and H-planes.

In Figure 5.6 b and c , the radiation pattern is before the stop band at 10 GHz. Both the E- and H-planes of the antenna with the tripole array show the radiating properties of a leaky wave antenna. The main beam indicates the power is concentrated towards the direction that the antenna is pointing and having many small side lobes all round. This explains the gain experienced before the bandgap mentioned both in this chapter and in Chapter 4.

In Figure 5.6d, using a X band horn placed 50 inches (117 cm) in the direction of the antenna, the system is normalised from 8.2 to 10.5 GHz. With the tripole array on, the stopband begins at around 10.2 GHz. The tripole is in the position where propagation is in the ($\Gamma - X$) direction and it exhibits gain from 8.2 to 9.4 GHz with a maximum gain of 3.5 dB at 8.4 GHz.

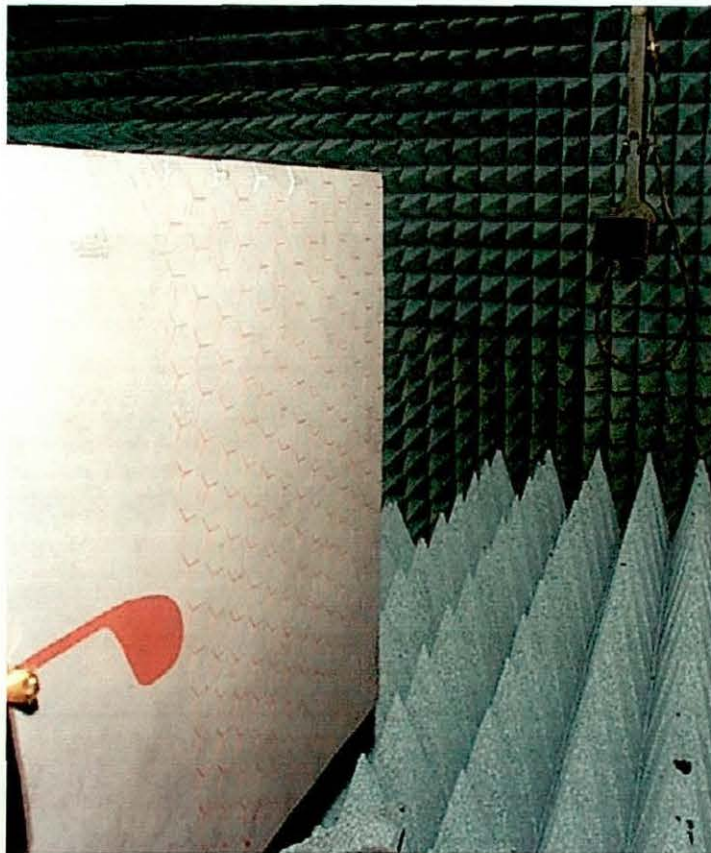


Figure 5.6a: Photo of the setup for radiation pattern measurement

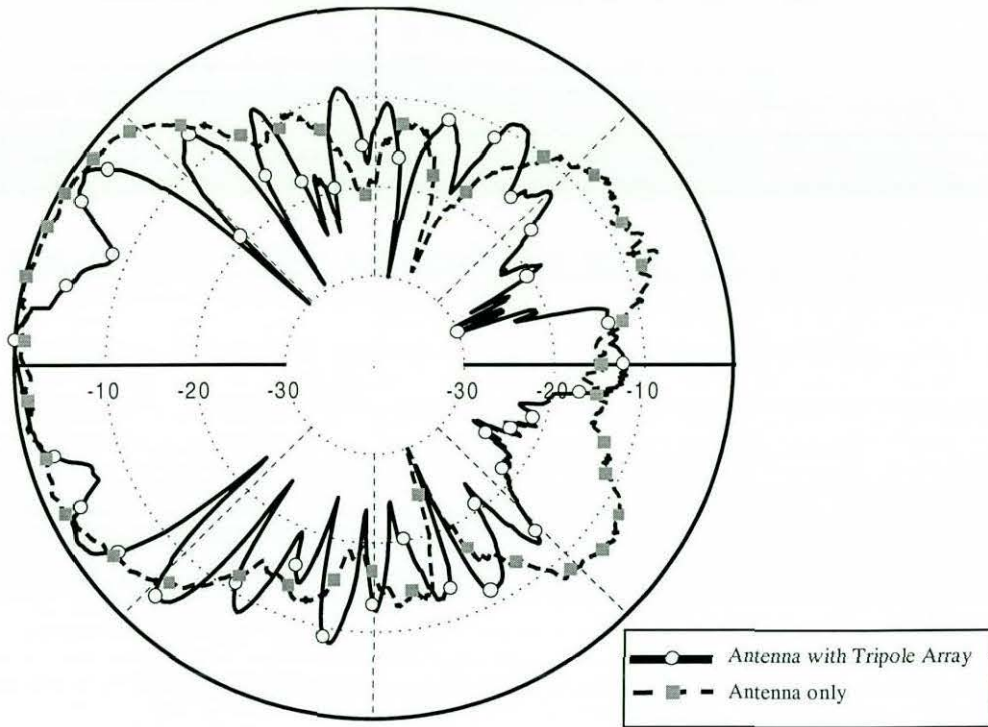


Figure 5.6b : H-plane radiation pattern at 10 GHz

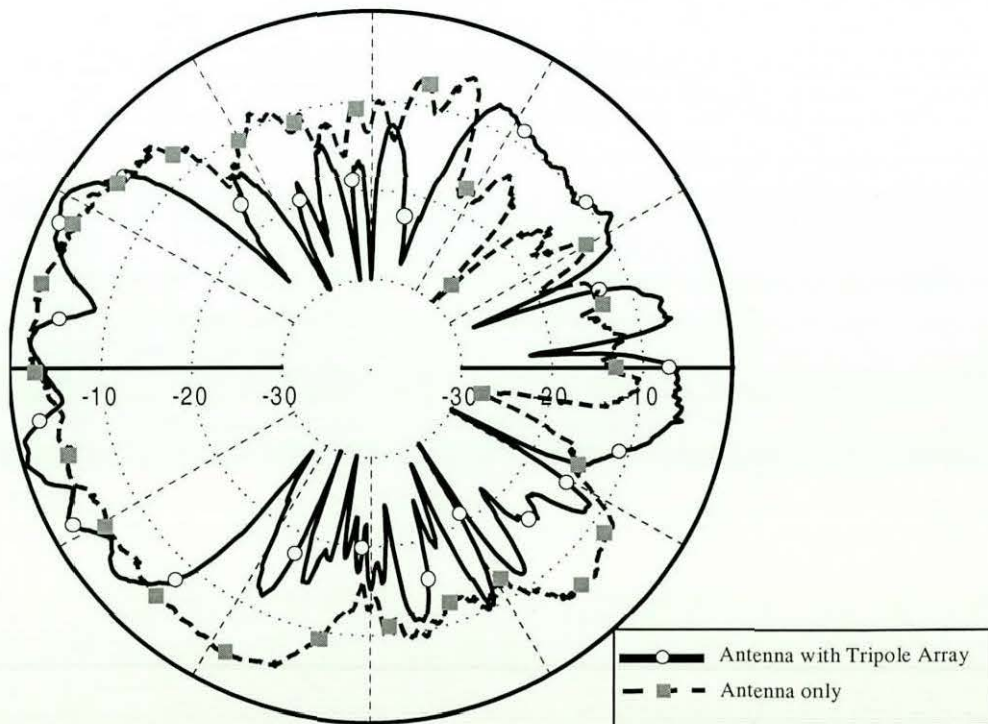


Figure 5.6c : E-plane radiation pattern at 10 GHz

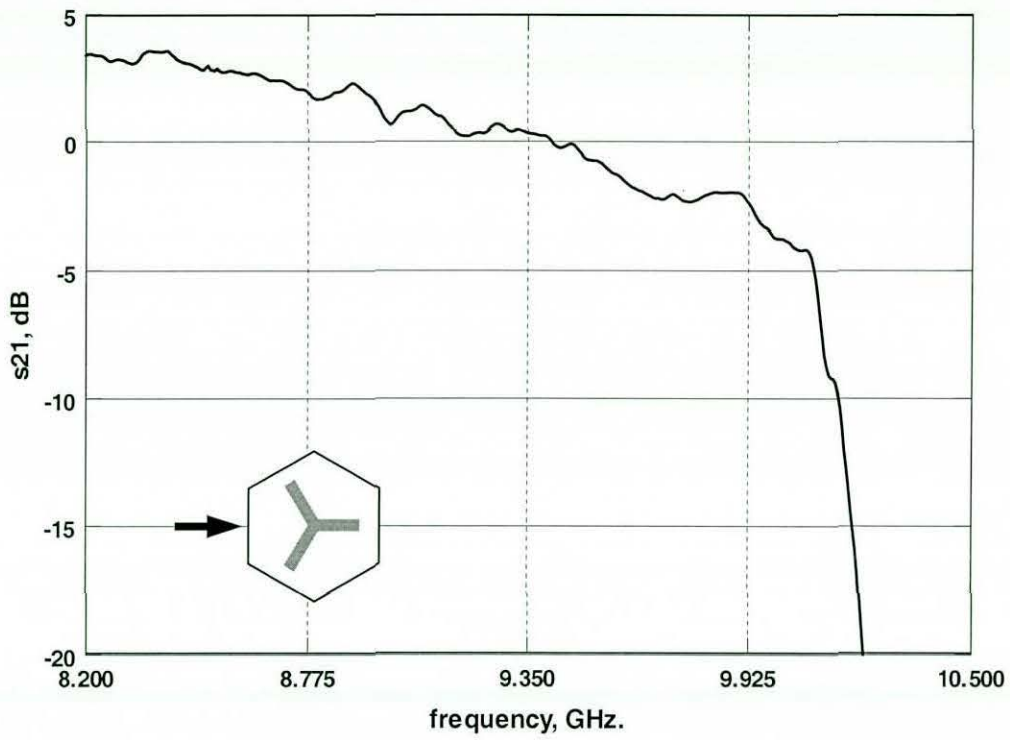


Figure 5.6d: Gain measurement for a tripole periodic array on a Vivaldi antenna.

Figure 5.7 shows radiation pattern at the beginning of the bandgap at 10.5 GHz. In the H-plane, the bandgap has just been formed with a suppression of 22 dB at an angle of $\pm 10^\circ$ in the direction of the antenna. The energy is reflected back towards the feed. From the measurement, the energy seems to concentrate at $\pm 50^\circ$ behind the feed.

The E-plane measurement is on the same plane as the dielectric slab where the antenna and tripole array is printed. On this plane, the tripole array that is printed in front of the transmitting antenna is expected to stop any propagation in front of the antenna. From the measurement, the suppression extends to a much wider angle in the direction of the antenna.

Figure 5.8 presents the measurements at 11 GHz where the TE bandgap is well established. The suppression in the H-plane has extended to $\pm 20^\circ$ and in the E-plane the suppression is almost $\pm 90^\circ$. Comparing with the radiation pattern in Figure 5.7, there are signs that the main beam is moving from either side of the antenna towards the front.

Figure 5.9 presents the radiation pattern at 11.6 GHz where, in the H-plane the main beam has moved to $\pm 45^\circ$ in the direction of the antenna. Comparing the E-plane for 10.5 GHz, 11 GHz and 11.6 GHz, it is evident that main beam has moved in the same direction as in the H-plane but at a slower rate. Likewise due to the position of tripole array in front of the antenna, the E-plane has exhibited suppression at a large angle in the direction of the antenna.

From the observation made from the radiation patterns, when the bandgap occurs the energy is prohibited from propagating in the direction of the tripole array; it is reflected and radiated as leaky waves at an angle to the dielectric slab. The main beam of the leaky waves also moves as the frequency increases which is a characteristic of a leaky wave antenna. Since for a certain design of the array elements can yield a large bandgap and design requirements can be set to not only stop the propagation in an unwanted direction, but it could also control and steer the reflected beam by varying the element dimensions by a little.

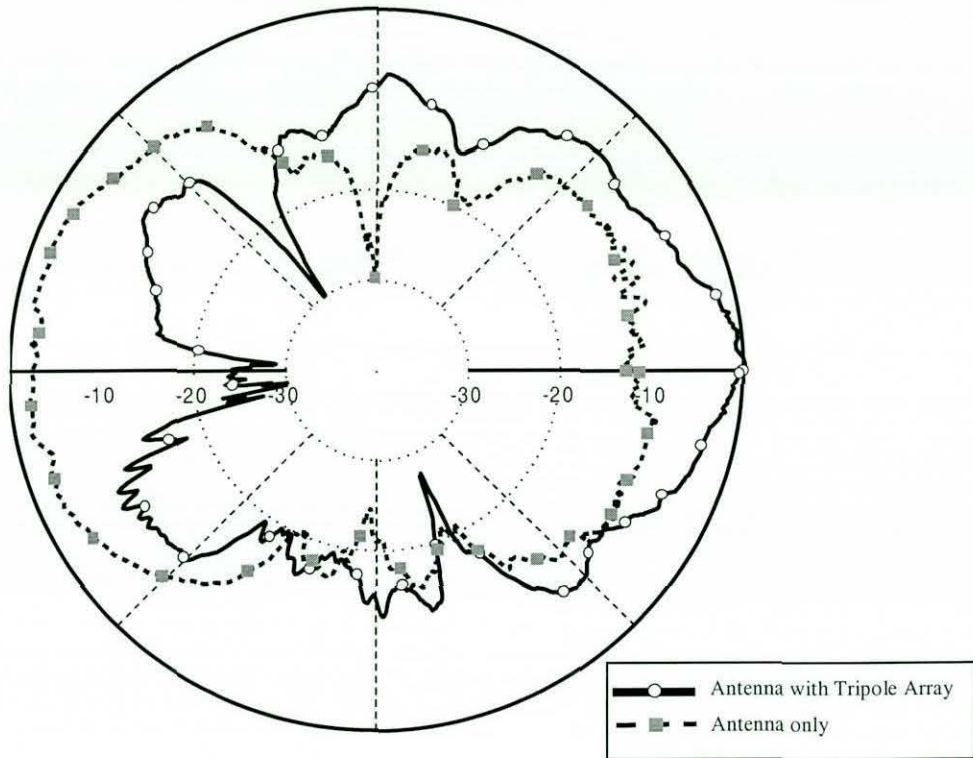


Figure 5.7a : H-plane radiation pattern at 10.5 GHz

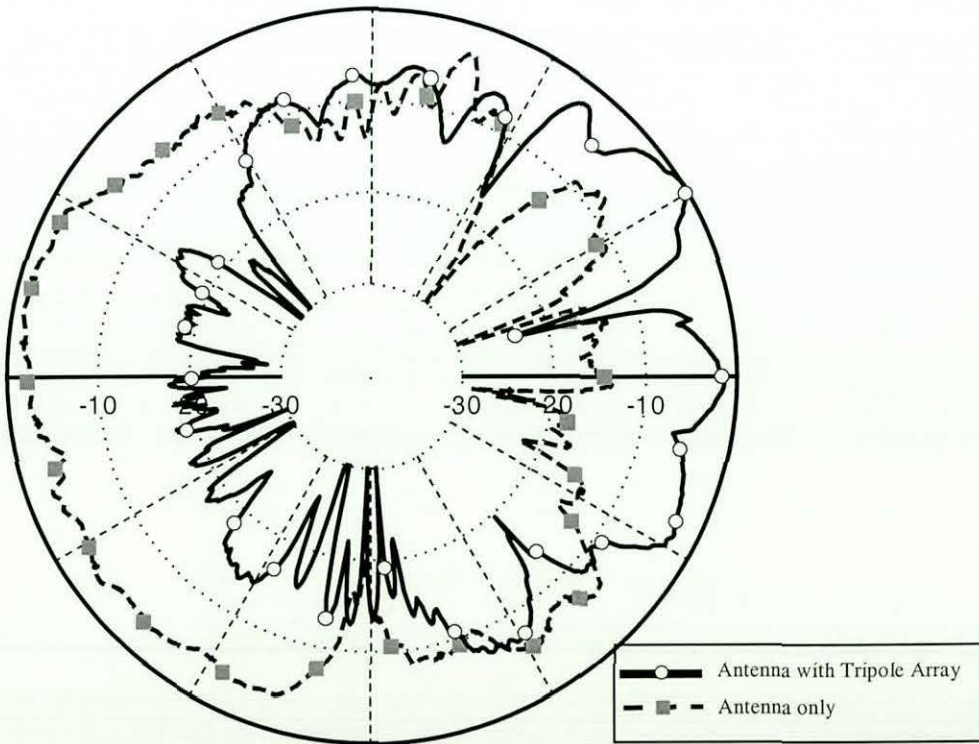


Figure 5.7b : E-plane radiation pattern at 10.5 GHz

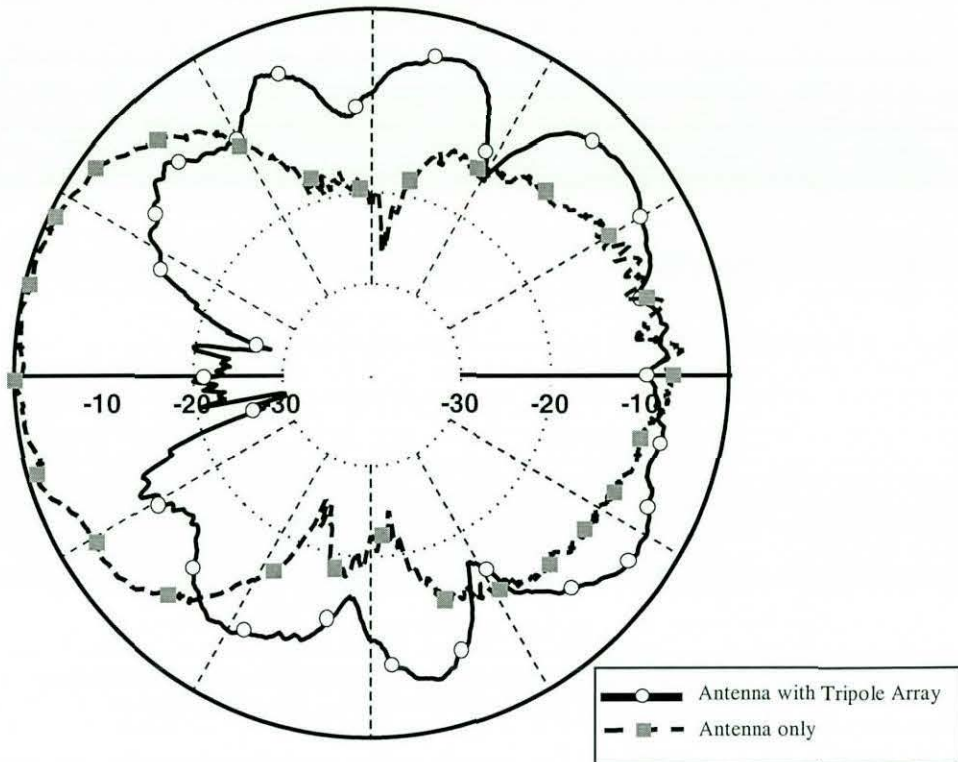


Figure 5.8a : H-plane radiation pattern at 11 GHz

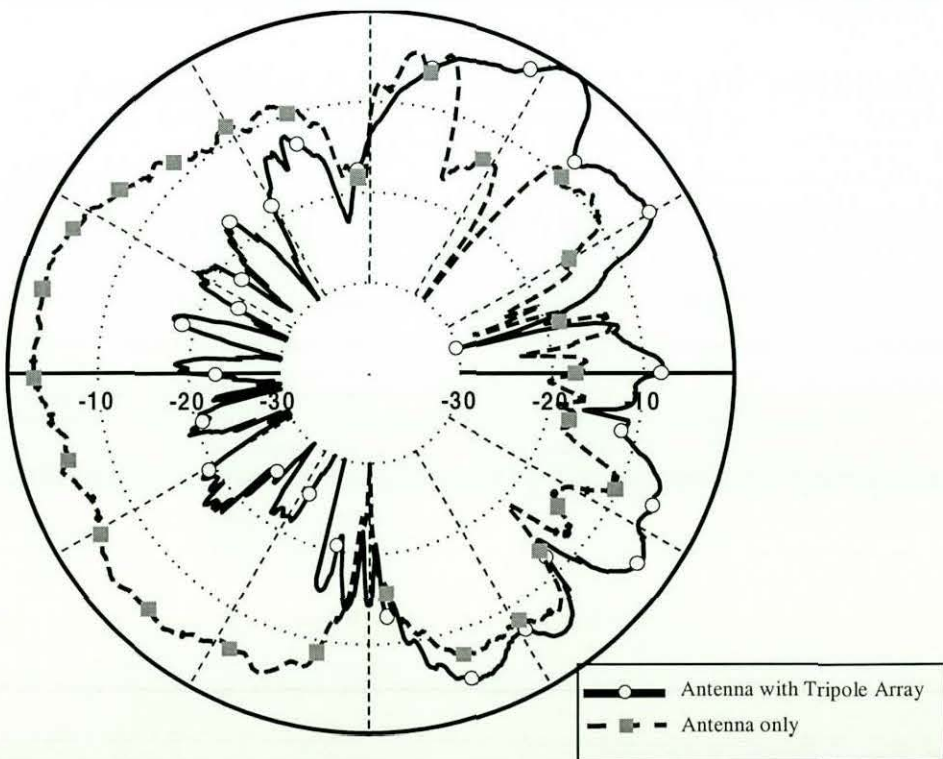


Figure 5.8b : E-plane radiation pattern at 11 GHz

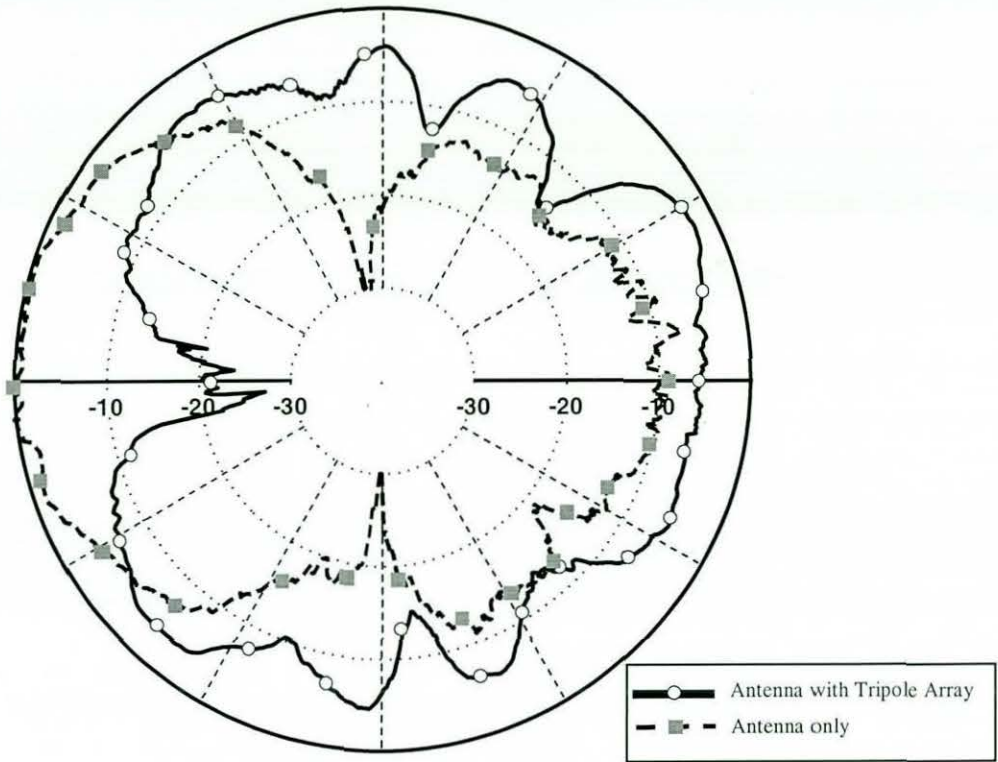


Figure 5.9a : H-plane radiation pattern at 11.6 GHz

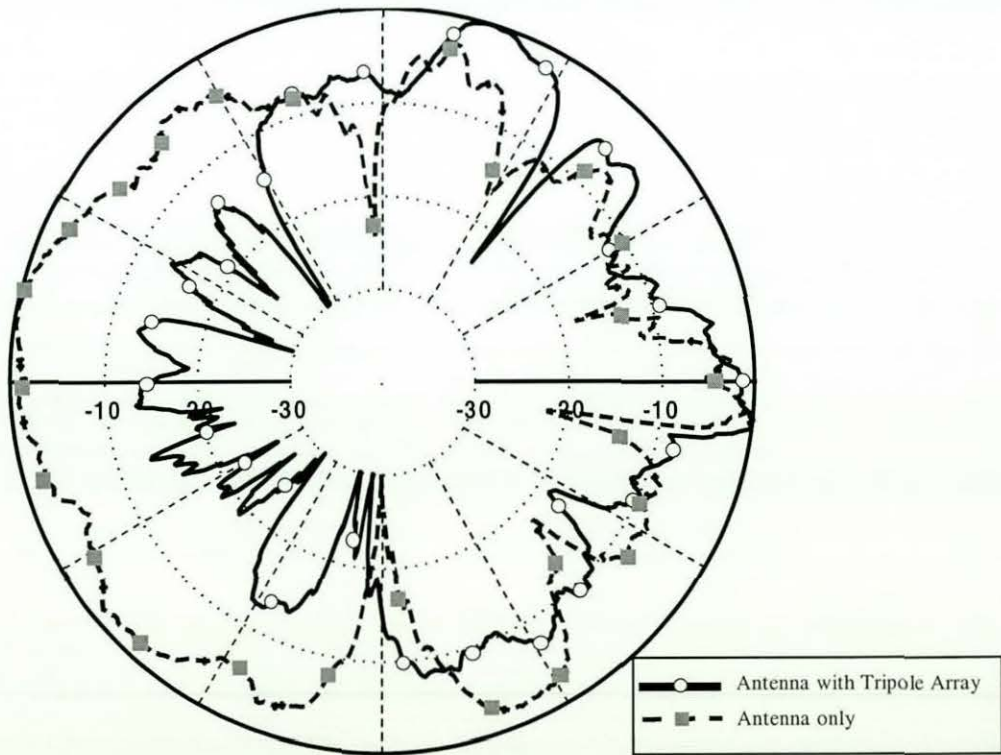


Figure 5.9b : E-plane radiation pattern at 11.6 GHz

5.4 Designing the Bandgap Frequency

The bandgap exhibited by such metallodielectric arrays is relatively large and usually more than adequate to cover the range of frequencies an application might require. An important point is where the bandgap begins and how can one design this. As an example, this section covers the effect that the tripole length dimension, dielectric constant and substrate thickness have on the absolute TE bandgap starting frequency. However in some applications, it might be essential to operate in the common TE and TM bandgap.

As observed in the tripole arrays examples given in this chapter, the absolute TE bandgap frequency is governed by the M point of the Brillouin zone which is propagation in the ($\Gamma - M$) direction with respect to the tripole orientation shown in Figure 5.1b.

Figure 5.10 shows the beginning of the TE absolute bandgap with respect to different tripole arm lengths for different dielectric constant substrates. The triangular lattice periodicity is fixed at 12mm and the substrate thickness is 1.125mm. Various arm lengths of the tripole element on different dielectric constant substrates are considered.

It is observed that for higher dielectric constant the TE absolute bandgap shifts down in frequency for a fixed tripole length; in fact as expected at a higher dielectric constant, the modes tend to 'compress' down towards lower frequencies. From the prediction, it also suggested that a larger L/D ratio would give rise to a larger bandgap [7].

Using trendline equations to describe the curves, one can easily design the beginning of the TE bandgap with respect to different tripole dimensions using such equations:

For $\epsilon_r = 2.2$, where $x = L/D$ and $D = 12\text{mm}$

$$\text{TE bandgap (absolute)} = 195.14x^3 - 200.6x^2 + 42.441x + 13.652$$

For $\epsilon_r = 3$,

$$\text{TE bandgap (absolute)} = 214.69x^3 - 21077x^2 + 42.857x + 12.941$$

For $\epsilon_r = 4$,

$$\text{TE bandgap (absolute)} = 175.94x^3 - 166.73x^2 + 27.966x + 13.522$$

For $\epsilon_r = 5$,

$$\text{TE bandgap (absolute)} = 153.85x^3 - 142.37x^2 + 20.514x + 13.388$$

For $\epsilon_r = 6$,

$$\text{TE bandgap (absolute)} = 139.99x^3 - 127.84x^2 + 16.708x + 12.974$$

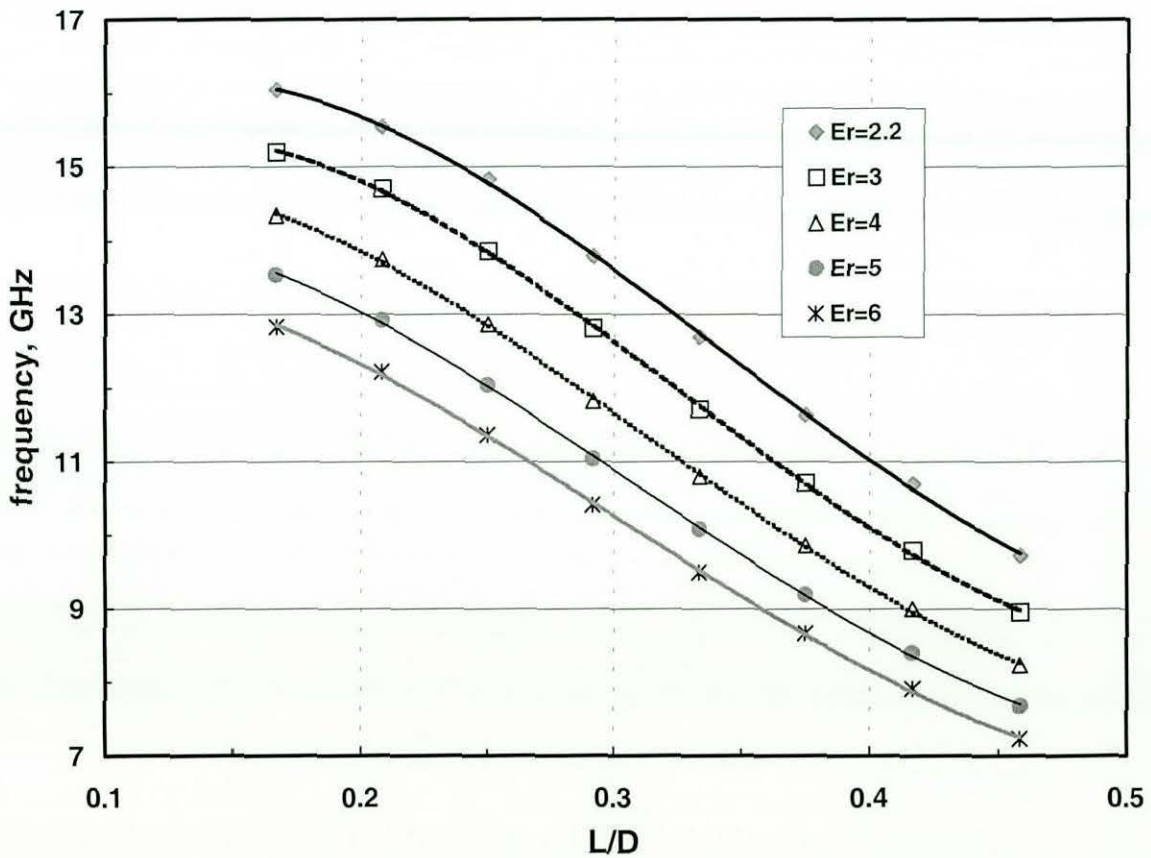


Figure 5.10 : Beginning of the TE absolute bandgap with respect to tripole's arm length and dielectric constant

In Figure 5.11, different substrate thicknesses and dielectric constants are modeled for a fixed lattice periodicity ($D = 12\text{mm}$) and tripole arm length ($L = 5\text{mm}$). From the observation, the TE absolute bandgap shifts down as the thickness increases and tends to 'stabilise'.

Likewise, using trendline equations to describe the curves:

For $\epsilon_r = 2.2$, where Thickness x in millimeter and $D = 12\text{mm}$, $L = 5\text{mm}$

$$\text{TE bandgap (absolute)} = -0.0012x^5 + 0.0258x^4 - 0.216x^3 + 0.9x^2 + 1.974x + 12.1$$

For $\epsilon_r = 3$,

$$\text{TE bandgap (absolute)} = -0.0014x^5 + 0.0294x^4 - 0.2512x^3 + 1.07x^2 + 2.41x + 11.49$$

For $\epsilon_r = 4$,

$$\text{TE bandgap (absolute)} = -0.0017x^5 + 0.037x^4 - 0.3144x^3 + 1.33x^2 + 2.96x + 11$$

The work achieved in this part of research has shown that with different substrate properties, the physical dimensions of the elements can be used to design and control the bandgap start frequency. Using the trendline equations as listed above could easily predict the beginning of the bandgap but this would limit to a tripole array on triangular lattice with fixed periodicity of 12mm as studied in this case.

Much work would be needed to be done as to the design requirements needed to be taken into consideration such as different lattices, different elements and different elements orientations to fully design the location of the absolute bandgap.

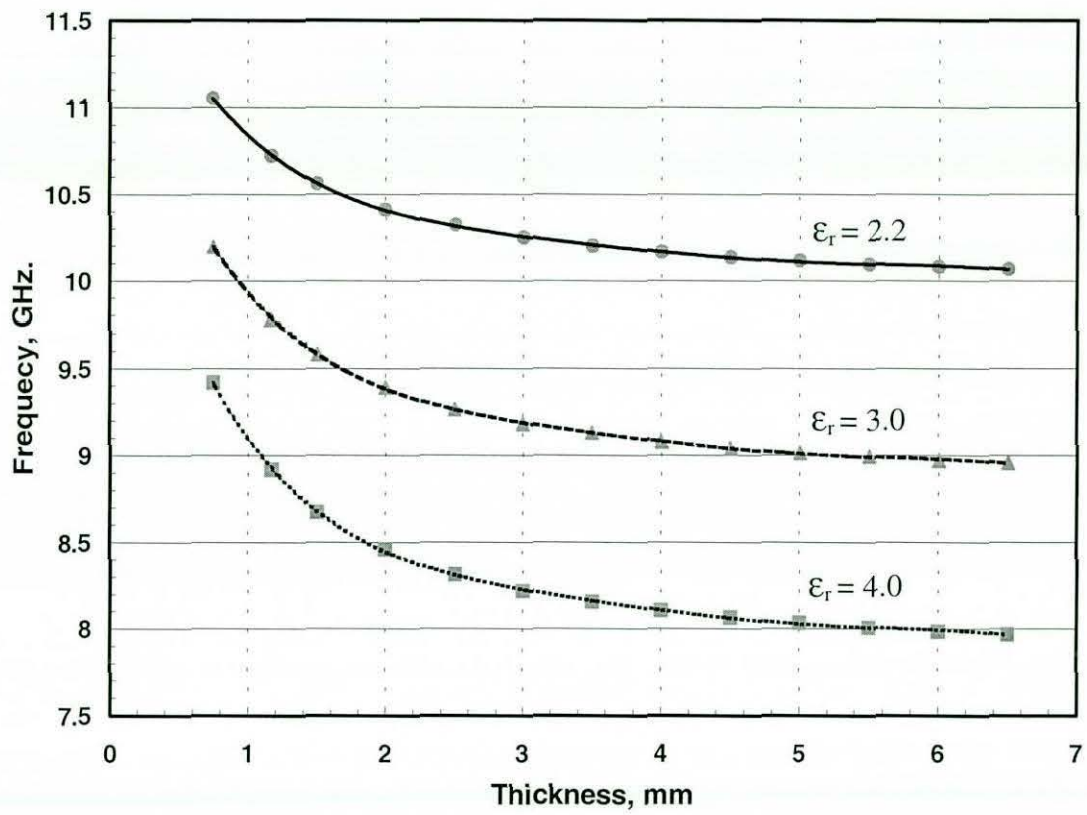


Figure 5.11: Beginning of the TE absolute bandgap with respect to substrate thickness and dielectric constant

5.5 Some Applications Investigated

5.5.1 Application for Tripole Array

Patch antennas were one application area investigated [8,9]. It is known that the main loss mechanism of a patch antenna is surface wave loss. This surface wave loss is mainly due to the TM_0 mode, which has no cutoff frequency. The objective is to enhance the performance of the patch antenna by surrounding it with an array that has an absolute bandgap in the region of the transmitting frequency. This 2-D periodic array will prevent any TM_0 mode surface wave at the transmitting frequency propagating in any direction along the surface of the dielectric slab. Therefore as desired, more energy is radiated from of the patch antenna.

Unlike in Chapter 4 and in this Chapter, the patch antenna is printed on a dielectric slab with a ground plane. It was shown in Chapter 3 that the computer model can incorporate this easily by reducing the thickness of the dielectric slab by half and including a very thin layer behind the slab with a very high loss tangent, to simulate a ground plane.

Different patch antennas are printed on 3 commercially available materials with different dielectric constants, RT-Duroid, MC3D and FR4. Tripole elements are chosen for the arrays because of its 'stable' and absolute bandgap properties (Section 5.2). All the arrays are designed to have the transmitting frequencies fall within their absolute TM bandgap region.

In Figure 5.14a, the patch antenna is printed on RT-Duroid 5880 with a dielectric constant 2.2 and a thickness of 1.125 mm. Its operating (resonant) frequency is at 12.07 GHz with a bandwidth of 0.2 GHz at -10 dB, and it establishes a measured reflection coefficient (s_{11}) of -14.9 dB. With the tripole array surrounding it, the operating frequency shifts a little to 12.11 GHz with a measured reflection coefficient (s_{11}) of -25.4 dB. Generally, a patch antenna has a very narrow frequency bandwidth and it is often desirable to increase this. From this design, the tripole array has improved the reflection coefficient by -10.5 dB and the bandwidth has increased to 0.25 GHz (25% increment) at -10 dB.

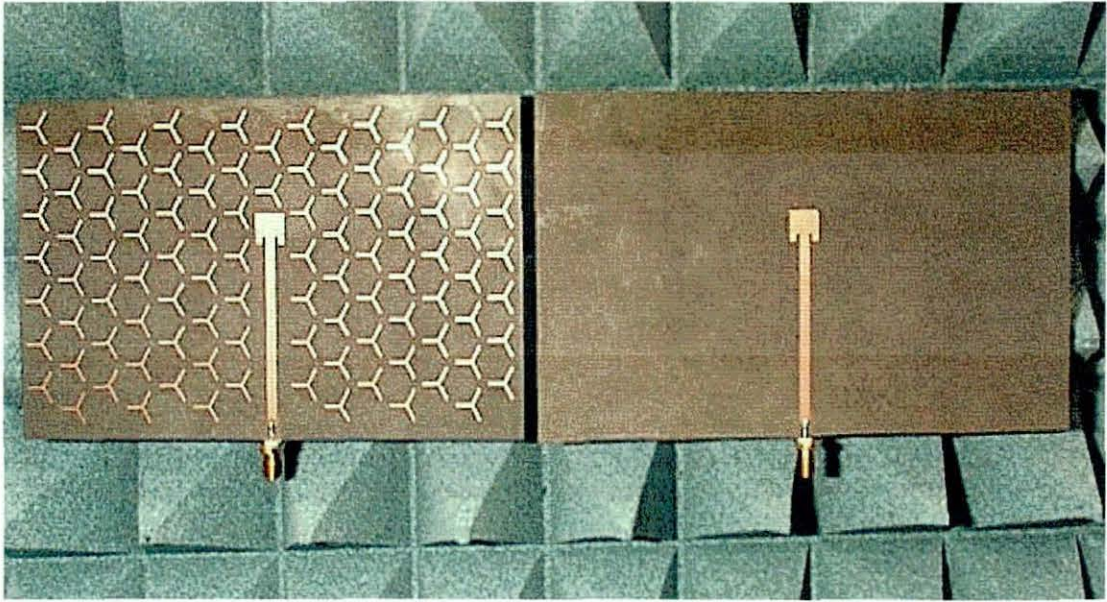


Figure 5.14a : Patch antenna printed on RT-Duriod with and without tripole array

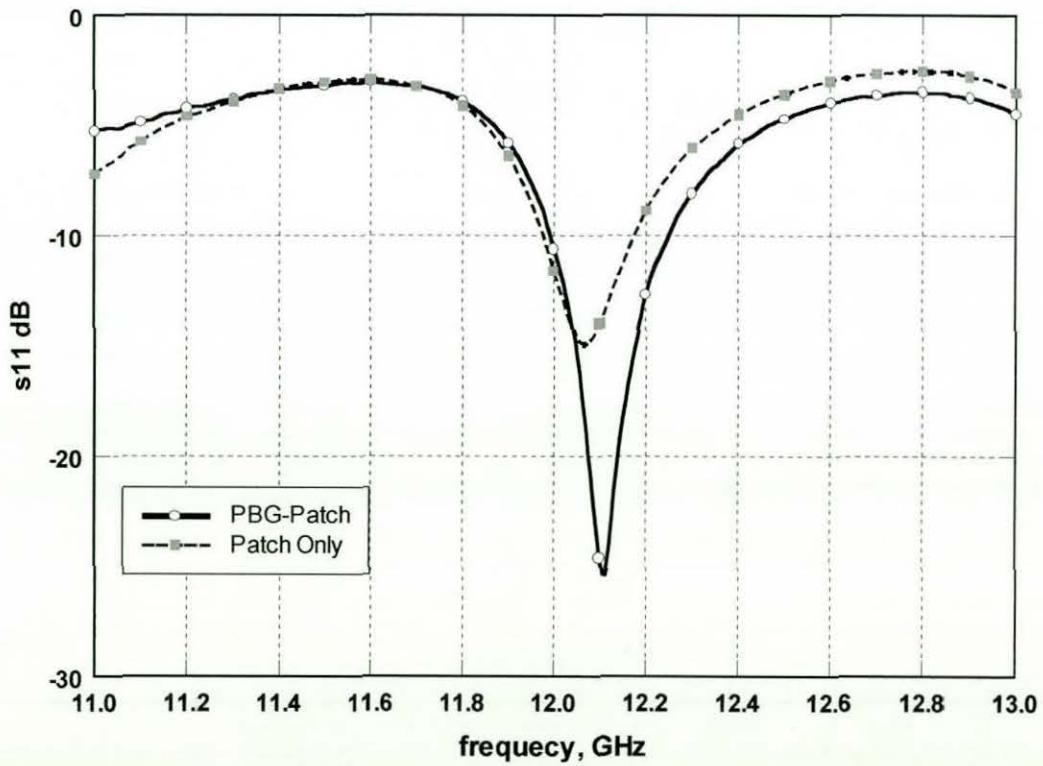


Figure 5.14b : Reflection coefficient (s11) of Patch antenna printed on RT-Duriod with and without tripole array

Figure 5.15a shows a patch antenna printed on a MC3D with a dielectric constant of 3.53 and thickness of 1.575 mm. Its operating frequency is 16.64 GHz with a bandwidth of 0.8 GHz at -10 dB and it shows a measured reflection coefficient of -21.9 dB. With the tripole array surrounding it, the operating frequency shifts slightly to 16.6 GHz with a measured reflection coefficient of -31.9 dB. From this design, the array has improved the reflection coefficient by -10 dB and the bandwidth has increased to 0.9 GHz at -10 dB.

Finally, Figure 5.16a shows a patch antenna printed on a FR4 with a dielectric constant of 4.88 and thickness of 1.6 mm. Its operating frequency is at 12.41 GHz with a bandwidth of 0.36 GHz at -10 dB and it shows a measured reflection coefficient of -22.7 dB. With the tripole array surrounding it, the operating frequency shifts a little to 16.6 GHz with a measured reflection coefficient of -38.2 dB. From this design, the tripole array has improved reflection coefficient by -10 dB and the bandwidth has increased to 0.43 GHz at -15.5 dB. For the other resonant which is another harmonics, it is introduced by the spurious effect due to the feeding method.

Dielectric Materials	Patch antenna			Patch antenna with Tripole array		Improvement	
	Operating frequency (GHz)	Reflection coeff. (dB)	Bandwidth (GHz)	Reflection coeff. (dB)	Bandwidth (GHz)	Reflection coeff. (dB)	Bandwidth Increment (%)
RT-Duriod	12.07	-14.9	0.2	-25.4	0.25	-10.5	25
MC3D	16.64	-21.9	0.8	-31.9	0.9	-10	12
FR4	12.41	-22.7	0.36	-38.2	0.43	-15.5	19.4

From the results summarised in the table above, it can be seen that with the tripole arrays there is an apparent improvement in the performance of the patch antenna by eliminating the TM_0 mode surface waves. Another positive effect from the inclusive of tripole array was that it increases the bandwidth of the patch antenna.

It is known that for patch antenna with higher dielectric constant substrate, the surface wave losses become more apparent and thus the patch antenna become highly inefficient. Arrays of such can be design around the patch antenna to improve their performance. As

a comparison with the design in Qian [8] which needed vias to connect the square pads (the array) to the ground, the tripole array option might be easier to fabricate to achieve desired improvement.

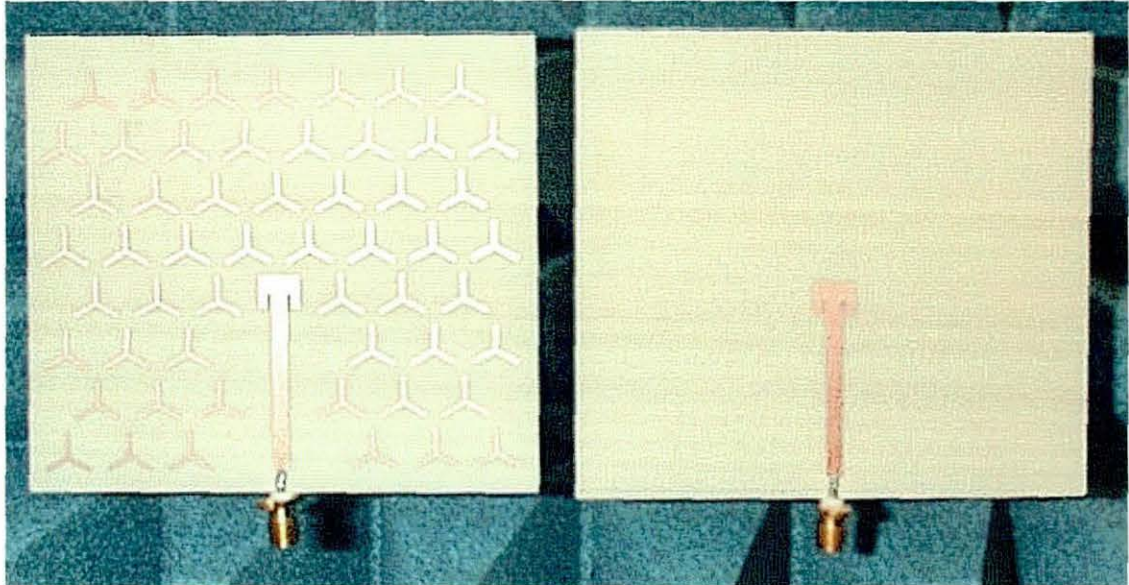


Figure 5.15a : Patch antenna printed on MC3D with and without tripole array

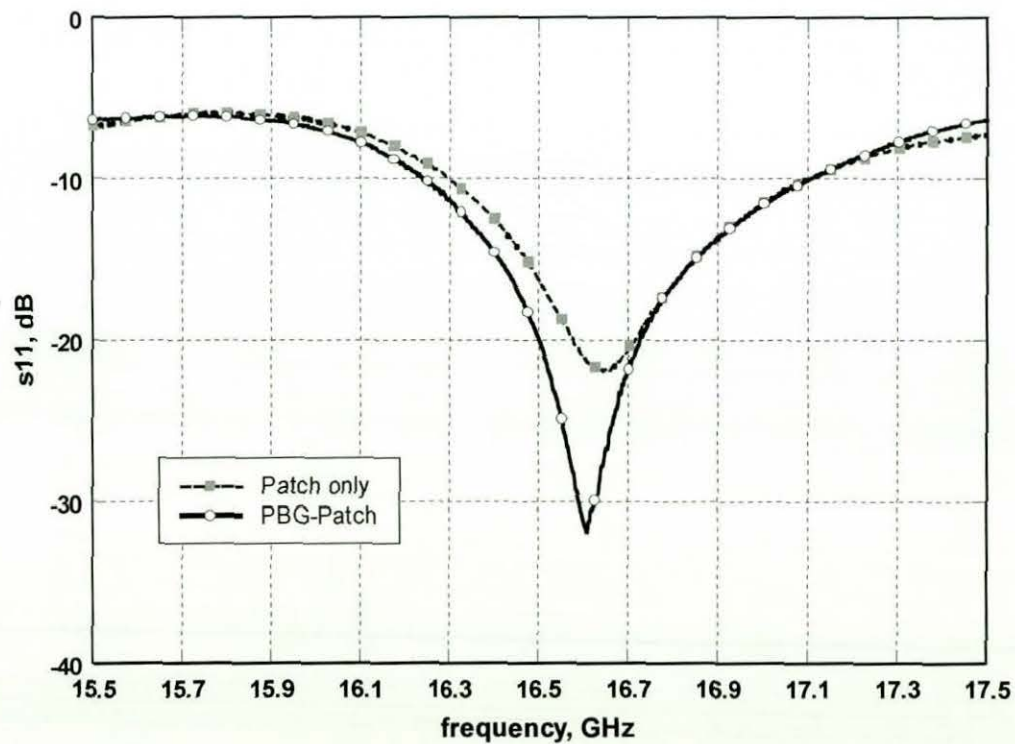


Figure 5.15b : Reflection coefficient (s_{11}) of Patch antenna printed on MC3D with and without tripole array

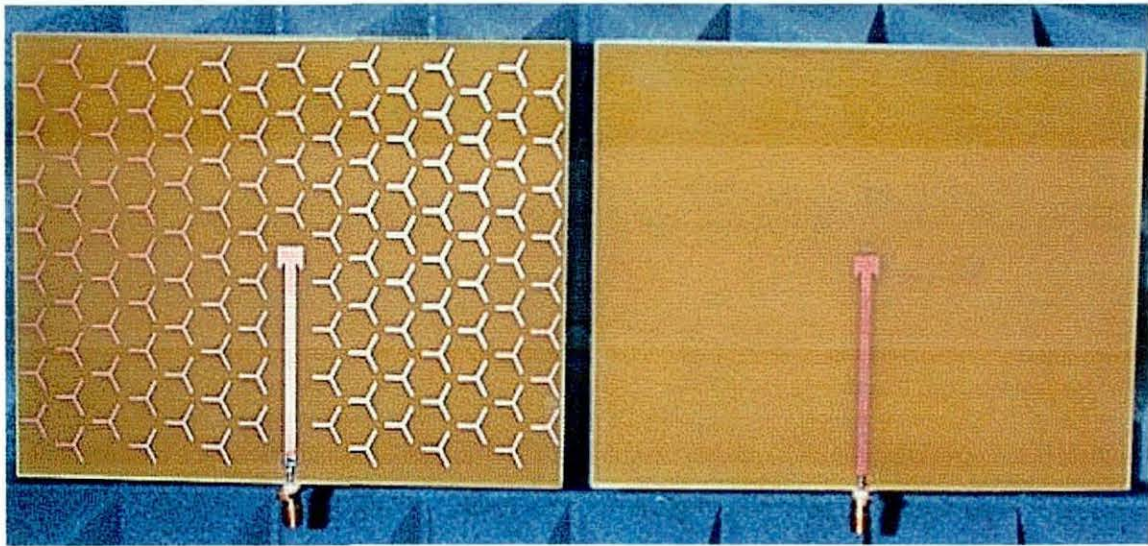


Figure 5.16a : Patch antenna printed on FR4 with and without tripole array

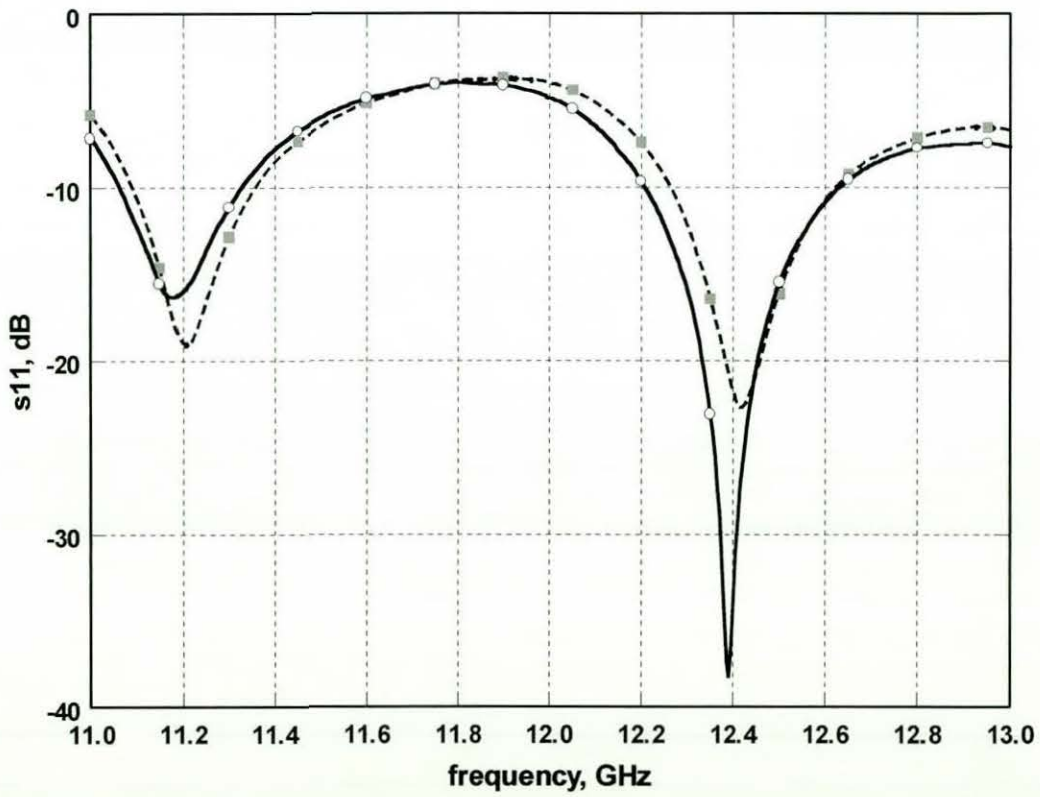


Figure 5.16b : Reflection coefficient (s_{11}) of Patch antenna printed on FR4 with and without tripole array

5.5.2 Application for Dipole Array

Another application presented, uses a periodic array of conducting dipoles which is a form of 1-D 'photonic crystal'. The propagation incidence is only restricted to one direction, which is perpendicular to the length of the dipole. The advantage is with the shape of a dipole element, it can be packed closely together thus increases the packing density and reduces the size of the device.

Here we discuss the bandgap arising from a two dimensional array of conducting dipole elements printed on a grounded dielectric substrate. Figure 5.17a shows a 50Ω microstrip line printed on top of a double sided polyester dielectric sheet ($\epsilon_r = 3$) with a thickness of 0.071 mm. Beneath the dielectric sheet, a dipole periodic array is printed with the dipole length $L=15\text{mm}$, width $w=1\text{mm}$ and a periodicities D_x and D_y of 5mm and 16.5mm respectively.

The dielectric sheet is pasted on an RT-Duroid 5880 with dielectric constant and thickness of 2.2 and 1.125 mm respectively. For the electromagnetic analysis, *EMSihtTM* (Applied Wave Research) [10] has been used. The effect of the connectors was removed in the simulation by de-embedding it to about on guided wavelength (at 10 GHz) from the edge of the substrate.

Figure 5.17b shows the predicted and measured S21 of the microstrip line with the dipole array designed to gives a centre bandgap frequency of 10 GHz. The predicted bandgap of this structure is from 8.9 to 12 GHz and the measured bandgap is from 8.9 to 12.9 GHz. Regarding the stopband, the measured bandgap has a width of 40% between the -10 dB points, whereas in the predictions is about 30%.

From the results in Figure 5.17b, the dipole array can be used as 1-D planar 'photonic crystal' and the tripole array as 2-D planar 'photonic crystal' for filtering purpose in microstrip technology [11,12].

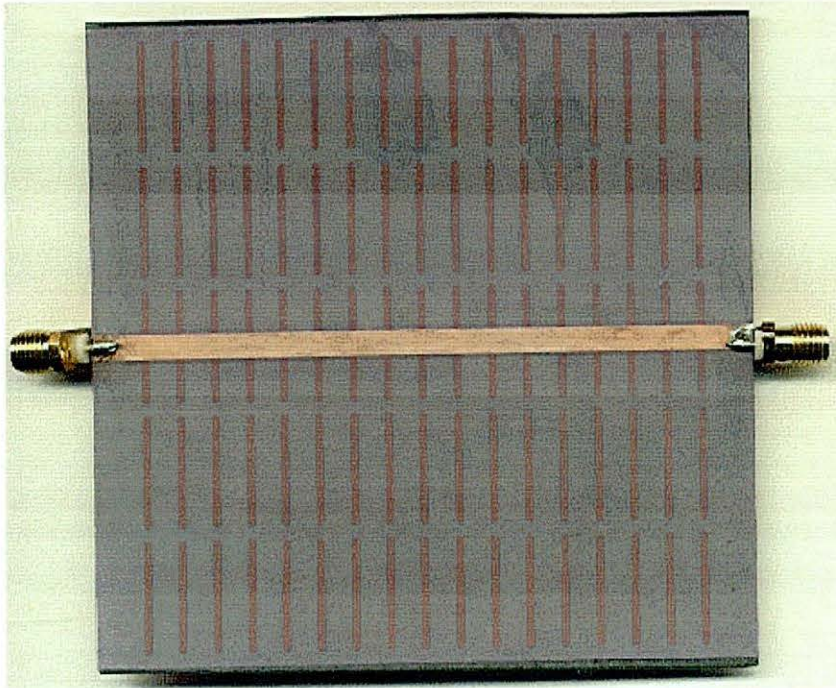


Figure 15.7a photograph of the geometry of a microstrip line on a dipole array

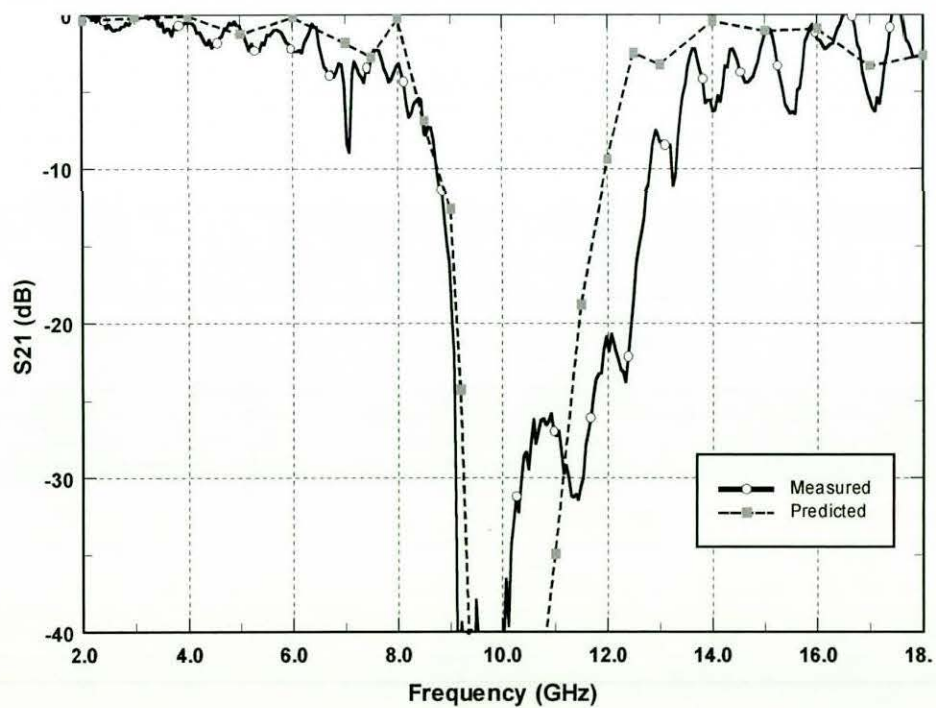


Figure 5.17b : Insertion loss (s_{21}) of the microstrip line with the dipole array

With the results observed in Figure 5.17b, the microstrip line is replaced with a 5 GHz resonator. It is known that a resonator has harmonic frequencies multiple to its fundamental frequency. The objective in this section is to suppress the first harmonic (10 GHz).

The resonator in Figure 5.18a has a conducting dipole array with parameters as in Figure 5.17a. The dipoles underneath the resonator have been deliberately removed in order to alleviate any strong coupling that may adversely degrade its performance. The effects of having dipoles under the resonator will cause the fundamental resonant to shift down in frequency and the higher harmonics will not be absolute multiples of its fundamental frequency.

In Figure 5.19a (predicted) and 5.19b (measured), the dipole array was able to eliminate the first harmonic (10 GHz) but it is accompanied with a 2 dB degradation of the insertion loss at 5 GHz. However, it can be observed that the resonator with the dipole array has a higher Q factor by about 30% as compared with the conventional half-wavelength resonator [13].

In order to improve the band gap near 9 GHz, a pragmatic approach has been taken whereby two dipole arrays were situated either side of the resonator (Figure 5.18b). Varying the dimensions of the dipoles by about 15%, two distinct but close resonances (near 10 GHz) appear and thus an increase of the bandgap is obtained. The Q-factor has also improved by about 30% with a 3dB degradation of the insertion loss at 5 GHz compared with the conventional half-wavelength resonator (Figure 5.19b).

With regards to the single resonator, a narrower Q factor has been observed as a result of the loading of the dipole array. In addition, its first harmonic has been eradicated by placing the band gap near 10 GHz. These kind of resonant structures are expected to find applications particularly in low phase noise microwave and mm-wave oscillators, highly selective mm-wave filters [14], active FSS and antennas.

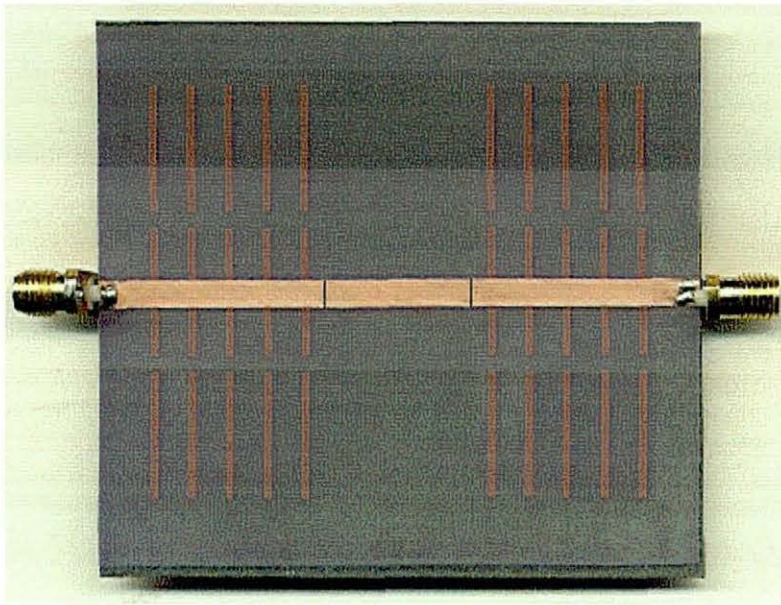


Figure 5.18a : Photograph of the geometry of a microstrip line and resonator with a dipole array.

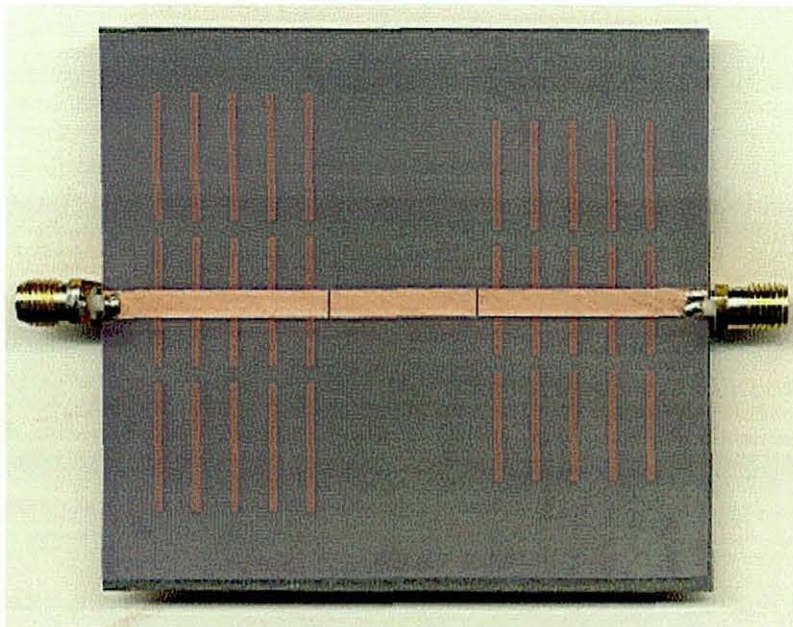


Figure 5.18b : Photograph of the geometry of a microstrip line and resonator with 2 different dipole arrays.

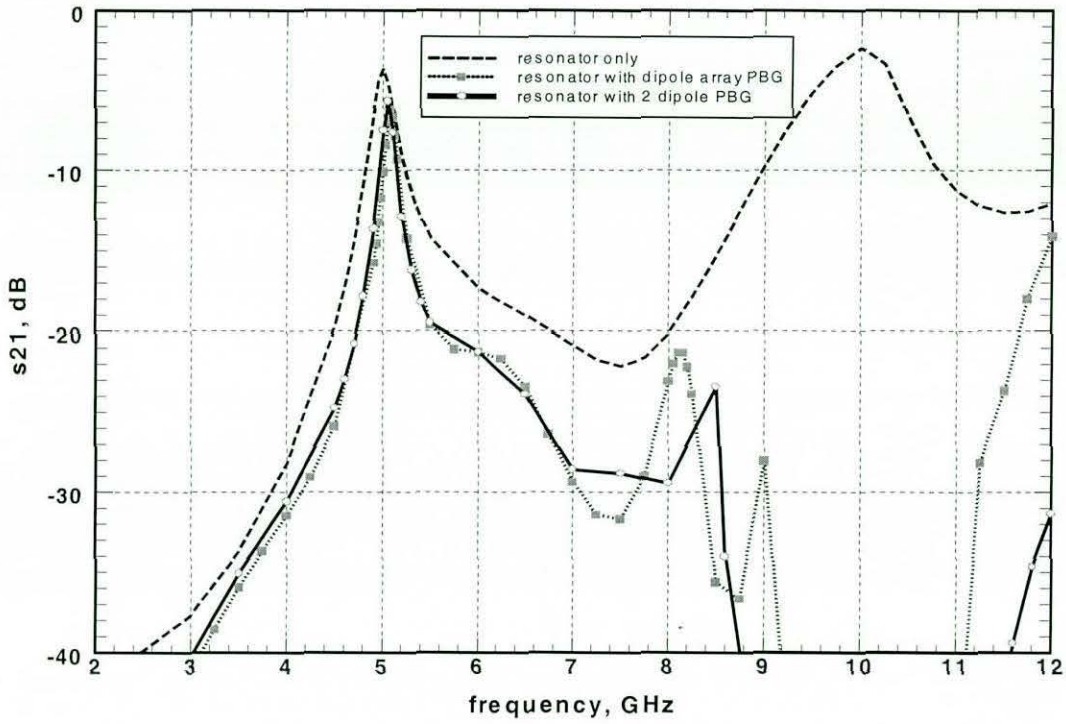


Figure 5.19a :Predicted insertion loss of a single resonator and with 1 and 2 types of dipole arrays.

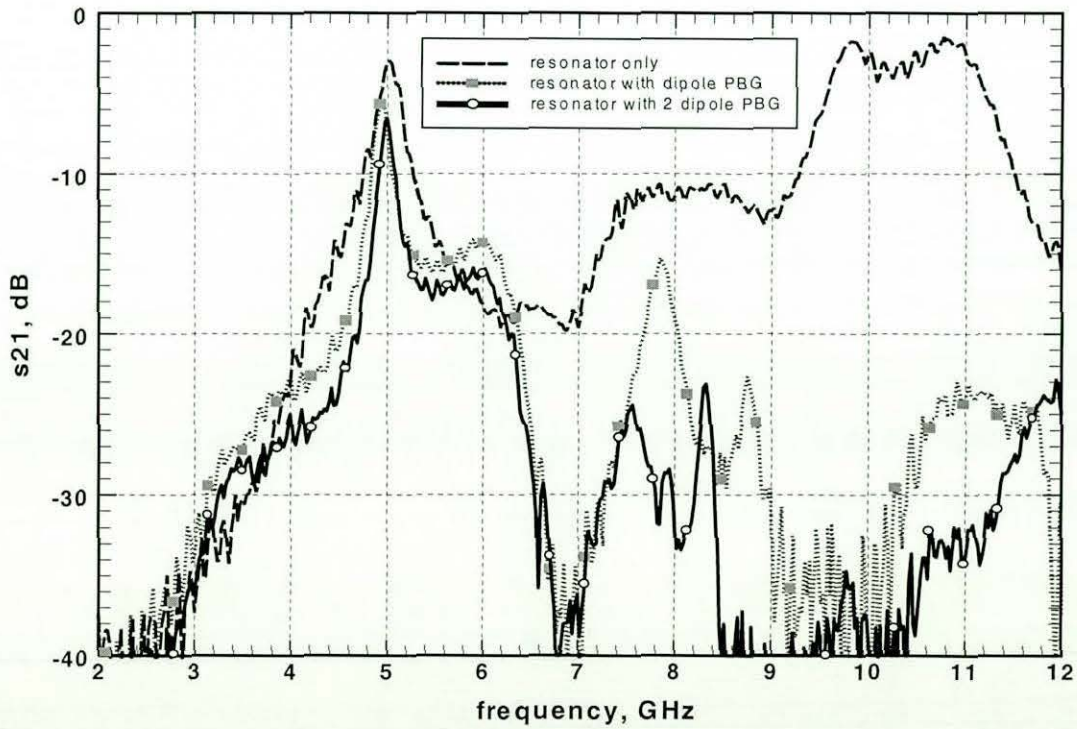


Figure 5.19b :Measured insertion loss of a single resonator and with 1 and 2 types of dipole arrays

5.6 Conclusions

The bandgap and bandpass properties for a tripole array on a triangular lattice have been assessed in this chapter. It incorporated both predictions and measurements of the propagation and bandgap properties and these were found to be in good agreement with each other.

The tripole conductor periodic array was shown to produce considerable large (TM and TE) bandgaps. This is one of the properties of Metallodielectric Photonic Crystals (MDPC) and they are known to exhibit much larger electromagnetic stopband than the photonic crystal [15]. The tripole array also possesses large overlapping between the TE and TM stopband which is the absolute bandgap on a two dimensional plane.

In the passband, the gain experienced before the bandgap is due to the tripole array. The conducting tripoles act as guiding elements for the transmitting antenna and thus concentrates the fields in the direction of the antenna. The radiation pattern confirms the narrowing of the main beam at the passband frequencies [16].

The radiation patterns are also presented in the E- and H- planes for frequencies before and after the bandgap. It is observed that when the bandgap occurs the energy is prohibited from propagating in the direction of the tripole array; it is reflected and radiated as leaky waves at an angle to the dielectric substrate. The main beam of the leaky waves tilts as the frequency increases, which is a characteristic of a leaky wave antenna. Since a typical tripole array can yield a large bandgap, design requirements can be made to not only stop the propagation in an unwanted direction but it could also control and steer the reflected beam by varying the element dimensions.

The effect of different dielectric constants and physical dimensions has also been examined and these properties could be used to design and control an array for different bandgap frequencies and different ranges of stopbands.

Two applications were investigated to try and utilise the benefits of such periodic conductor arrays. First, the efficiency of a well-designed patch antenna depends mainly on the surface wave losses to the substrate. The tripole array that has an absolute bandgap in all planar directions was chosen to eliminate the TM_0 mode surface waves and thus increases the patch antenna efficiency. Another positive effect is that the tripole array has increased the bandwidth of the patch antenna.

The other application examined a microstrip line and a resonator on a dipole array. Since the main propagation is restricted in one direction along the microstrip or resonator, a dipole array would be sufficient. Furthermore, due to the physical dimension of the dipole, it can be easily packed into a small area, an important factor for MMIC fabrication. It is illustrated that it is able to eradicate the first harmonic of the resonator. Also, a narrower Q factor has been observed as a result of loading it by the dipole array.

REFERENCES

- [1] VARDAXOGLU J.C. and PARKER, E.A.: 'Performance of two tripole arrays as frequency selective surfaces', *Electronic Letters*, Vol. 19,1983, pp. 709-710.
- [2] VARDAXOGLU J.C. and HOSSAINZADEH, A.H.: 'Single and double layer FSS of tripole arrays', *Proceedings 19th Microwave Europe Conference*, London, September 1989, pp. 863-868.
- [3] VARDAXOGLU J.C.: 'Frequency Selective Surfaces : Analysis and Design.', *Research Studies Press*, 1997, Chapter 2.
- [4] LEE R., CHAURAYA A., VARDAXOGLU J.C.: 'Metallodielectric Photonic Band Gap Structures for Microwave Filter and Antenna Applications' Submitted for PREP2000 Conference, Nottingham, United Kingdom, April 2000.
- [5] JOANNOPOULOS J.D., MEADE R.D., WINN J.N.: 'Photonic Crystals – Molding the Flow of Light', *Princeton University Press*, 1995, pp. 73-77.
- [6] LEE R., VARDAXOGLU J.C., BUDIMUR D.: 'Microwave Band-gap and Band-pass Structures using Planar Metallodielectric Periodic Arrays', *30th ARMMS Conference Digest*, Hindhead, United Kingdom, Nov. 1999.
- [7] LIN S.Y., ARJAVALLINGAM G., and ROBERTSON, W.M.: 'Investigation of absolute photonic band gaps in two-dimensional dielectric structures', *Journal of Modern Optics*, Vol. 44, No. 2, 1994, pp. 385-393.
- [8] QIAN Y., COCCIOLI R., SIEVENPIPER D., RADISIC V., YABLONOVITCH E., ITOH T.: 'A microstrip patch antenna using novel photonic band-gap structures', *Microwave Journal*, Jan 1999, pp. 66-76.
- [9] COCCIOLI R., YANG F.R., QIAN Y., ITOH T.: 'Effects of UC-PBG Substrate on Patch Antennas Performance', *International Conference on Electromagnetics in Advanced Applications 1999*, pp. 403-406

- [10] EmSight™, "User's Manual", Applied Wave Research. Inc., CA, USA.
- [11] RADISIC V., QIAN Y., COCCIOLI R., ITOH T.: 'Novel 2-D Photonic Bandgap Structure for Microstrip Lines', IEEE Microwave and Guided Wave Letters, Vol. 8, No. 2, Feb 1998, pp.69-71.
- [12] YANG F.R., KUANG P.M., QIAN Y., ITOH T.: 'A Uniplanar Compact Photonic Bandgap (UC-PBG) Structure and its Applications for Microwave Circuits', IEEE Transactions on Microwave Theory and Techniques, Vol.47, No.8, Aug 1999, pp. 1509-1514.
- [13] LEE R., VARDAXOGLU J.C., BUDIMUR D.: 'High Q resonator using a Microwave Bandgap Structure from Periodic Array of conducting Dipoles', Submitted for publication.
- [14] D. BUDUMIR, and C. W. TURNER, "Extremely Narrow Band Microstrip Bandpass Filters using Periodic Couplers", Microwave and Optical Technology Letters, Vol. 20, No.4, February 1999, pp.268-270.
- [15] BROWN, E. R. and MCMAHON, O. B.: 'Large electromagnetic stop bands in metallodielectric photonic crystals', Applied Physics Letters, Vol. 67, Oct 1995, pp. 2138.
- [16] MULDAVIN J. B. and REBEIZ G. M.: 'Millimeter-Wave Tapered-Slot Antennas on Synthesized Low Permittivity Substrates', IEEE Transactions on Antennas and Propagation, Vol.47, No. 8, Aug 1999, pp. 1276-1280.

Chapter 6

Conclusions

This thesis has described the theory and practical demonstration of a novel kind of planar 'photonic' bandgap crystal substrate that prohibits any propagation of electromagnetic fields in all planar directions within the bandgap frequencies.

The method of modeling has been adopted from past FSS programs for modal analysis of scattering from a single layer infinite array. Changes were made for the first time to the computer modeling to enable calculation of propagation modes in the plane of the array. Selection criteria are established to enable the analysis of propagation modes along the plane of the array. The purpose is to find the 'photonic' bandgap where propagation is prohibited in all directions in the array's plane. Such array structures can also be termed as 'Planar Metallodielectric Bandgap Crystals' (MPBG).

Modelling results for a dielectric slab and a grounded dielectric slab have successfully predicted all the propagation modes that exist on the plane of the array.

The 'Photonic' bandgap for dipole, cross dipole and tripole arrays were investigated and the effects of lattice configuration, dielectric constant and element parameters on the bandgap width and location have also been studied.

The dipole array has exhibited a bandgap over a wide range of propagation direction but it does not have an absolute bandgap due to its singly polarised nature of the dipole element. However, due to its physical shape (small width size) it can be packed closely together and thus increases the packing density. It can be used as a planar 1-D 'photonic' crystal where the only propagation is perpendicular to the length of the dipole.

The cross dipole does demonstrate an absolute bandgap in all planar directions. It can be chosen as a 2-D planar 'photonic crystal' for a square lattice. However, the beginning of the TE bandgap tends to vary over a large frequency range as the propagation direction changes. Further research effort looks into 'stabilising' the bandgap so that the beginning of the bandgap does not vary with the direction of propagation.

The tripole was chosen because it is not a linearly polarised element and it proves to provide a 'stable' bandgap, as its starting bandgap frequency is almost constant with respect to all propagation directions. The properties of the tripole array were investigated in more detail; this included the gain demonstrated in the passband frequencies and the radiation patterns in E and H planes in both the region of the passband and the stopband [1-2].

From the modeling results and practical demonstrations presented in this thesis for doubly periodic conductor arrays, the propagation and bandgap properties have been shown to be in good agreement with each other.

Different dielectric constants and physical dimensions can be designed to vary the stopband location and width; these properties could be used in as a means of controlling bandgap start frequencies and range [3-4].

Two applications were investigated for the benefits of having such conductor periodic arrays. The tripole periodic array is chosen to eliminate TM_0 mode surface waves and thus enhance the patch antenna performance and bandwidth [5].

The other application examined a microstrip line and resonator on the dipole array [6,7]. From the microstrip example, a stopband was revealed with respect to the dipole array used. For the resonator, it is illustrated that it is possible to eradicate the first harmonic and produce a narrower Q as a result of loading by the dipole array.

Possibilities of future research efforts might cover the modeling and study of doubly periodic aperture arrays. Such arrays can be used as PBG ground plane in applications for microwave circuits [8,9].

Future research efforts might also include the modeling of doubly periodic arrays in multiple layers to produce periodicity in three dimensions. This will be a form of 3-D photonic crystal and at frequencies in its absolute bandgap region, it will prohibit propagation in all directions [10].

Other possible experiments might include placing the array in a waveguide and using its bandgap for filtering purposes [11]. The array could also be used to channel and focus the radiating beam of an antenna in certain direction thus increasing its intensity [12,13].

- [8] RADISIC, V., QIAN, Y., COCCIOLI, R., ITOH, T.: 'Novel 2-D Photonic bandgap structure for Microstrip Lines', IEEE Microwave and Guided Wave Letters, Vol. 8, No. 2, Feb 1998, pp.69-71.
- [9] YANG F.R., KUANG P.M., QIAN Y., ITOH T.: 'A Uniplanar Compact Photonic Bandgap (UC-PBG) Structure and its Applications for Microwave Circuits', IEEE Transactions on Microwave Theory and Techniques, Vol.47, No.8, Aug 1999, pp. 1509-1514.
- [10] JOANNOPOULOS J.D., MEADE R.D., WINN J.N.: 'Photonic Crystals – Molding the Flow of Light', Princeton University Press, 1995.
- [11] CALOZ, C., ZURCHER, J-F., SKRIVERVIK, A.K.: 'Measurement of a 2D Photonic Crystal in a Waveguide', Nice-International Symposium on Antennas, 1998, pp.627-630.
- [12] BROWN, E.R. and MCMAHON, O.B.: 'High zenithal directivity from a dipole antenna on a photonic crystal', Applied Physics Letters, Vol. 68, No.9, Feb 1996, pp. 1300-1302.
- [13] DANGLLOT J., VANBESIEN O., LIPPENS D.: 'A 4-Port Resonant Switch Patterned in a Photonic Crystal', IEEE Microwave and Guided Wave Letters, Vol. 9, No. 7, July 1999, pp. 274-276.

REFERENCES

- [1] LEE R., VARDAXOGLU J.C., BUDIMUR D.: 'Microwave Band-gap and Band-pass Structures using Planar Metallodielectric Periodic Arrays', 30th ARMMS Conference Digest, Hindhead, United Kingdom, Nov. 1999.
- [2] LEE R., CHAURAYA A., VARDAXOGLU J.C.: 'Metallodielectric Photonic Band Gap Structures for Microwave Filter and Antenna Applications' Submitted for PREP2000 Conference, Nottingham, United Kingdom, April 2000.
- [3] VARDAXOGLU J.C., LOCKYER D.S., KEARNEY M.J., LEE Y.L.R.: 'Photonic Induced Antenna Arrays and Their Bandgap Properties', International Conference on Electromagnetics in Advanced Applications 1999, pp 485-488.
- [4] ZHANG L, ALEXOPOULOS N.G.: 'Magnetically Tunable PBG Materials for Printed Antenna Applications', International Conference on Electromagnetics in Advanced Applications 1999, pp. 399-401.
- [5] QIAN Y., COCCIOLI R., SIEVENPIPER D., RADISIC V., YABLONOVITCH E., ITOH T.: 'A microstrip patch antenna using novel photonic band-gap structures', Microwave Journal, Jan 1999, pp. 66-76.
- [6] RUMSEY, I., PIKET_MAY, M., KELLY, R.K.: 'Photonic bandgap structures used as filters in microstrip circuits', IEEE Microwave and Guided Wave Letters, Vol. 8, No. 10, Oct 1998, pp.336-338.
- [7] LEE R., VARDAXOGLU J.C., BUDIMUR D.: 'High Q resonator using a Microwave Bandgap Structure from Periodic Array of conducting Dipoles', Submitted for publication.

